Plate Tectonics and Aspherical Earth Structure: The Importance of Poloidal-Toroidal Coupling

A. M. Forte and W. R. Peltier

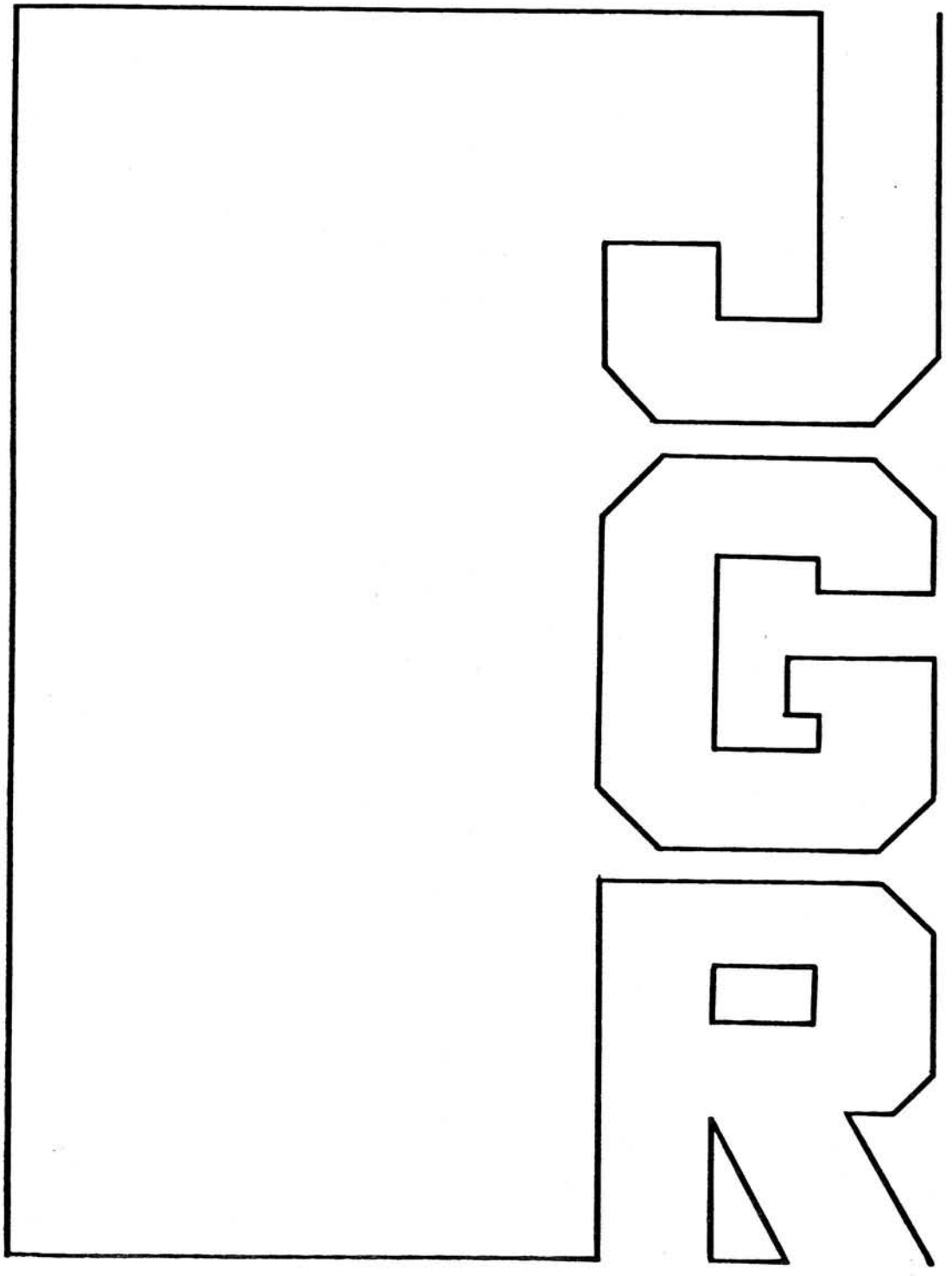

Journal of Geophysical Research, vol. 92, no. B4, April 10, 1987

JOURNAL OF GEOPHYSICAL RESEARCH, VOL. 92, NO. B5, PAGES 3645–3679, APRIL 10, 1987

Plate Tectonics and Aspherical Earth Structure: The Importance of Poloidal-Toroidal Coupling

A. M. FORTE AND W. R. PELTIER

Department of Physics, University of Toronto, Ontario, Canada

We derive poloidal flow internal loading Green functions for incompressible fluid models of the mantle consisting either of a single constant viscosity spherical shell or of two adjacent spherical shells having different viscosities. From the Green function we obtain kernels connecting the surface divergence, the geoid, and the surface topography fields to the lateral density heterogeneity inferred on the basis of the application of seismic tomographic imaging techniques, and with these kernels we argue that both the surface divergence and geoid fields, consisting of harmonic degrees 2–5, may be reasonably fit with only a factor of 8 viscosity increase at a depth of 1200 km. We point out, however, that the coupling from poloidal to toroidal flow which is required to understand surface velocity spectra, may allow these observations to be understood in terms of a viscosity increase at depth which is smaller than required by nonhydrostatic geoid data in the context of pure poloidal models. Using the observed kinetic energy in the surface plate motions as a constraint allows us to infer a value for the steady state upper mantle viscosity of $(2.0 \pm 0.5) \times 10^{21}$ Pa s. We comment on the implication of the difference between this number and the somewhat lower value (1×10^{21} Pa s) which has been derived on the basis of analyses of signatures of the glacial isostatic adjustment process.

1. INTRODUCTION

The relationship between the large-scale asphericities of the observed nonhydrostatic geoid and the seismically inferred lateral density variations in the earth's mantle has lately received much attention. The method most often employed to derive the kernels which relate geophysical surface observables to internal heterogeneities has been the propagator matrix technique [e.g., *Richards and Hager*, 1984*a*; *Ricard et al.*, 1984]. The analytic Green function method of *Parsons and Daly* [1983] allows one to derive, for sufficiently simple models, the geophysical kernel functions in a very direct way that does not require consideration of propagator matrices or Love numbers. In this paper we extend the Green function method described by *Parsons and Daly* [1983] and employ this alternative formulation of the internal loading problem to three-dimensional, self-gravitating, spherical shells of homogeneous (constant viscosity) fluid and also to the case of shells consisting of two layers having different viscosities.

There are two main reasons why we reexamine the internal loading problem for fluids with spherically symmetric properties. First, the Green function technique does have the attractive feature of allowing one to readily derive explicit, analytic expressions for the geophysical kernel functions, while the propagator matrix method as it has been applied delivers only numerical representations of these kernels. Since increasing attention is being payed to numerical modeling of convective flows in three-dimensional spherical geometry [e.g., *Baumgardner*, 1984], the explicit representation of the kernels to be derived here may be found useful. Second, the kernels that we obtain for a two-layer model will allow us to conduct an extensive and independent evaluation of the recent inferences of mantle viscosity using geoid anomalies by *Richards and Hager* [1984*a*]. In this paper we will present a detailed analysis of both the horizontal divergence of the surface flow and the geoid, and we will argue that previous conclusions drawn on the basis of the geoid data alone, to the effect that a large viscosity increase at depth in the earth's mantle is required [e.g., *Hager*, 1984], may not be warranted. In this connection we will argue that the main outstanding issue concerns the influence of coupling between the poloidal and toroidal components of the tectonic plate velocities.

The theoretical kernel functions describing the surface divergence of the fluid flow driven by internal lateral density variations will be employed to demonstrate that, on the whole, the observed large-scale plate motions are just those expected to exist on the basis of the deep density heterogeneity observed using seismic tomographic imaging. *Hager and O'Connell* [1981] have previously attempted to develop models of mantle flow which are noteworthy for being the first to include a realistic, three-dimensional, spherical geometry. In the formulation of these models, which *Hager and O'Connell* [1981] believe to be consistent with a boundary layer formulation of the convection problem, it is imagined that a major driving mechanism for plate motions is provided by the horizontal density variations in the cold thermal boundary layer (the lithosphere). In fact, boundary layer analyses of thermal convection in a fluid [e.g., *Turcotte and Oxburgh*, 1967; *Roberts*, 1977] show that the buoyancy forces in the horizontal thermal boundary layers are negligible in the asymptotic limit of very large Rayleigh numbers and that the fluid motion is driven by internal buoyancy forces localized in the ascending and descending thermal plumes. In addition, it is evident from the profiles of the horizontal divergence kernels which will be presented here that horizontal density contrasts in either the upper or lower thermal boundary layers will produce a vanishingly small flow. Finally, the flow models presented by *Hager and O'Connell* [1981] remain essentially kinematic since they include the observed surface plate velocities as a boundary condition and this requires the existence of an externally applied shearing stress to drive the plates. In the analysis to be presented here, on the other hand, we will use the seismically observed density heterogeneity in the mantle to predict the surface motions and will employ the observed surface velocities to constrain further the parameters of the earth model.

In the derivation of the kernels describing the nonhydrosta-

Paper number 6B6099.
0148-0227/87/006B-6099$05.00

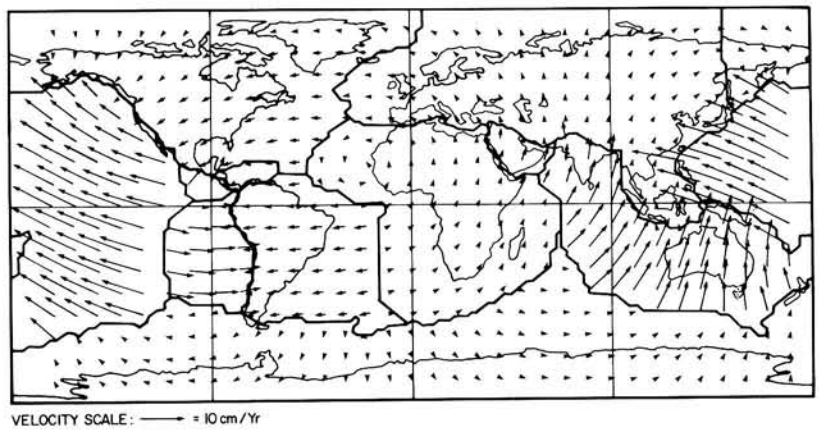

Fig. 1. Surface plate velocity field constructed from the absolute angular velocity vectors of *Minster and Jordan* [1978] in the "hot spot" frame.

tic geoid and the surface horizontal divergence of the mantle flow, it will be shown that the geoid is sensitive only to the ratio of the viscosity of one layer to that of an adjoining layer and that it cannot therefore be used to independently constrain the absolute value of the viscosity in the earth's mantle. In contrast it will be shown that the observed surface plate velocities do constrain the absolute viscosity values. We are thus able for the first time to obtain, by considering both the geoid and the horizontal divergence simultaneously, a preliminary estimate of the absolute value of the viscosity by ensuring that the dynamic balance between buoyant and viscous forces in the mantle is such as to enable us to match the kinetic energies of the predicted and observed surface flows. This is a main contribution of the present paper. The discrepancies between these absolute viscosity estimates and those obtained from glacial isostatic adjustment analyses [e.g., *Peltier*, 1982] will be shown to have important implications for the issue of transient mantle rheology [e.g., *Peltier*, 1985*b*].

The outline of the paper is as follows. In section 2 we employ the *Minster and Jordan* [1978] model of surface plate velocities to characterize the surface kinematics associated with mantle convection and to demonstrate anew the equipartition of kinetic energy which obtains between the poloidal and toroidal elements of the flow, a result which was apparently first obtained by *Hager and O'Connell* [1978]. Section 3 is concerned with a discussion of the correlations between these two independent scalar characterizations of plate motion and other geophysical observables, namely, the nonhydrostatic geoid and the seismically observed internal lateral heterogeneity of density. In section 4 we describe the new theory which we have developed to predict the poloidal component of the surface velocity field and the nonhydrostatic geoid from the tomographically inferred lateral heterogeneity of density at depth. The theory is employed to infer the contrast between the viscosities of the upper and lower mantles which is required by the data. A discussion of these interpretations is presented in section 5 where we argue that the effect of the generation of toroidal flow in the near-surface region of the mantle will most probably reduce the viscosity contrast inferred by fitting geoid height observations. In this section we will also present a quantitative discussion of the constraints imposed by our preliminary absolute viscosity estimates on the extent to which transient rheology is liable to be important in the upper mantle. Our principal conclusions are also summarized at the end of section 5.

2. PRESENT-DAY TECTONIC PLATE MOTIONS

Proceeding from the Wilson-Morgan hypothesis of fixed hot spots, *Minster and Jordan* [1978] have obtained an absolute motion model consisting of the present-day rotation rate vectors for each of the 11 surface plates. A map depicting the instantaneous, present-day surface plate velocities relative to the hot spot frame is shown in Figure 1. From these surface plate velocities we have computed two scalar fields which are of fundamental importance in considerations of hydrodynamic process: namely, the horizontal divergence and the radial vorticity. This "two scalar" summary of the surface kinematics is both necessary and sufficient to describe the type of plate boundaries which are observed in nature: Transform faults are regions where radial vorticity is important and ridges and trenches are regions where horizontal divergence is important [*Peltier*, 1985*a*]. *Hager and O'Connell* [1978] have previously calculated two complementary scalars which also describe the surface plate velocities: namely, the poloidal and toroidal generating scalars, which are directly related to horizontal divergence and radial vorticity although the latter process related fields were not computed from them.

For present purposes the north-south component of the surface velocity field, $v_\theta(\theta, \phi)$, and the west-east component, $v_\phi(\theta, \phi)$, have been expanded in terms of spherical harmonics up to degree and order 32. From the harmonic decompositions of these two fields one may proceed to calculate the spherical harmonic expansions of the horizontal divergence, $\nabla_H \cdot \mathbf{v}$, and the radial vorticity, $(\nabla \times \mathbf{v}) \cdot \hat{r}$ ($\hat{r}$ is the radial unit vector). The truncated spherical harmonic expansions of the horizontal divergence and the radial vorticity may be written as

$$\nabla_H \cdot \mathbf{v} = \sum_{l=0}^{32} \sum_{m=-l}^{l} D_l^m Y_l^m(\theta, \phi) \tag{1a}$$

and

$$(\nabla \times \mathbf{v}) \cdot \hat{r} = \sum_{l=0}^{32} \sum_{m=-l}^{l} V_l^m Y_l^m(\theta, \phi) \tag{1b}$$

where $Y_l^m(\theta, \phi)$ is the complex surface spherical harmonic.

An alternative scalar representation of the surface kinematics was obtained by *Hager and O'Connell* [1978] by describing the surface velocity field in terms of poloidal and toroidal components. In general, any solenoidal vector field $\mathbf{v}$ can be

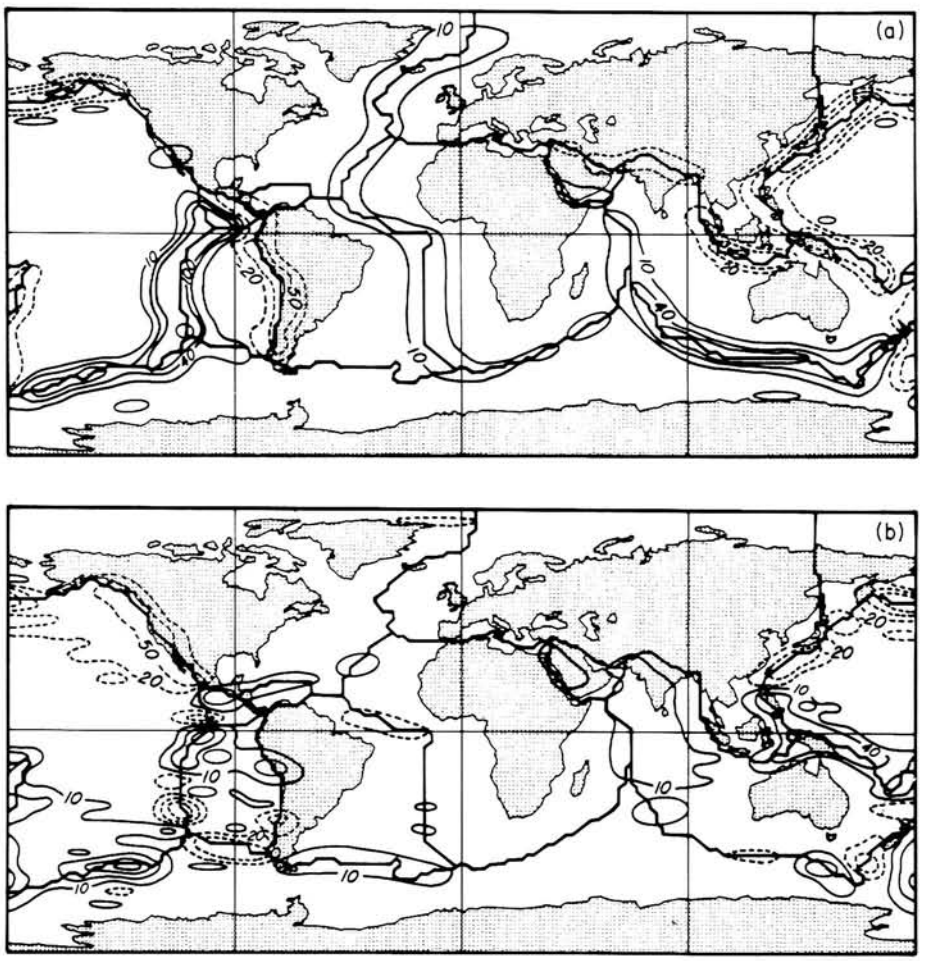

Fig. 2. (*a*) Surface divergence up to degree and order 32. The contour interval is 30×10^{-9} rad/yr and the individual contour levels are in units of 10^{-9} rad/yr. The dashed contour lines indicate negative divergence. (*b*) Radial vorticity to degree and order 32. The contour interval and units are as in Figure 2*a*. The dashed contour lines indicate negative vorticity (i.e., clockwise circulation).

expressed as [*Backus*, 1958; *Chandrasekhar*, 1961]

$$\mathbf{v} = \mathbf{T} + \mathbf{S} \tag{2a}$$

where

$$\mathbf{T} = \mathbf{\Lambda}\psi \tag{2b}$$

is the toroidal vector field with the defining scalar ψ and

$$\mathbf{S} = \nabla \times \mathbf{\Lambda}\phi \tag{2c}$$

is the poloidal vector field with the defining scalar ϕ. Following *Backus* [1958], we employ the vector operator $\mathbf{\Lambda}$, which is defined as

$$\mathbf{\Lambda} = \mathbf{r} \times \nabla \tag{3}$$

The assumption that the surface velocity field is solenoidal is justified to the extent that the material may be considered incompressible (i.e., $\nabla \cdot \mathbf{v} = 0$) which is certainly true in the case of completely rigid surface plates. In the present application, $\mathbf{v}(r = a)$ is the surface velocity field (a is the earth's radius). Upon expanding the scalars ψ and ϕ in terms of spherical harmonics, it is readily shown that one can express $\mathbf{T}$ as

$$\mathbf{T} = \sum_{l,m} T_l^m \mathbf{\Lambda} Y_l^m(\theta, \phi) \tag{4}$$

T_l^m will be referred to as the toroidal scalar (T_l^m is the scalar ${\psi_l}^m$ $(r = a)$). Similarly, one can express $\mathbf{S}$ as

$$\mathbf{S} = \sum_{l,m} S_l^m \hat{r} \times \mathbf{\Lambda} Y_l^m(\theta, \phi) \tag{5}$$

S_l^m will be called the poloidal scalar (S_l^m is the scalar $d{\phi_l}^m/dr$ $(r = a)$). A simple relationship exists between these scalars and the divergence and vorticity scalars defined previously in (1), namely,

$$S_l^m = \frac{aD_l^m}{l(l+1)} \tag{6a}$$

and

$$T_l^m = -\frac{aV_l^m}{l(l+1)} \tag{6b}$$

The harmonic coefficients D_l^m and V_l^m (see Table C1 in Appendix C) have been used to synthesize maps of surface divergence and radial vorticity using (1). The horizontal divergence field is shown in Figure 2*a* where contours of constant divergence are plotted. A map of the surface radial vorticity is presented in Figure 2*b*. Ridges and trenches show up as extrema of divergence, whereas transform faults like the San Andreas show up as extrema of vorticity.

It will be useful for purposes of later discussion to consider

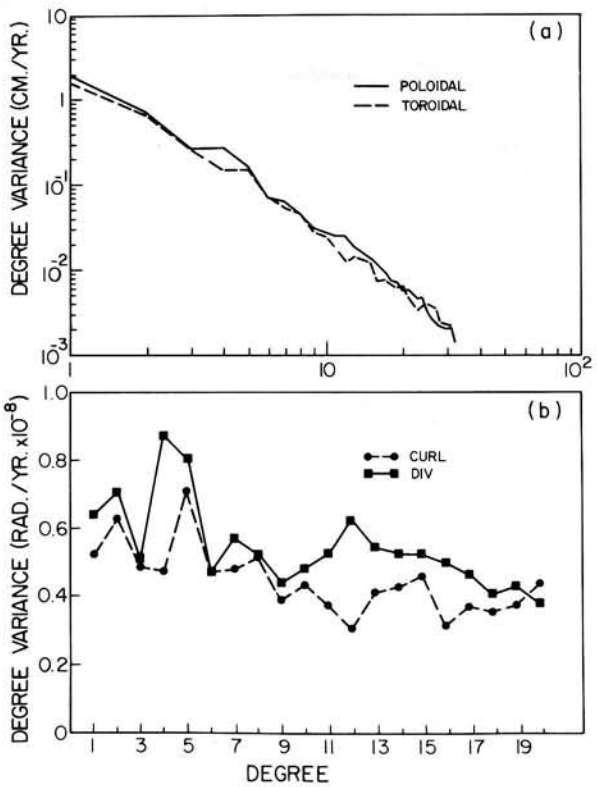

Fig. 3. (*a*) Degree variance of the poloidal and toroidal components of the surface velocity field. (*b*) Degree variance of the horizontal divergence and radial vorticity fields derived from the surface plate velocities.

how the kinetic energy of the surface motion is partitioned among the spherical harmonic components of the surface velocity field. A measure of the total power found in each harmonic degree is given by the degree variance σ_l. The degree variances of the poloidal and toroidal components of the velocity field are defined as

$$\sigma_l^2(\text{poloidal}) = \sum_{m=-l}^{l} S_l^m S_l^{m*} \tag{7a}$$

and

$$\sigma_l^2(\text{toroidal}) = \sum_{m=-l}^{l} T_l^m T_l^{m*} \tag{7b}$$

It can be shown, using the orthogonality properties of the vectors $\hat{\mathbf{r}} \times \mathbf{\Lambda} Y_l^m$ and $\mathbf{\Lambda} Y_l^m$ [e.g., *Jackson*, 1975], that the mean kinetic energy of the surface motion is given by

$$\frac{1}{4\pi}\int_0^{2\pi}\int_{-1}^{1} \mathbf{v}\cdot\mathbf{v}\, d\cos\theta\, d\phi = \sum_l l(l+1)[\sigma_l^2(\text{pol}) + \sigma_l^2(\text{tor})] \tag{8}$$

The degree variances for the poloidal and toroidal fields are shown in Figure 3*a*. Figure 3*a* illustrates anew a result first obtained by *Hager and O'Connell* [1978]: that the surface kinematic manifestations of the convection flow in the mantle exhibit an almost exact equipartition of kinetic energy between its poloidal and toroidal constituents. In a spherical shell consisting of chemically uniform fluid with spherically symmetric properties one expects thermally induced buoyancy to excite poloidal flow only. As noted by *Hager and O'Connell* [1981], one agency which probably contributes to the generation of the toroidal flow required by this equipartition is the extreme lateral variation of viscosity in the lithosphere. We also expect that an equally and perhaps more important mechanism for generating toroidal flow may be the presence of chemically distinct units (continental versus oceanic crust) in the near-surface region of the earth [e.g., *Peltier*, 1985*a*].

The degree variances of the horizontal divergence and radial vorticity have also been computed, as in (7*a*) and (7*b*), and are shown in Figure 3*b*. These power spectra reveal much more structure than those of the generating scalars shown in Figure 3*a*, and it will be observed in particular that the divergence spectrum is characterized by the presence of a well-defined peak for $l = 4, 5$. This peak is clearly associated with the dominant scale of the plates and therefore of the flow which sustains their motion [*Peltier*, 1985*a*].

3. Correlation of the Surface Kinematics With Other Geodynamic Observables

3.1. *The Geoid*

A quantitative measure of the linear dependence between two surface fields $F(\theta, \phi)$ and $G(\theta, \phi)$ is the degree correlation coefficient [e.g., *O'Connell*, 1971] which is a measure of the spatial correlation between $F_l(\theta, \phi)$ and $G_l(\theta, \phi)$, where $F_l(\theta, \phi)$ is the function synthesized from all the harmonics corresponding to degree l, that is,

$$F_l(\theta, \phi) = \sum_{m=-l}^{l} F_l^m Y_l^m(\theta, \phi)$$

in which F_l^m is the complex spherical harmonic coefficient of $F(\theta, \phi)$. The degree correlation coefficient ρ_l is the normalized inner product of $F_l(\theta, \phi)$ and $G_l(\theta, \phi)$, that is,

$$\rho_l = \frac{\sum_{m=-l}^{l} F_l^m G_l^{m*}}{\left[\left(\sum_{m=-l}^{l} F_l^m F_l^{m*}\right)\left(\sum_{m=-l}^{l} G_l^m G_l^{m*}\right)\right]^{1/2}} \tag{9}$$

In our analysis the function $G(\theta, \phi)$ will first be assumed to be the observed, GEM 10B, nonhydrostatic geoid of *Lerch et al.* [1979] (filtered by removal of the dynamically inferred flattening of *Nakiboglu* [1982]), and $F(\theta, \phi)$ will be either of the two scalars that were derived from the surface plate velocities; namely, the horizontal divergence ("div") and the radial vorti-

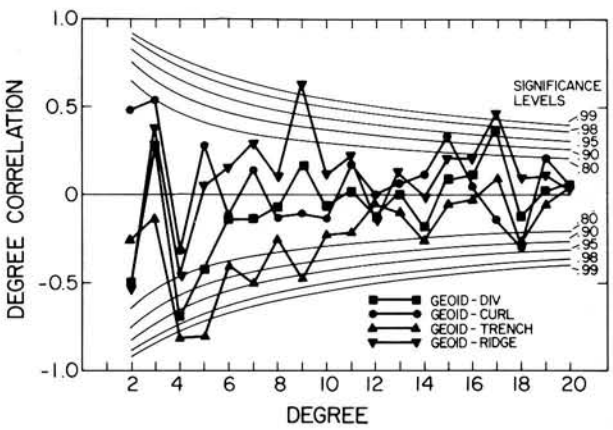

Fig. 4. Degree correlations of the horizontal divergence (div), radial vorticity (curl), trench signal, and ridge signal with the corrected GEM 10B nonhydrostatic geoid. An 80% significance level indicates a 20% probability that the degree correlation is zero.

city ("curl"). The degree correlations between the corrected nonhydrostatic geoid and the "div" and "curl" fields are shown in Figure 4. Inspection of Figure 4 shows that the greatest correlation between "div" and the geoid occur at degrees $l = 4$ and 5. *Hager and O'Connell* [1978] believe that the $l = 4$ correlation is random and dismiss it accordingly. We believe instead that such an interpretation ignores the steady trend to increasingly greater correlations as one goes from $l = 8$ to $l = 4$ and in addition it ignores the dynamic significance of the location at $l = 4$, 5 revealed in Figure 3*b*: The peak power in the horizontal divergence field occurs at these two degrees, and we believe this to be representative of the dominant horizontal length scale of the flow in the upper mantle. This interpretation is further reinforced by the strong $l = 4$ correlation of "div" with upper mantle heterogeneity, as we will show below.

There may be some significance to the observation that the trend of the correlation coefficients between "div" and the geoid is broken at $l = 3$ since at this degree a peak develops in the correlation between the "curl" field and the geoid. The region of strong negative vorticity along the western coast of North America (the San Andreas fault) and the region of strong positive vorticity centred over New Guinea (compare Figure 2*a*) are well represented in a map of the $l = 3$ vorticity field (not shown here). These regions also lie along plate boundaries where continental crust meets oceanic crust, and this leads us to speculate that lateral chemistry variations may be important in determining the $l = 3$ vorticity field as well as explaining the degree 3 correlation with the goid.

A more concrete illustration of the spatial correspondence between the geoid anomaly field and the surface divergence field for degrees 4–8 is provided in Figures 5*a* and 5*b*, which show the maps synthesized from these harmonic constituents. Ridges (positive divergence) are generally coincident with geoid lows, and trenches (negative divergence) are coincident with geoid highs; this correspondence between ridges/trenches and geoid lows/highs had previously been noted in the early pioneering studies of *Runcorn* [1964, 1967].

We have examined the relationship between the geoid and ridges and trenches in greater detail by separating the surface divergence field into two parts: the positive divergence field (the "ridge signal") and the negative divergence field (the "trench signal"). This separation is such that the sum of the ridge and trench fields equals the original surface divergence field. The spherical harmonic coefficients of these two fields were calculated, and their degree variances are plotted in Figure 6, where one can observe that the ridge signal again has a peak at degree 4 and the trench signal has a peak at degree 2. We have also determined the degree correlations of these two fields with the nonhydrostatic geoid, and the results are shown in Figure 4. The correlation between the trench signal and the geoid is excellent for degrees 4–9. *Hager* [1984] has shown there to be a good correlation between the actual geoid and a geoid predicted by a model which includes the density heterogeneity associated with downgoing slabs only, in this same band of wave numbers $4 \leq l \leq 9$. We observe that the weak negative correlation at degree 2 between "div" and the geoid is entirely due to the ridge signal which is also weakly correlated to the geoid at degree 4. The ridge correlation at degree 4 is important since the peak power in the ridge spectrum is at the same degree. It is not surprising that this correlation is weaker than the degree 4 trench correlation since the lateral density variations associated with buoyant upwellings in a thermally convecting fluid are expected to be of smaller amplitude than those associated with the more intense downwellings particularly if there is some degree of internal heating in the fluid [e.g., *Jarvis and Peltier*, 1982].

The negative sign of the low-degree correlation coefficients between the surface divergence and the nonhydrostatic geoid shows that the long-wavelength geoid anomalies must be representative of internal buoyancy in the mantle. The geoid anomalies that are produced by a thermally convecting mantle will depend on the mutually opposing contributions to the anomalies provided by the effective lateral density variations caused by boundary deflections [e.g., *Pekeris*, 1935; *Runcorn*, 1967] and those due to the direct effect of the lateral density variations in the interior. The manner in which these contributions interfere provides important information regarding the viscosity structure of the mantle. Early speculations by *Runcorn* [1967] show him to be aware of the importance of radially varying viscosity on the geoid signature, and *Richards and Hager* [1984*a*] have in fact shown that an increase of viscosity with depth allows the geoid contribution delivered by observed internal density anomalies to dominate the opposing contribution provided by surface topography. A lengthier discussion of the correlation analysis presented in this section may be found in the work by *Forte and Peltier* [1987].

3.2. *Seismically Inferred Mantle Heterogeneity*

Recent developments in seismology [e.g., *Anderson and Dziewonski*, 1984] have made it possible, in a preliminary way, to map the earth's internal lateral heterogeneity at long wavelength and thus to provide a direct image of the convective circulation itself. In this section, available models of the earth's internal lateral heterogeneity will be examined to determine what constraints may thereby be placed on the nature of the thermal convective circulation occurring in the mantle.

3.2.1. *Upper mantle.* The theory of unresolved multiplet splitting has been applied in an analysis of fundamental spheroidal mode eigenfrequencies by *Masters et al.* [1982], who argued that the heterogeneity responsible for producing the observed splitting consisted mainly of degree 2 harmonics and was most likely localized in the depth range 420–670 km (the transition zone). A map of the degree 2 transition zone density perturbation, corresponding to the harmonic coefficients of *Masters et al.* [1982], is presented in Figure 5*d*. We found that a remarkably good correlation exists between the degree 2 heterogeneity of Figure 5*d* and the degree 2 surface divergence (shown in Figure 5*c*) and moreover that it has the proper sign; regions of negative divergence correspond to sinking flow and thus to negative temperature perturbations in the mantle and hence to positive density perturbations (assuming that the lateral density contrasts are controlled by lateral temperature variations). We expect that the degree 2 density perturbation will be produced by both lateral temperature contrasts and the deflection of the olivine-spinel phase boundary, although we believe that the latter is the most important contributor [*Forte and Peltier*, 1987; *Jarvis and Peltier*, 1986].

Woodhouse and Dziewonski's [1984] model M84C which describes the upper mantle confirms the presence of a degree 2 heterogeneity localized in the transition zone. Model M84C was parameterized in terms of spherical harmonic coefficients as

$$\delta(v_s^2) = \sum_{l=0}^{8} \sum_{m=-l}^{l} \delta m_l^m(x) Y_l^m(\theta, \phi) \tag{10}$$

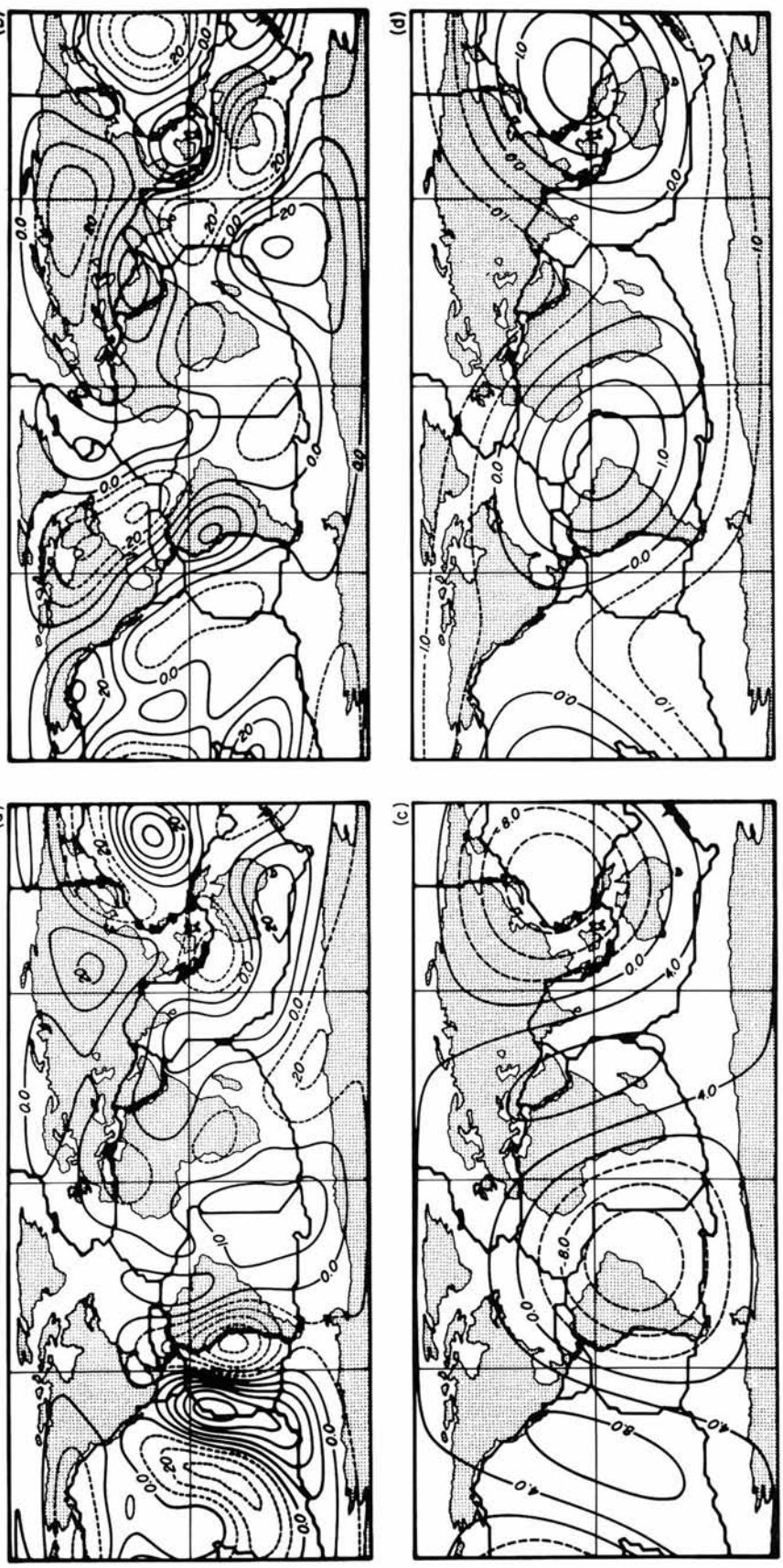

Fig. 5. (*a*) Horizontal divergence field for $4 \leq l \leq 8$. The contour interval is 10×10^{-9} rad/yr, and the individual contour levels are in units of 10^{-9} rad/yr. (*b*) Nonhydrostatic (GEM 10B) geoid heights for $4 \leq l \leq 8$. The contour interval is 10 m, and the dashed contours indicate negative geoid heights. (*c*) The $l = 2$ horizontal divergence field. The contour interval is 4×10^{-9} rad/yr. (*d*) The $l = 2$ transition zone density perturbation of *Masters et al.* [1982]. The contour interval is 0.5%.

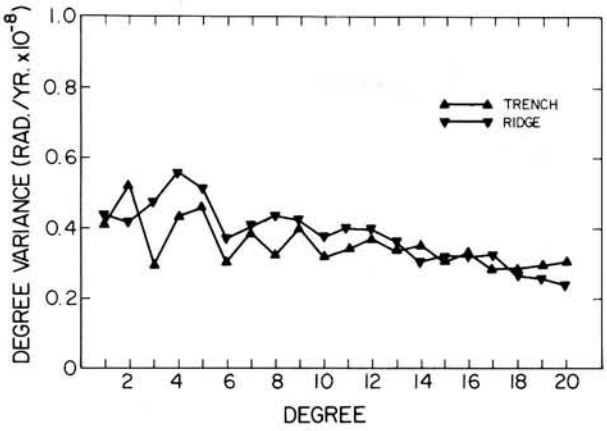

Fig. 6. Degree variance of the trench and ridge signals obtained from the surface divergence field.

where

$$\delta m_l^m(x) = \sum_{k=0}^{3} p_{klm} P_k(x)$$

$P_k(x)$ is a Legendre polynomial whose argument x is the normalized radius. From (10) it is evident that the heterogeneities with horizontal length scales less than 2500 km will not be resolved by this model nor will details with a vertical length scale less than 200 km. To determine the manner in which power is distributed among the various harmonic degrees in the model, the degree variance (determined as in (7)) as a function of depth has been calculated, and the results are summarized in Figure 7.

Jarvis and Peltier [1986] have suggested a new diagnostic technique for interpreting the power spectra of lateral heterogeneities in a thermally convecting mantle. They studied the power spectra of the internal lateral heterogeneities produced in steady, two-dimensional, numerically derived, Boussinesq convective circulations under various conditions. An important result that has emerged from their study is that in the thermal boundary layers of the convection cells, the power spectra of the lateral temperature variations are characterized by strong power at the wave number characteristic of the dominant horizontal length scale(s) of the flow. This was found to be true for all Rayleigh numbers that could conceivably correspond to mantle conditions for heated from below convection cells with various degrees of partial internal heating. It is on the basis of this spectral analysis that we expect that the $l = 5$ spectral peak at lithospheric depths which is evident in Figure 7 is due to the thermally induced heterogeneity in the upper thermal boundary layer of the circulation responsible for driving the plates.

We will next examine the correspondence between the surface plate motions and internal mantle heterogeneity in the spectral domain by calculating the degree correlations between the two surface scalars and $\delta(v_s^2)$ for various depths; the results for model M84C are presented in Figure 8. At degrees 2 and 4 there is a strong negative correlation between surface divergence and $\delta(v_s^2)$ that appears at about 300 km depth and extends down to 670 km depth. As discussed above, this negative correlation is expected if the lateral variations in shear wave velocity are produced by the thermal effects of upwelling and downwelling convective plumes.

In Figure 9 we present correlations of the ridge and trench signals with the upper mantle heterogeneity of model M84C. In Figure 9 we observe that the best correlations of the trench signal occur in the transition zone at degrees 2, 6, and 7; the negative sign of these correlations is reasonable, as this implies that positive velocity (and thus density) perturbations are associated with a negative trench signal (i.e., with downwelling). A very important observation is the significant correlation of the ridge signal throughout the entire upper mantle at degrees 4 and 5 which persists into the lower mantle (compare Figure 12). There is also a significant correlation of ridges with velocity heterogeneity at degrees 2 and 3 in the transition zone. The negative sign of the ridge correlations is again "correct" (except at $l = 3$), as it implies that negative velocity perturbations are associated with a positive ridge signal (i.e., with upwelling). The anomalous sign of the $l = 3$ ridge correlation may be due to the effects of poloidal-toroidal coupling [*Forte and Peltier*, 1987]. Clearly, at degrees 2, 4, and 5 the divergent component of the surface velocity field is the expression of deep, buoyant upwellings in the mantle as would be expected in a high Rayleigh number convective circulation with only partial internal heating. The ridges are not then merely passive features but rather are the surface manifestations of hot, active, upwelling thermals.

3.2.2. *Lower mantle.* A smoothed representation of the lateral P wave velocity heterogeneities in the lower mantle has been obtained by *Dziewonski* [1984]. We will consider his model L02.45 for which the velocity heterogeneities were rep-

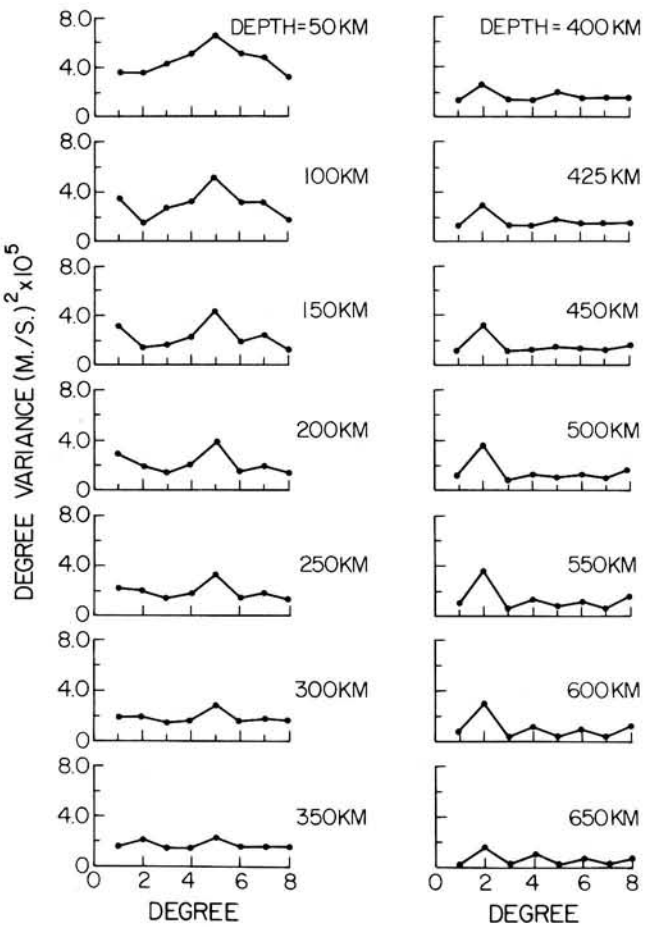

Fig. 7. Degree variance of the squared shear velocity heterogeneity as a function of depth for the upper mantle model M84C of *Woodhouse and Dziewonski* [1984]. The unit of variance is $(m/s)^2 \times 10^5$.

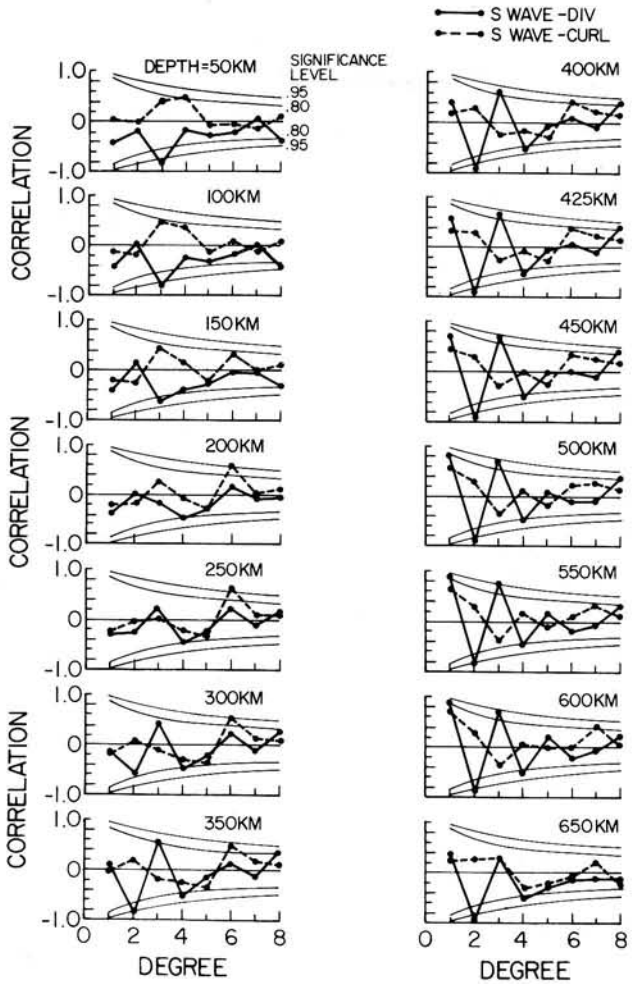

Fig. 8. Degree correlation as a function of depth between the squared shear velocity heterogeneity in model M84C of *Woodhouse and Dziewonski* [1984] and the horizontal divergence (div) and radial vorticity (curl).

resented in terms of a spherical harmonic expansion, as in equation (10), namely,

$$\delta(v_p) = \sum_{l=0}^{5} \sum_{m=-l}^{l} \delta m_l^m(x) Y_l^m(\theta, \phi) \tag{11}$$

where

$$\delta m_l^m(x) = \sum_{k=0}^{3} C_{klm} P_k(x)$$

The degree variance of $\delta(v_p)$ as a function of depth has been calculated for model L02.45, and the results are shown in Figure 10.

If it is assumed that a whole mantle convective circulation exists, then the upwelling and downwelling thermal plumes must penetrate the 670-km seismic discontinuity, and it should thus be reasonable to expect that the amplitude of the seismic velocity heterogeneities at the interface separating the upper and lower mantles should be the same in each mantle layer and thus that the power spectrum of $\delta(v_p)$ at 670 km should agree closely with the power spectrum of $\delta(v_s^2)$ at 670 km. An analysis of the correlation between the ridge signal and $\delta(v_p)$ presented below will show that this assumption is not unreasonable. One may directly compare the lateral heterogeneity of the upper mantle model with that of the lower mantle model by translating $\delta(v_p)$ into $\delta(v_s^2)$; this is readily done if one assumes that the velocity perturbations are caused solely by lateral temperature variations; with this assumption we write

$$\delta(v_s^2) = C\ \delta(v_p) \tag{12}$$

where

$$C = \frac{2v_s(\partial v_s/\partial T)_{p,m}}{(\partial v_p/\partial T)_{p,m}}$$

and the subscripts p, m indicate differentiation holding pressure and chemical composition (and/or phase) constant, respectively. The proportionality constant C in (12) may be evaluated from data obtained in laboratory measurements on minerals representative of the mantle; for spinel ($MgAl_2O_4$) the temperature derivatives of v_s and v_p given by *Anderson et al.* [1968] yield a C value of 8.0 km/s. Using (12) we have converted the power spectrum of $\delta(v_p)$ at 670 km depth into an equivalent spectrum of $\delta(v_s^2)$, thus enabling a comparison with the $\delta(v_s^2)$ spectrum of model M84C at this depth. We found that the power at $l = 4$ matched well, but the powers at all other degrees matched very poorly. *Woodhouse and Dziewonski* [1984] and *Dziewonski* [1984] point out that their data sets poorly resolve the mantle heterogeneity at this depth. As a result, we next considered the power spectrum of $\delta(v_s^2)$ at the

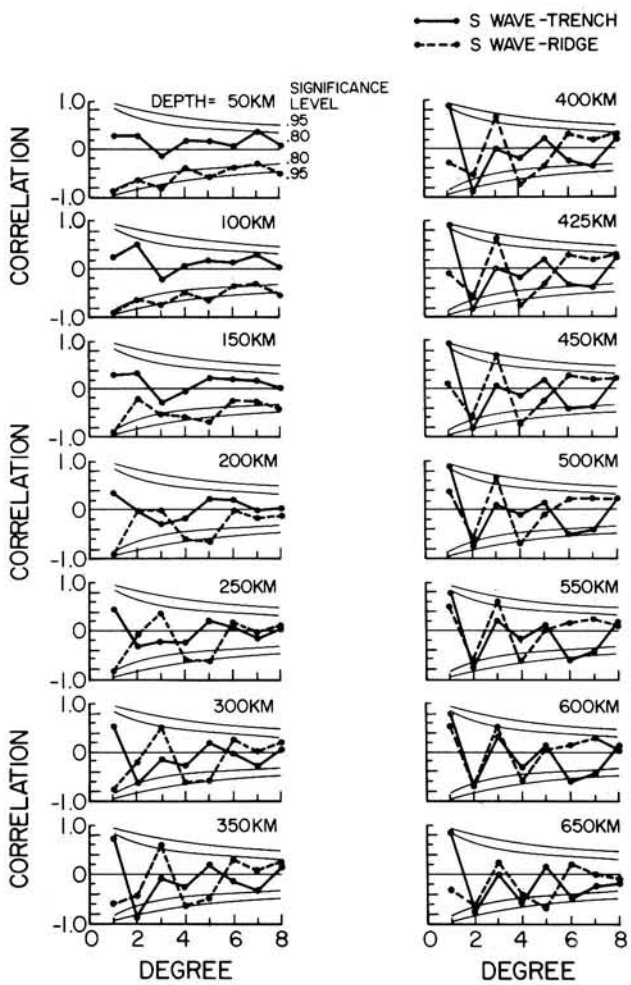

Fig. 9. Degree correlation as a function of depth between the squared shear velocity heterogeneity in model M84C *Woodhouse and Dziewonski* [1984] and the trench and ridge signals.

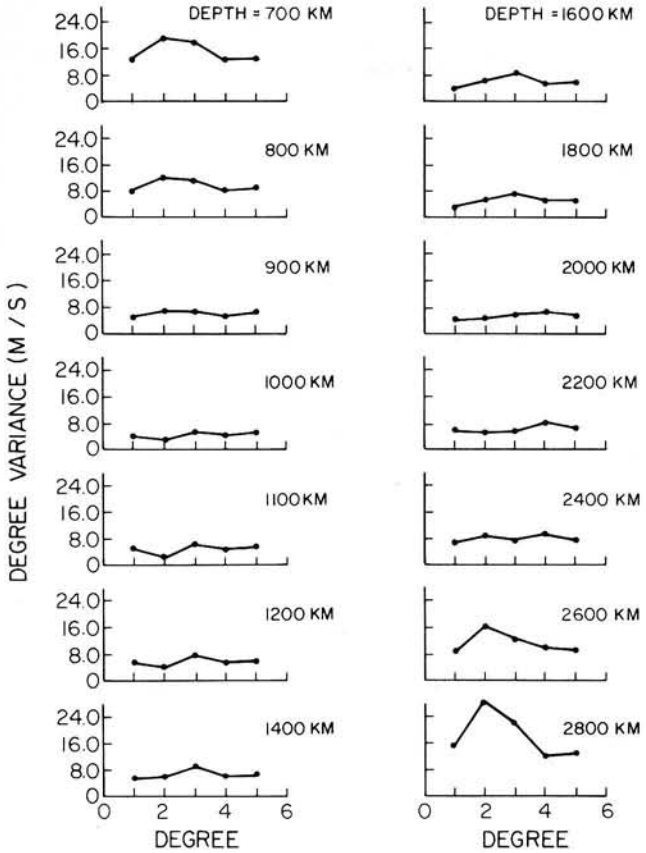

Fig. 10. Degree variance of the compressional wave velocity heterogeneity as a function of depth for the lower mantle model L02.45 of *Dziewonski* [1984]. The unit of variance is meters per second.

shallower depth of 650 km and the power spectrum of $\delta(v_p)$ at 700 km depth. The results of comparing the $\delta(v_p)$ field with the $\delta(v_s^2)$ field are summarized in Table 1. From Table 1 one can see that the power of the even degree harmonics is in good agreement, while the power at the odd degrees in model L02.45 is substantially greater than that of model M84C, and this is not surprising since the odd harmonics in the upper mantle model are poorly resolved at these depths [*Woodhouse and Dziewonski*, 1984]. We, of course, do not imply by the use of the temperature derivatives for spinel that this mineral is a constituent of the lower mantle, but the results obtained here indicate that these derivatives may provide a reasonable estimate of the actual values.

The power spectra of the upper and lower mantle models match quite well when interpreted in terms of lateral temperature variations, and this is somewhat unexpected since part of the velocity heterogeneity at 670 km depth should also include the contribution provided by the deformed spinel-mixed oxides phase change boundary. These results would seem to suggest that the phase boundary deflection is not significant and consequently that the Clapeyron slope of this phase transformation might be rather small.

In Figure 10 we see that the power spectrum of $\delta(v_p)$ shows a strong $l = 2$ peak at the base of the lower mantle, while at shallower depths the spectrum becomes flat with significantly less power than the peak at 2800 km depth. Following *Jarvis and Peltier* [1986], we may interpret this variation of lateral heterogeneity with depth in the context of a thermal convective circulation in the mantle; therefore the strong peak at the fundamental wave number ($l = 2$) in a depth interval of about 100–200 km next to the core-mantle boundary (i.e., within the seismic D'' layer) indicates the existence of a well-defined thermal boundary layer which would be associated with a partly heated from below, high Rayleigh number convective circulation whose dominant scale is of degree 2.

It is possible to investigate the temperature variations in D'' by converting $\delta(v_p)$ in model L02.45 into equivalent lateral temperature variations δT. If we again assume that $\delta(v_p)$ is only produced by temperature variations, then we may write

$$\delta T = (\partial v_p/\partial T)_{p,m}^{-1}\, \delta(v_p) \tag{13}$$

Stacey and Loper [1983] have derived a thermodynamic expression for $(\partial K_s/\partial T)_p$ which they used to calculate a $\partial v_p/\partial T$ value of -0.0899 m s^{-1} K^{-1} in D''. *Dziewonski* [1984] has provided a map of $\delta(v_p)$ at the core-mantle boundary synthesized from the harmonic coefficients of model L02.45, and in it one observes that the amplitude of the $\delta(v_p)$ field is about 100 m/s, which translates (using equation (13)) into an amplitude of 1100°K in the equivalent δT field. This amplitude is about the same as the temperature jump across D'' which is estimated to be 840°K $\pm$ 30% [*Stacey and Loper*, 1983], and this is precisely what is expected in a high Rayleigh number convective circulation in which the temperature contrast of the plumes relative to the adiabatic core of the convection cell is about the same as the temperature jump across the thermal boundary layer [e.g., *Jarvis and Peltier*, 1982]. Model L02.45 is a low-pass-filtered image of the lateral heterogeneity in the lower mantle [*Dziewonski*, 1984]; however, we are fairly confident that our inference of the amplitude of the lateral temperature variations in D'' is valid, since according to *Jarvis and Peltier* [1986] almost all the power in the δT field is confined to the fundamental wave number in the thermal boundary layer which in our case is $l = 2$.

The degree correlation coefficients between the "div" and "curl" fields and the $\delta(v_p)$ field of model L02.45 have been calculated for various depths, and the results are shown in Figure 11, wherein one sees that unlike the degree correlations for the upper mantle heterogeneities, there are no sharp correlations in the lower mantle. The degree correlations of the separate ridge and trench signals with $\delta(v_p)$ are presented in Figure 12. The most notable correlation is that of the degree 3 component of the ridge signal which persists from 1200 km depth down to the core-mantle boundary; above 1200 km the sign of the degree 3 correlation "flips," and perhaps this reversal is due to a coupling to toroidal flow as suggested by the degree 3 vorticity correlations shown in Figure 11. An important result is provided by the ridge correlations in the depth range 700–900 km. (compare Figure 12) which are almost identical to the ridge correlations in the transition zone (compare Figure 9) since this suggests that upwelling thermal plumes do continue across the 670-km "boundary."

TABLE 1. Matching the Degree Variances of the Upper and Lower Mantle Models at Spinel-Mixed Oxides Phase Boundary

Model M84C (at z = 650 km)		Model L02.45 (at z = 700 km)	
Degree l	$\delta(v_s^2)$, (m/s)$^2 \times 10^5$	$\delta(v_p)$, m/s	Equivalent $\delta(v_s^2)$, (m/s)$^2 \times 10^5$
$l = 2$	1.56	18.8	1.50
$l = 3$	0.11	17.7	1.42
$l = 4$	1.04	12.6	1.01
$l = 5$	0.22	12.7	1.02

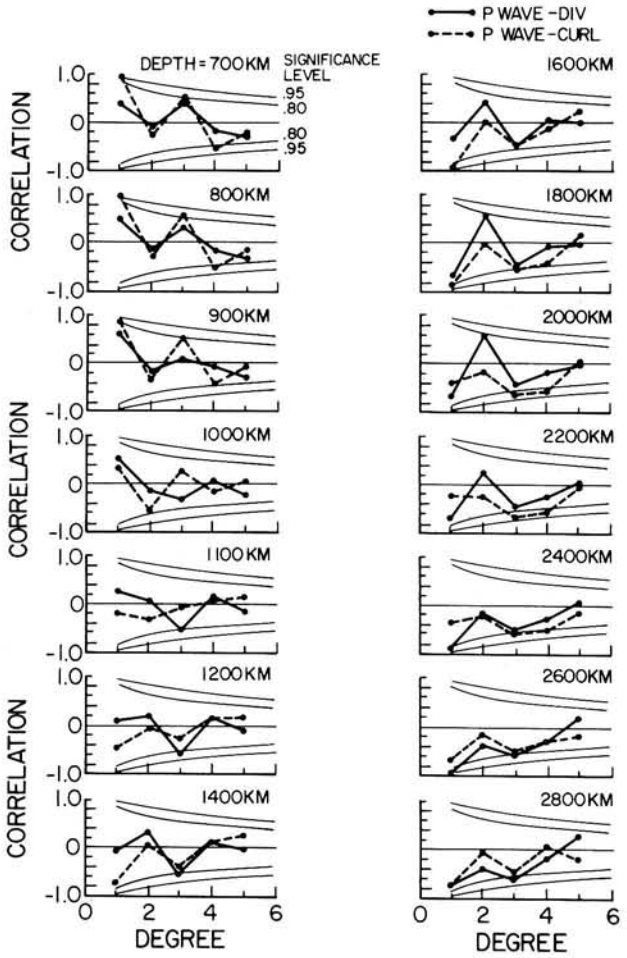

Fig. 11. Degree correlation as a function of depth between the compressional wave velocity heterogeneity in model L02.45 [*Dziewonski*, 1984] and the horizontal divergence (div) and radial vorticity (curl).

4. Predicting Surface Motions, the Geoid, and Surface Topography From Seismically Inferred Mantle Heterogeneity

In this section we will derive the theoretical results which are required to connect the newly observed lateral heterogeneity of the mantle to surface plate kinematics and the structure of the gravitational field. Our theoretical models of these connections will be described in order of increasing complexity.

4.1. *Homogeneous (Constant Viscosity) Mantle Green Function*

If one applies a first-order perturbation theory to the hydrodynamic equations expressing the principles of mass conservation and momentum conservation, then the following equations are obtained which are accurate to first order:

$$\nabla \cdot \mathbf{u} = 0 \tag{14}$$

and

$$\rho_0 \mathbf{g}_1 + \rho_1 \mathbf{g}_0 - \nabla P_1 + \eta \Delta \mathbf{u} = 0 \tag{15}$$

The quantities with subscript 1 are perturbations to the hydrostatic reference state which is denoted by the subscript 0. In arriving at (14) it has been assumed that the density distribution of the reference state, ρ_0, is constant (i.e., the Boussinesq approximation has been made), while in (15) the inertial force has been ignored since the mantle is characterized by an essentially infinite Prandtl number. The term $\rho_0 \mathbf{g}_1$, which describes the effect of self-gravitation, was ignored in the analysis of *Parsons and Daly* [1983]. The acceleration $\mathbf{g}_0$ is given by

$$\mathbf{g}_0 = -\frac{g_0}{r}\mathbf{r} \tag{16}$$

where g_0 is assumed constant since it is known that the acceleration due to gravity is approximately constant in the earth's mantle. We will adopt the sign convention that the acceleration perturbation, $\mathbf{g}_1$, is expressed as a positive gradient:

$$\mathbf{g}_1 = \nabla \phi_1 \tag{17}$$

and therefore that ϕ_1, the perturbed gravitational potential, satisfies

$$\Delta \phi_1 = -4\pi G \rho_1 \tag{18}$$

Equation (14) asserts that $\mathbf{u}$ is a solenoidal vector field which may thus be represented as [*Backus*, 1958]

$$\mathbf{u} = \nabla \times \Lambda p + \Lambda q \tag{19}$$

where the operator Λ was defined in (3) and p and q are the poloidal and toroidal scalars, respectively. Throughout this section we will make liberal use of the mathematical identities employed by *Backus* [1958].

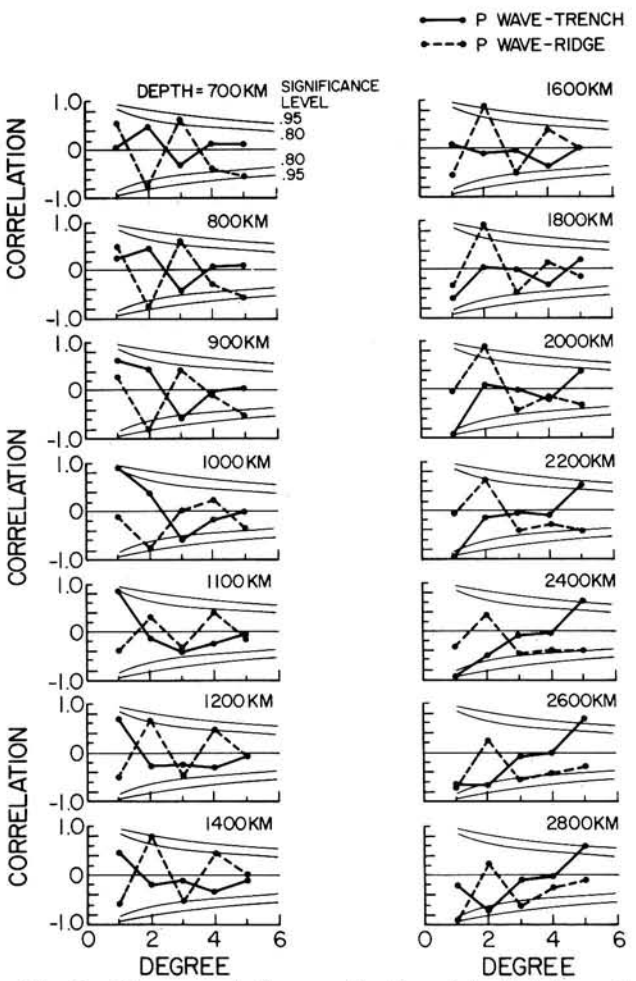

Fig. 12. Degree correlation as a function of depth between the compressional wave velocity heterogeneity in model L02.45 [*Dziewonski*, 1984] and the trench and ridge signals.

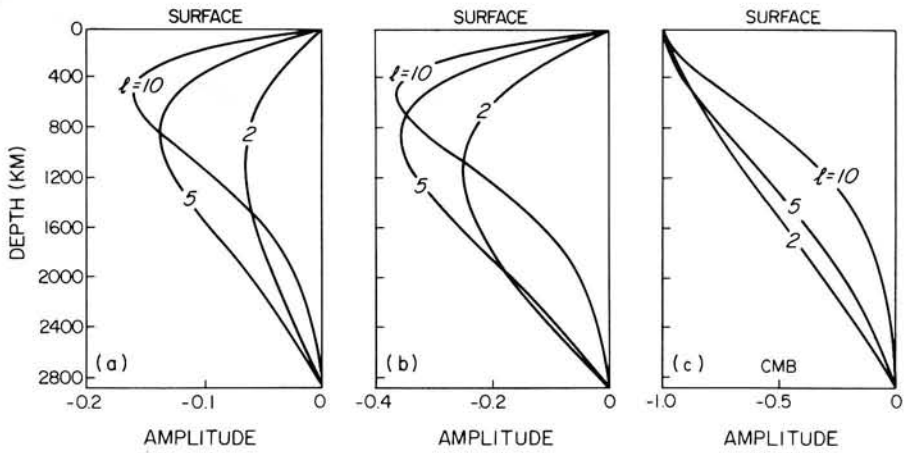

Fig. 13. Kernels for an incompressible, homogeneous mantle with free slip conditions at the surface and CMB. (*a*) Horizontal divergence kernels. (*b*) Geoid kernels for a self-gravitating mantle. (*c*) Surface topography kernels for a self-gravitating mantle.

If one substitutes (16), (17), and (19) into (15) and applies the operator $\nabla \times$ to the resulting equation the following result, is obtained:

$$\mathbf{\Lambda} \frac{\rho_1 g_0}{r} + \eta \nabla \times \mathbf{\Lambda} \Delta q - \eta \mathbf{\Lambda} \Delta^2 p = 0 \tag{20}$$

If one applies the operator

$$\frac{1}{4\pi} \int_s dS \, \mathbf{\Lambda} Y_l^m$$

to (20), the following further result is obtained:

$$\frac{1}{4\pi} \int_s Y_l^m \Lambda^2 \frac{\rho_1 g_0}{r} \, dS = \frac{\eta}{4\pi} \int_s Y_l^m \Lambda^2 \Delta^2 p \, dS \tag{21}$$

The operator $\Lambda^2 = \mathbf{\Lambda} \cdot \mathbf{\Lambda}$ is characterized by the property that

$$\Lambda^2 Y_l^m = -l(l+1) Y_l^m \tag{22}$$

where $Y_l^m(\theta, \phi)$ is the complex spherical harmonic function which is normalized such that

$$\frac{1}{4\pi} \int_s Y_l^m(\theta, \phi) Y_s^{t*}(\theta, \phi) \, dS = \delta_{ls} \, \delta_{mt} \tag{23}$$

If one now expands the scalars ρ_1 and p in terms of spherical harmonics and applies the results (22) and (23), we obtain from (21) the following fundamental equation:

$$D_l^2 p_l^m(r) = \frac{g_0}{\eta} \frac{(\rho_1)_l^m(r)}{r} \tag{24}$$

where $p_l^m(r)$ and $(\rho_1)_l^m(r)$ are the radially varying spherical harmonic coefficients of the scalars p and ρ_1, respectively. D_l^2 is the transformed biharmonic operator Δ^2, and the operator D_l is defined as

$$D_l = \frac{d^2}{dr^2} + \frac{2}{r} \frac{d}{dr} - \frac{l(l+1)}{r^2}$$

Equation (24) shows that when the dynamic viscosity η is assumed constant, then lateral density variations will drive only a poloidal flow field.

To determine the poloidal flow Green function $p_l^m(r, r')$, one must solve the equation

$$D_l^2 \, p_l^m(r, r') = \delta(r - r') \tag{25}$$

where $\delta(r)$ is the Dirac delta function and r' is the depth at which the δ function load is applied. The function satisfying (25) will be completely determined after applying the appropriate boundary conditions at the earth's surface ($r = a$) and at the core-mantle boundary ($r = b$). Once the Green function has been found, then the poloidal scalar may be obtained from

$$p_l^m(r) = \frac{g_0}{\eta} \int_b^a \frac{(\rho_1)_l^m(r')}{r'} \, p_l^m(r, r') \, dr' \tag{26}$$

We have shown in the correlation analysis of section 3 that the tectonic plates should be regarded as participating in the large-scale flow in the mantle, and therefore if we are to model the surface plate motions, application of a free slip boundary condition at the earth's surface is suggested. We will also assume a free slip boundary condition at the core-mantle boundary (CMB). The derivation of the Green function which satisfies (25) and the stated boundary conditions is described in Appendix A.

In attempting to predict the surface plate motions using the poloidal flow scalar of (26) one is naturally confronted with the difficulty of explaining the toroidal flow which is observed in the surface velocity field. This difficulty has led some researchers [e.g., *Ricard et al.*, 1984] to assert that it is not possible to describe surface plate kinematics with a spherically symmetric viscosity model. We note instead that the good correlation between the surface divergence and the seismically inferred lateral heterogeneity in the upper mantle at degrees 2 and 4 suggests to us that there may be an almost linear relationship between these two fields at $l = 2$ and $l = 4$ and that it should therefore be possible to model the surface divergence, which is directly determined from the poloidal scalar, with a spherically symmetric viscosity model. Since we assume that toroidal flow is mostly generated in the near-surface region of the earth, then it is reasonable, as a first approximation, to assume that internal density heterogeneity below the lithosphere excites mostly a poloidal flow, thus maintaining the validity of (24). In Appendix A we derive the expression for the dimensionless kernel $S_l(r')$, which relates the spherical harmon-

TABLE 2. Degree Correlations Between Predicted Surface Divergence for a Homogeneous Mantle and Observed Surface Divergence

Degree l	Correlation Coefficient	Significance Level α
$l = 2$	0.80	$90\% < \alpha < 95\%$
$l = 3$	0.30	$\alpha < 80\%$
$l = 4$	0.68	$95\% < \alpha < 98\%$
$l = 5$	0.28	$\alpha < 80\%$

ic components of the horizontal divergence field at $r = a$ to the lateral variations of density in a constant viscosity mantle as

$$(\nabla_H \cdot \mathbf{u})_l^m(r = a) = \frac{g_0}{\eta} \int_b^a S_l(r')(\rho_1)_l^m(r')\, dr' \qquad (27)$$

In Figure 13*a* we present profiles of this kernel for several values of spherical harmonic degree l.

We have used (27) to predict the surface divergence field driven by the seismically inferred lateral heterogeneities in the mantle. The density perturbations $(\rho_1)_l^m(r)$ were obtained from models M84C of *Woodhouse and Dziewonski* [1984] and L02.45 of *Dziewonski* [1984] assuming that the lateral variations in seismic wave speeds are caused solely by lateral temperature variations, and we have again employed the temperature derivatives for spinel given by *Anderson et al.* [1968]. The assumption of pure lateral temperature variations is not entirely valid in the transition zone where part of the lateral heterogeneity is due to the deflected olivine-spinel phase boundary. The degree correlations between the predicted and observed divergence fields are given in Table 2, where one observes that very good correlations are obtained at degrees 2 and 4, as expected.

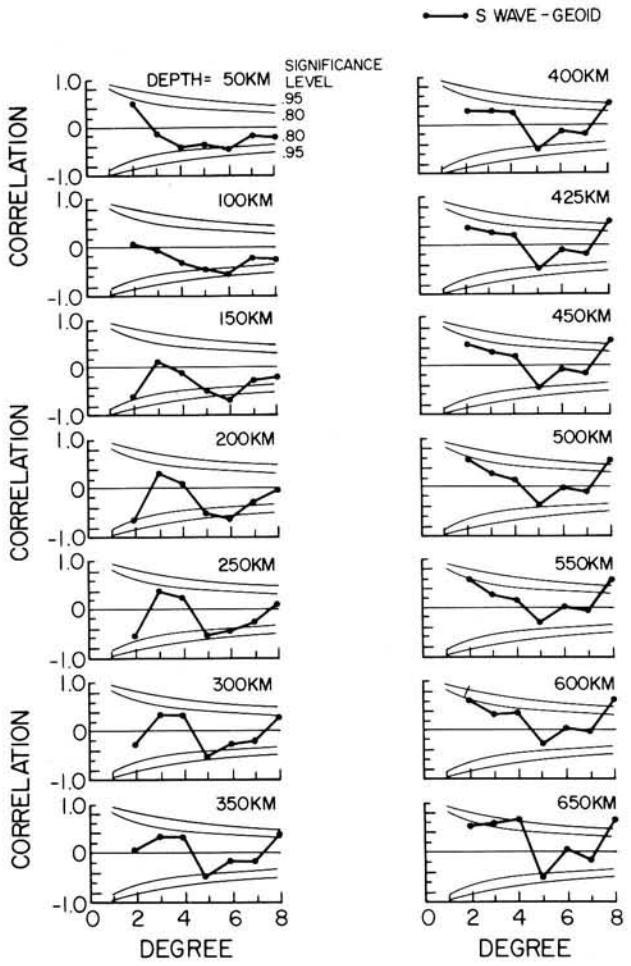

Fig. 14. Degree correlation as a function of depth between the squared shear velocity heterogeneity in model M84C [*Woodhouse and Dziewonski*, 1984] and the corrected, nonhydrostatic, GEM 10B geoid.

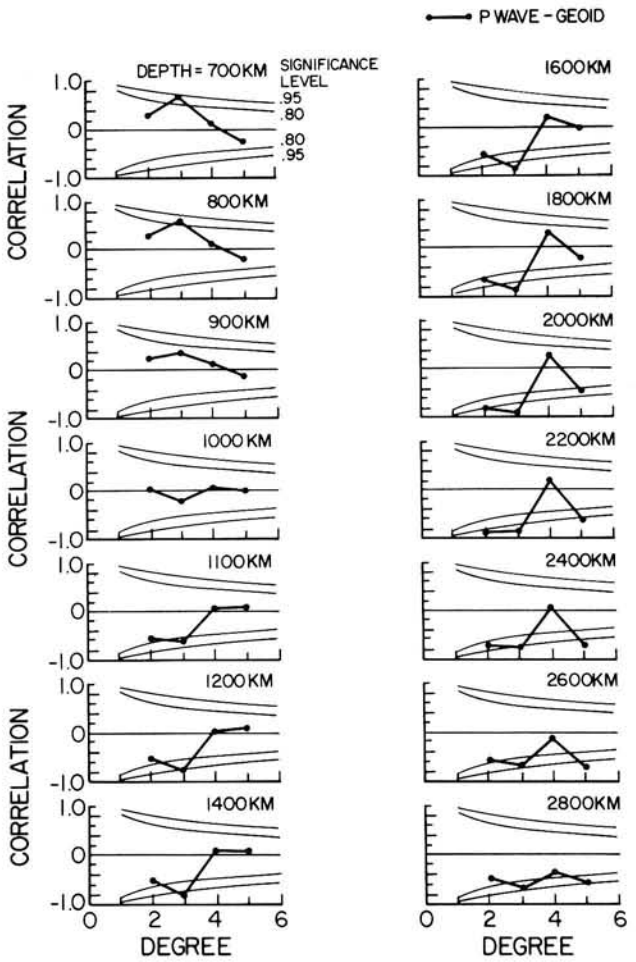

Fig. 15. Degree correlation as a function of depth between the compressional wave velocity heterogeneity in model L02.45 [*Dziewonski*, 1984] and the corrected, nonhydrostatic, GEM 10B geoid.

A further illustration of the flexibility offered by the Green function method is provided by the ease with which we will derive the geoid kernels. It will be very useful to consider first the degree correlations of the nonhydrostatic geoid with the seismically inferred mantle heterogeneities since one may then obtain a rough idea of the shape required of the kernel functions which describe the geoid. In Figures 14 and 15 we show these degree correlations for both the upper and lower mantles. Figures 14 and 15 suggest that the kernels describing the degree 2 and 3 geoid should have maximum (negative) amplitudes in the lower mantle and negligible amplitudes in the upper mantle, while for $l \geq 4$ the geoid kernels should generally have maximum (positive) amplitudes in the midmantle (except for $l = 5$) and negligible amplitudes elsewhere.

The solution of Poisson's equation (equation (18)) is given by the usual volume integral,

$$\phi(\mathbf{r}) = G \int_v \frac{\rho(r')}{|\mathbf{r} - \mathbf{r}'|}\, dV \qquad (28)$$

When the following useful expansion [e.g., *Jackson*, 1975]

$$\frac{1}{|\mathbf{r}-\mathbf{r}'|}=\sum_{l=0}^{\infty}\sum_{m=-l}^{l}\frac{1}{2l+1}\frac{r_<{}^l}{r_>{}^{l+1}}Y_l^m(\theta,\phi)Y_l^{m*}(\theta',\phi')$$

where $r_< = \min(|\mathbf{r}|, |\mathbf{r}'|)$, $r_> = \max(|\mathbf{r}|, |\mathbf{r}'|)$, is inserted into (28), the following expression is obtained for the harmonic coefficients of the interior gravitational potential generated by the internal density heterogeneities in the mantle:

$$(U_{\text{int}})_l^m(r)=\frac{4\pi G}{2l+1}\int_b^a r'^2\frac{r_<{}^l}{r_>{}^{l+1}}(\rho_1)_l^m(r')\,dr' \tag{29}$$

where $b \le r \le a$. Application of result (28) to the effective density heterogeneity produced by the deflected surface boundary at $r = a$ leads to the following expression for the harmonic coefficients of the internal potential generated by the deformed surface:

$$(U_a)_l^m(r)=\frac{4\pi Ga}{2l+1}(\rho_0-\rho_w)\left(\frac{r}{a}\right)^l\delta a_l^m \tag{30}$$

where δa_l^m are the harmonic coefficients of the deformed surface, $\delta a(\theta, \phi)$, at $r = a$, and we have assumed that the mantle of density ρ_0 is overlain by ocean with density ρ_w. Equation (30) is accurate to first order in δa. Similarly, one can show that the interior gravitational potential produced by the deflected core-mantle boundary is given by

$$(U_b)_l^m(r)=\frac{4\pi Gb}{2l+1}(\rho_c-\rho_0)\left(\frac{b}{r}\right)^{l+1}\delta b_l^m \tag{31}$$

where ρ_c is the density of the outer core and the harmonic coefficients describing the deflection field, $\delta b(\theta, \phi)$, of the core-mantle boundary are δb_l^m. If we ignore the (probably significant) contribution to the earth's gravitational potential provided by the deflected phase change boundaries then the total perturbed potential $\phi_1(r)$ is given by

$$(\phi_1)_l^m(r)=(U_{\text{int}})_l^m(r)+(U_a)_l^m(r)+(U_b)_l^m(r) \tag{32}$$

The deflection $\delta a(\theta, \phi)$ of the surface $r = a$ from its reference position is determined from the fact that the surface traction must be continuous across this material interface; to first order this implies the continuity of the σ_{rr} stress tensor component at the bounding surface and the following first-order accurate expression may be derived:

$$\delta a(\theta,\phi)=\frac{P_1(r=a)}{g_0(\rho_0-\rho_w)}-\frac{2\eta}{g_0(\rho_0-\rho_w)}\frac{\partial u_r}{\partial r}\bigg|_{r=a} \tag{33}$$

where P_1 is the perturbed (nonhydrostatic) pressure and $u_r = \hat{r} \cdot \mathbf{u}$. An expression identical to (33) applies to the deflected core-mantle boundary except that ρ_w is replaced by ρ_c and all quantities are evaluated at $r = b$. The nonhydrostatic pressure may be determined from the $\hat{\theta}$ component of the momentum equation (15) where it is evident that the self-gravitation term $\rho_0\mathbf{g}_1$ will have an effect. The details of the derivation for the self-gravitating geoid kernels are presented in Appendix A, where it is shown that

$$(Ge)_l^m=\frac{3}{(2l+1)\bar{\rho}}\int_b^a G_l(r')(\rho_1)_l^m(r')\,dr' \tag{34}$$

where $(Ge)_l^m$ is the harmonic coefficient of the nonhydrostatic geoid field, $\bar{\rho}$ is the average density of the earth, and $G_l(r')$ is the nondimensional geoid kernel. From the expression for the geoid kernel given in Appendix A it is clear that in contrast to the surface divergence field, the geoid anomalies produced by lateral density variations in a homogeneous fluid mantle are independent of the mantle's viscosity.

TABLE 3. Degree Correlations Between Predicted Geoid for a Homogeneous Mantle and Observed Nonhydrostatic Geoid

Degree l	Correlation Coefficient	Significance Level α
$l = 2$	−0.01	$\alpha < 80\%$
$l = 3$	0.53	$\alpha < 80\%$
$l = 4$	−0.51	$80\% < \alpha < 90\%$
$l = 5$	0.60	$\alpha \approx 95\%$

In Figure 13*b* we show profiles of the kernel $G_l(r')$ for various degrees l. The kernels for $l = 2$ and $l = 3$ have peaks in the midmantle, and consequently, according to our previous analysis of the correlations shown in Figures 14 and 15, we do not expect a good correlation between the geoid predicted by (34) and the observed geoid; the degree correlations between these two fields have been calculated and are presented in Table 3. The correlations at $l = 2$ and 3 are poor, as expected, and the correlation at $l = 4$ has the "wrong" sign since the corresponding kernel does not have the required positive amplitude. The best correlation is at $l = 5$ since the corresponding kernel has the negative peak in the midmantle required by the correlations in Figure 14.

The derivation of the kernels for the surface topography in a self-gravitating mantle is relatively straightforward, and the details of the derivation will be found in Appendix A, where it is shown that the spherical harmonic coefficients of the surface topography δa_l^m are given by

$$\delta a_l^m=\frac{1}{(\rho_0-\rho_w)}\int_b^a T_l(r')(\rho_1)_l^m(r')\,dr' \tag{35}$$

where $T_l(r')$ is the dimensionless topography kernel. Profiles of the kernel $T_l(r')$ for several degrees l are presented in Figure 13*c*.

4.2. *Inhomogeneous (Two-Layer) Mantle Green Function*

Microrheological considerations [e.g., *Ranalli and Fischer*, 1984] suggest that the effective Newtonian viscosity of the mantle should increase with depth with the largest increase probably occurring within the lower mantle. The simplest earth model which allows one to investigate the effects of radially varying viscosity is one in which the earth's mantle is divided into two layers having different viscosities. In this section we will derive the Green function for a two-layer mantle and then proceed to a detailed investigation of the surface divergence and geoid anomalies produced by the seismically inferred lateral density variations. As before, we will assume that a whole mantle convective flow exists, and consequently, we do not consider the possibility of layered convection which would imply that the depth of the viscosity jump also coincided with a chemical discontinuity.

In the derivation of the two-layer poloidal flow Green function it is assumed that within each layer the viscosity is constant and the Boussinesq field equations (14) and (15) are also applied to each layer. It is clear therefore that (24) will apply, although the dynamic viscosity η will have a different value in each layer. The delta function loads which excite the response are placed in both the upper and lower layers and thus the problem may be treated in two parts: case 1, to find the poloidal flow Green function for a delta function load in the

lower layer, and case 2, to find the Green function for a delta function load in the upper layer. In each case the mantle consists of three distinct regions which are schematically shown and numbered, for future reference, in Figure 16. The Green function for case 1 will satisfy the equations

$$\begin{aligned} D_l^2(p_L)_l^m(r, r') &= 0 \qquad d < r < a \\ D_l^2(p_L)_l^m(r, r') &= \delta(r - r') \qquad b < r < d \end{aligned} \tag{36}$$

where $r = d$ is the radius at which the viscosity jump occurs. The Green function for case 2 will satisfy the equations

$$\begin{aligned} D_l^2(p_u)_l^m(r, r') &= \delta(r - r') \qquad d < r < a \\ D_l^2(p_u)_l^m(r, r') &= 0 \qquad b < r < d \end{aligned} \tag{37}$$

The Green function satisfying equations (36) and (37) will satisfy free slip (i.e., zero tangential stress) boundary conditions at both $r = a$ (the surface) and $r = b$ (the CMB). One may readily verify that the poloidal flow scalar which satisfies (24) is given by the expression

$$p_l^m(r) = \frac{g_0}{\eta_u}\int_d^a \frac{(\rho_1)_l^m(r')}{r'}(p_u)_l^m(r, r')\,dr' + \frac{g_0}{\eta_L}\int_b^d \frac{(\rho_1)_l^m(r')}{r'}(p_L)_l^m(r, r')\,dr' \tag{38}$$

where $(p_u)_l^m(r, r')$ and $(p_L)_l^m(r, r')$ are the Green functions satisfying equations (37) and (36) and η_u and η_L are the viscosities of the upper and lower layers, respectively. Referring to the numbering scheme for the layers in Figure 16 and using (38), we write

$$p_l^m(r) = \frac{g_0}{\eta_u}\int_r^a \frac{(\rho_1)_l^m(r')}{r'}(p_5)_l^m(r, r')\,dr' + \frac{g_0}{\eta_u}\int_d^r \frac{(\rho_1)_l^m(r')}{r'}(p_4)_l^m(r, r')\,dr' + \frac{g_0}{\eta_L}\int_b^d \frac{(\rho_1)_l^m(r')}{r'}(p_3)_l^m(r, r')\,dr' \qquad d < r < a \tag{39a}$$

and

$$p_l^m(r) = \frac{g_0}{\eta_u}\int_d^a \frac{(\rho_1)_l^m(r')}{r'}(p_6)_l^m(r, r')\,dr' + \frac{g_0}{\eta_L}\int_r^d \frac{(\rho_1)_l^m(r')}{r'}(p_2)_l^m(r, r')\,dr' + \frac{g_0}{\eta_L}\int_b^r \frac{(\rho_1)_l^m(r')}{r'}(p_1)_l^m(r, r')\,dr' \qquad b < r < d \tag{39b}$$

where $(p_5)_l^m(r, r')$ is the Green function $(p_u)_l^m(r, r')$ for the region $d < r < r'$ (layer 5), $(p_4)_l^m(r, r')$ is the Green function $(p_u)_l^m(r, r')$ for the region $r' < r < a$ (layer 4), $(p_3)_l^m(r, r')$ is the Green function $(p_L)_l^m(r, r')$ for the region $d < r < a$ (layer 3), and so on. In Appendix B we present the details of the derivation of the Green functions satisfying (36), (37), the free slip boundary conditions at $r = a$, b, and the appropriate matching conditions at $r = r'$ and $r = d$.

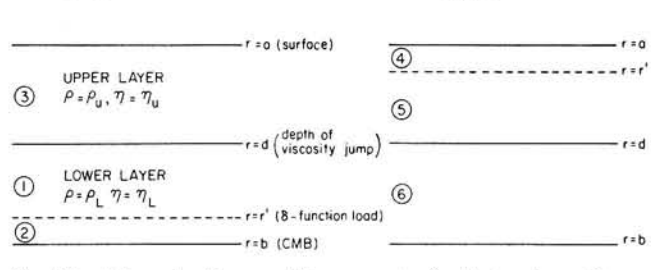

Fig. 16. Schematic diagram of the geometry for the two-layer Green function.

It is a straightforward task to obtain the surface divergence kernel for the two-layer mantle using the poloidal scalar given in (39). In Appendix B we describe the details of the derivation for the divergence kernel where we show that

$$(\nabla_H \cdot \mathbf{u})_l^m(r = a) = \frac{g_0}{\eta_u}\int_b^a S_l(r'; \eta_L/\eta_u, d)(\rho_1)_l^m(r')\,dr' \tag{40}$$

where here we emphasize that the behavior of the kernel S_l also depends on the ratio of the viscosities of the two layers and the depth of the boundary between them. The amplitude of the surface divergence also depends on η_u and thus the surface divergence field (or, equivalently, the surface poloidal scalar in equation (6*a*)) will depend on the absolute value of the viscosity in each layer. The nonhydrostatic geoid (see Appendix B), however, depends only on the ratio of the viscosities of the two layers:

$$(Ge)_l^m = \frac{3}{(2l+1)\bar{\rho}}\int_b^a G_l(r'; \eta_L/\eta_u, d)(\rho_1)_l^m(r')\,dr' \tag{41}$$

where G_l is the nondimensional, self-gravitating geoid kernel.

In our formulation of the two-layer model the radius at which the viscosity change occurs, $r = d$, has been presented as a variable parameter. In past studies of the internal loading problem the boundary between the two layers is almost always placed at the 670-km seismic discontinuity. If one interprets the seismic discontinuity as a manifestation of the spinel-mixed oxides phase change, then microphysical considerations of possible mantle creep mechanisms suggest that an increase in the activation enthalpy produced by the phase change will almost certainly lead to a viscosity increase at 670 km. These microphysical theories of the mantle creep mechanism also suggest that within the lower mantle the viscosity may increase by as much as 2 orders of magnitude [e.g., *Ranalli and Fischer*, 1984], while the maximum viscosity increase at 670 km is expected to be only an order of magnitude [e.g., *Sammis et al.*, 1977]. It does not seem physically reasonable therefore to insist that the entire radial variation of viscosity across the earth's mantle be approximated by a viscosity increase at 670 km depth in a simple two-layer model. We expect instead that a more reasonable alternative would be to place the depth at which the viscosity changes below 670 km (i.e., within the lower mantle) since this may be where the greatest increases in viscosity is most liable to occur. It is for these reasons that we will experiment with several values of the parameter d in (40) and (41).

In Figures 17*a*–17*c* we present several profiles of the surface divergence kernel S_l for the case $d = 5701$ km (i.e., depth $z = 670$ km), and in Figures 17*d*–17*f* we show profiles of the geoid kernel G_l for the same d value. A comparison of the two-layer geoid kernels with those for the homogeneous mantle (Figure 13*b*) shows a very marked change in behavior. Increasing the viscosity of the lower layer produces geoid kernels which are increasingly positive since the deflection of the surface boundary, $r = a$, becomes diminished in amplitude, allowing the effect of the internal density inhomogeneities to dominate the geoid, while in a homogeneous mantle the con-

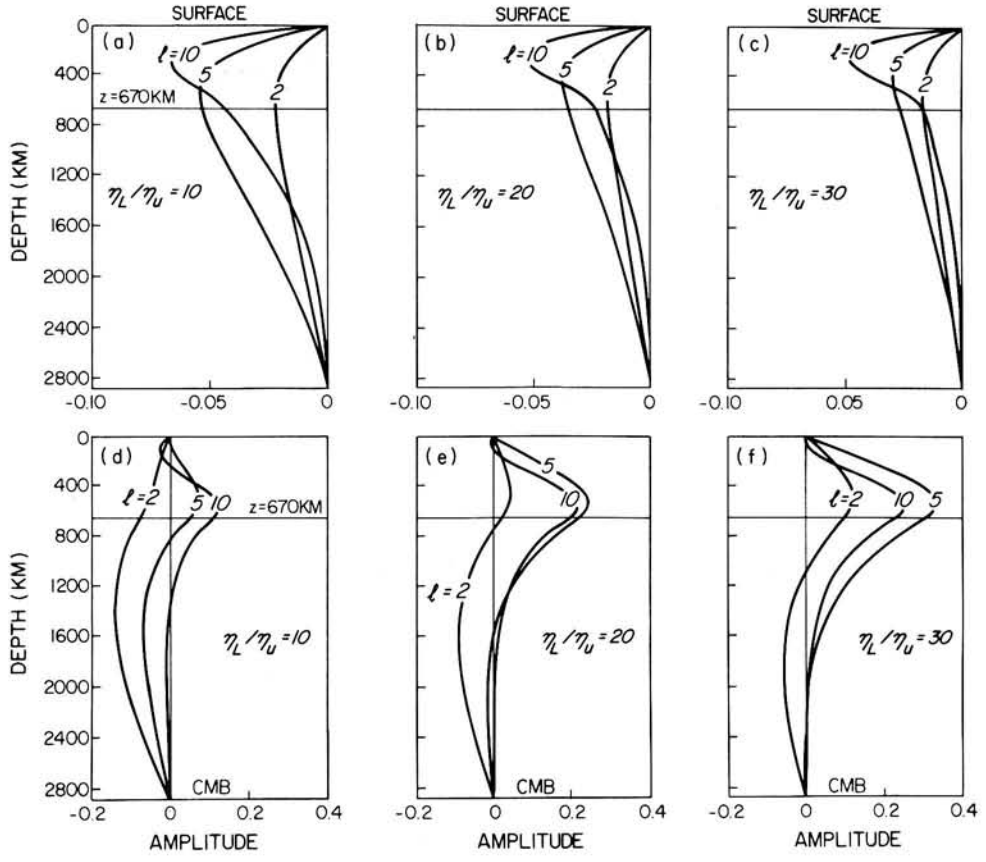

Fig. 17. Kernels for an incompressible, two-layer mantle with free slip conditions at the surface and CMB and viscosity jump at $z = 670$ km. (*a*)–(*c*) Horizontal divergence kernels. (*d*)–(*f*) Geoid kernels for a self-gravitating mantle.

tribution to the geoid from the surface topography always dominates that of the internal mass anomalies, thus producing negative geoid kernels [e.g., *Hager*, 1984]. In Figure 18 we present profiles of the surface divergence and geoid kernels for the case $d = 5171$ km ($z = 1200$ km) where again one may observe that the shape of the divergence kernels is very similar to those of Figures 13*b* or 17. Clearly, the spatial correlation of the geoids predicted from the two-layer model with the observed nonhydrostatic geoid will therefore be very sensitive to changes in the values of d and of η_L/η_u, while the spatial correlation of the predicted surface divergence with the observed surface divergence will not be as sensitive. We do expect, however, that the amplitude of the predicted surface divergence will be quite sensitive to changes in the values d, η_u, and η_L.

We now proceed to a detailed investigation of the degree correlations of the predicted divergence and geoid fields with the corresponding observed fields, and we will also compare the power spectra of the predicted fields with the observed fields. It is our intention to thereby unify the description of the surface plate kinematics (as represented by the surface divergence scalar) with the description of the nonhydrostatic geoid and thus to arrive at a two-layered earth model which best describes both fields simultaneously. In using (40) and (41) to obtain the predicted surface fields we again use models M84C [*Woodhouse and Dziewonski*, 1984] and L02.45 [*Dziewonski*, 1984] to deliver the required lateral variations of density in the earth's mantle.

In Figure 19 we show the degree correlations of the predicted and observed surface divergence fields, and one may see that the correlations are not very sensitive to either η_L/η_u or d, as expected. The degree correlations of the predicted geoid with the observed nonhydrostatic geoid and their dependence on η_L/η_u and d are shown in Figure 20, where one sees that, as expected the spatial correlations are indeed very sensitive to viscosity structure. For the case $z = 670$ km (Figure 20*a*) the best correlations (significance level >90%) for degrees 2 and 3 are for $16 \leq \eta_L/\eta_u \leq 18$, while the correlation at degree 4 is very poor in this range of viscosity ratios and the correlation at degree 5 has the "wrong" sign. A more successful fit, for all degrees, is obtained at $z = 1200$ km (Figure 20*d*) since for $\eta_L/\eta_u = 8$ the correlation coefficients for $l = 2$, 3, 4, and 5 are all positive and moreover the correlations are more than 90% significant for $l = 2$, 3, and 5. The correlation at degree 4 is also much better than for the case $z = 670$ km.

The amplitude of the surface divergence depends not only on η_L/η_u but also on η_u (see equation (40)), and thus to show the complete dependence of the degree variance of the predicted divergence field on the viscosity in a single diagram, we have plotted, in Figure 21, a quantity we call $\log_{10}(\sigma_R)$ versus η_L/η_u, where

$$\log_{10}(\sigma_R) = \log_{10}\left(\frac{\sigma_l(\eta_L/\eta_u)}{\sigma_l(\eta_L/\eta_u = 1)}\right) \tag{42}$$

where $\sigma_l(\eta_l/\eta_u)$ is the degree variance of the predicted surface divergence for a given value of η_L/η_u and $\sigma_l(\eta_L/\eta_u = 1)$ is the degree variance of the predicted field for a uniform (constant viscosity) mantle, and consequently, the ratio σ_R defined in (42) is independent of η_u since in (40), η_u appears as a simple

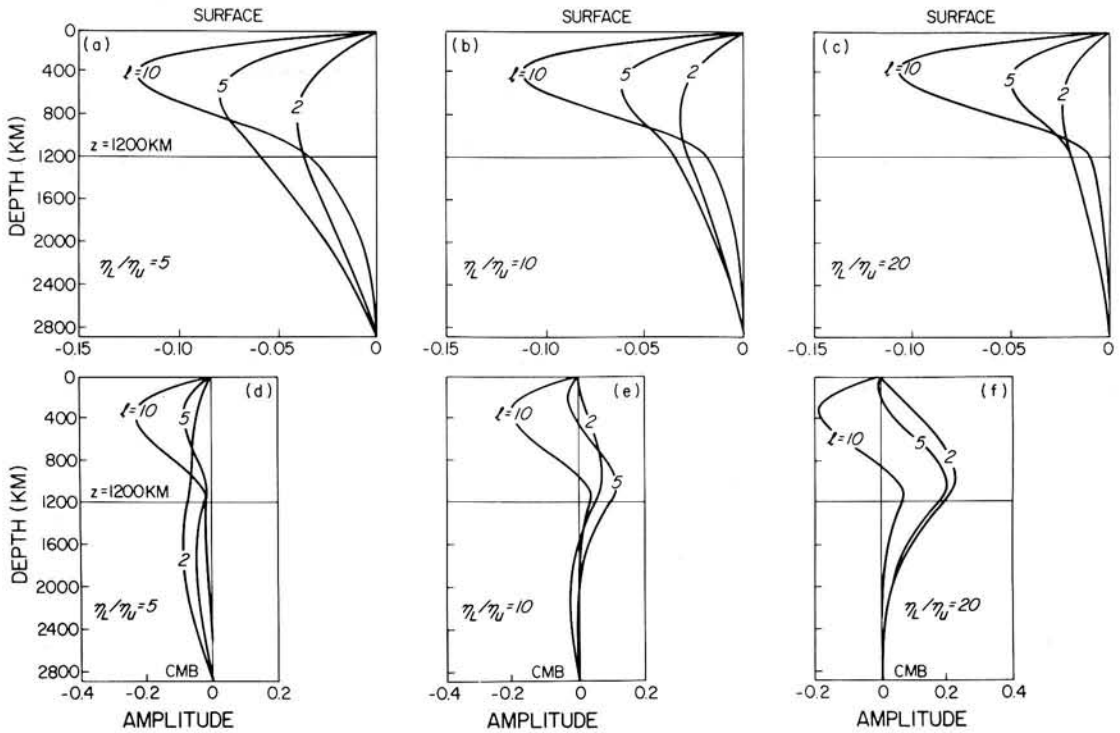

Fig. 18. Kernels for an incompressible, two-layer mantle with free slip conditions at the surface and CMB and viscosity jump at $z = 1200$ km. (*a*)–(*c*) Horizontal divergence kernels. (*d*)–(*f*) Geoid kernels for a self-gravitating mantle.

factor. The observational constraints are introduced by considering the following quantity:

$$\log_{10}(\sigma_0) = \log_{10}\left(\frac{\sigma_l(\text{observed})}{\sigma_l(\eta_l/\eta_u = 1)}\right) \tag{43}$$

where σ_l (observed) is the degree variance of the total observed surface kinetic energy (i.e., poloidal + toroidal; see equation (8)). We include the energy of the toroidal field since we assumed that it is produced by a flux of energy out of the poloidal field. The quantity σ_0 defined in (43) is directly proportional to η_u and is independent of η_L/η_u. In Figure 22 the horizontal dashed lines are plots of $\log_{10}(\sigma_0{}^*)$ for $\eta_u{}^* = 1 \times 10^{21}$ Pa s. It is clear therefore that once an appropriate value of η_L/η_u has been chosen, then a value for η_u may be determined by equating $\log_{10}(\sigma_R)$ with $\log_{10}(\sigma_0)$ (i.e., by matching the predicted and observed kinetic energies) and in Figure 21 this amounts to measuring, for a particular degree l, the "distance" (as measured along the ordinate axis) of a particular point on a $\log_{10}(\sigma_R)$ curve from the $\log_{10}(\sigma_0{}^*)$ line; if

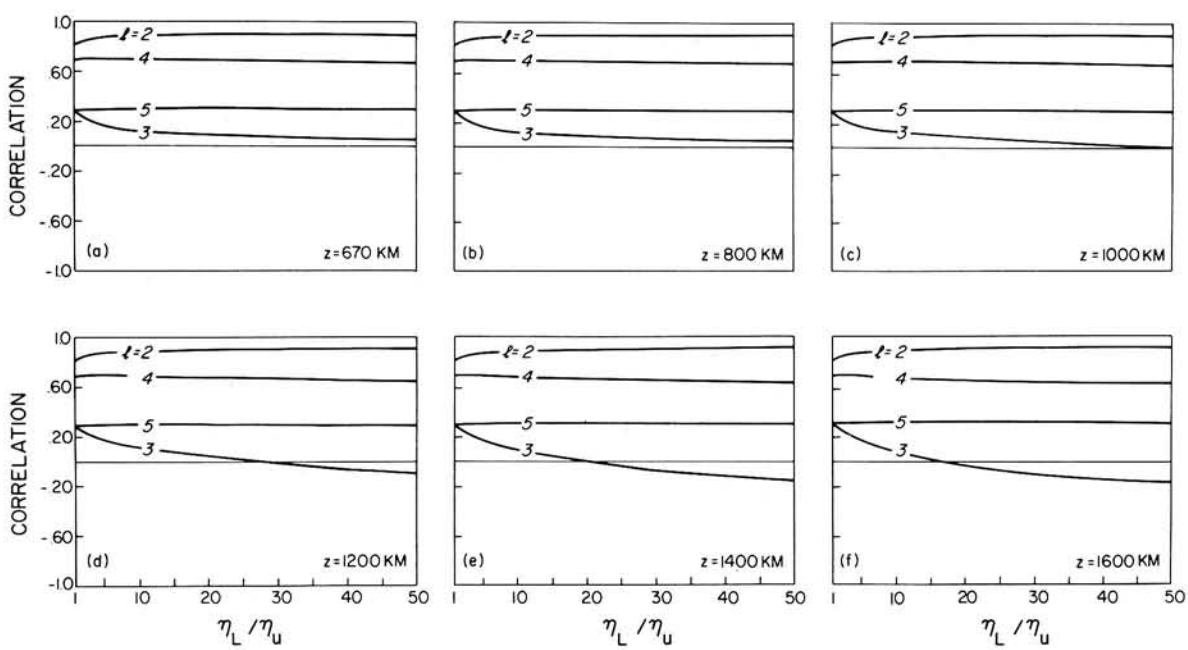

Fig. 19. Degree correlations of observed surface divergence field with the predicted surface divergence field, for a two-layer mantle, as a function of viscosity contrast and depth of viscosity jump.

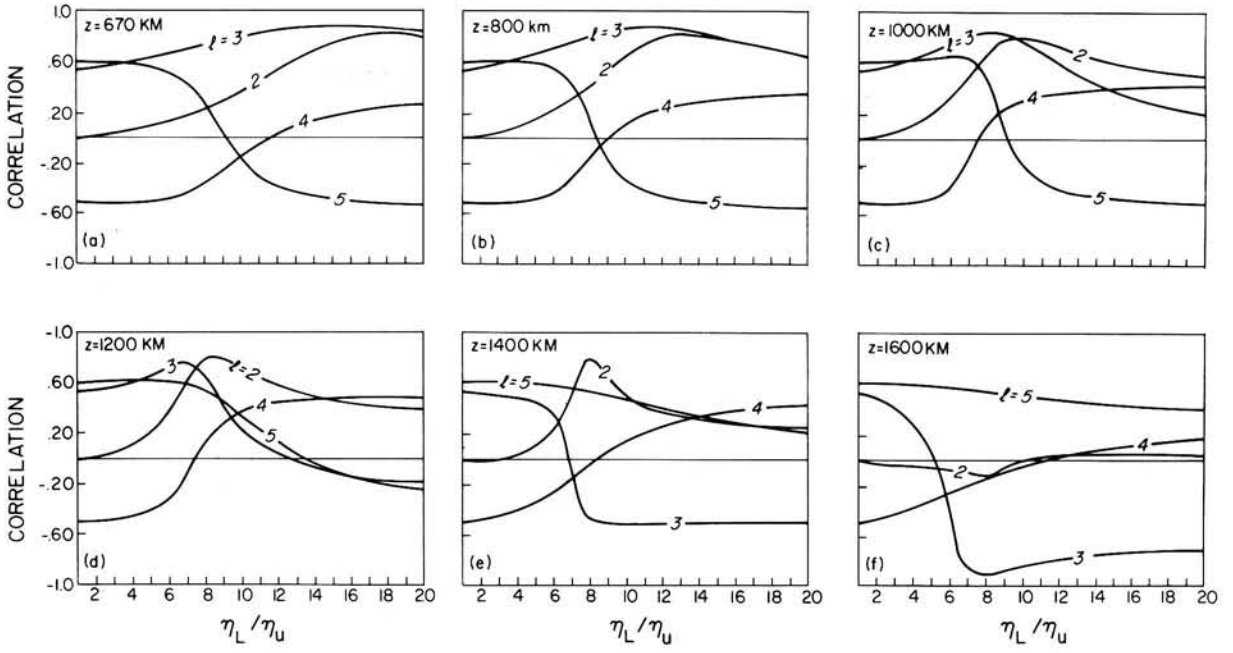

Fig. 20. Degree correlations of corrected, nonhydrostatic, GEM 10B geoid with the predicted geoid, for a two-layer mantle, as a function of viscosity contrast and depth of viscosity jump.

we call this "distance" $\log_{10} d$, then the value of the upper mantle viscosity is $\eta_u = d \times \eta_u^* = d \times 10^{21}$ Pa s. Since the degree correlations of the predicted surface divergence (Figure 19) are rather insensitive to the value of η_L/η_u, the appropriate viscosity ratio will be obtained by considering the predicted geoid field.

In Figure 22 we plot the variation of the degree variances of the predicted geoid field and the horizontal dashed lines are the degree variances of the observed nonhydrostatic (GEM 10B) geoid.

The choice of the best viscosity ratio η_L/η_u and boundary depth d will very much depend on the criterion employed to determine the "best fit." One approach is to choose the viscosity ratio that maximizes the degree correlations. In this approach the optimum viscosity ratio will also vary according the particular degree l that is considered, and thus it is very possible to arrive at apparently conflicting conclusions, as have *Richards and Hager* [1984*b*], who achieve a good fit for their slab geoid ($4 \leq l \leq 9$) with viscosity ratios greater than 30, while a best fit for their residual geoid ($l = 2, 3$) is obtained with a viscosity increase of 10. The different harmonic components of the predicted geoid will be most sensitive to viscosities at different depths in the mantle, and thus a good fit to the observed geoid at all degrees l clearly requires a more

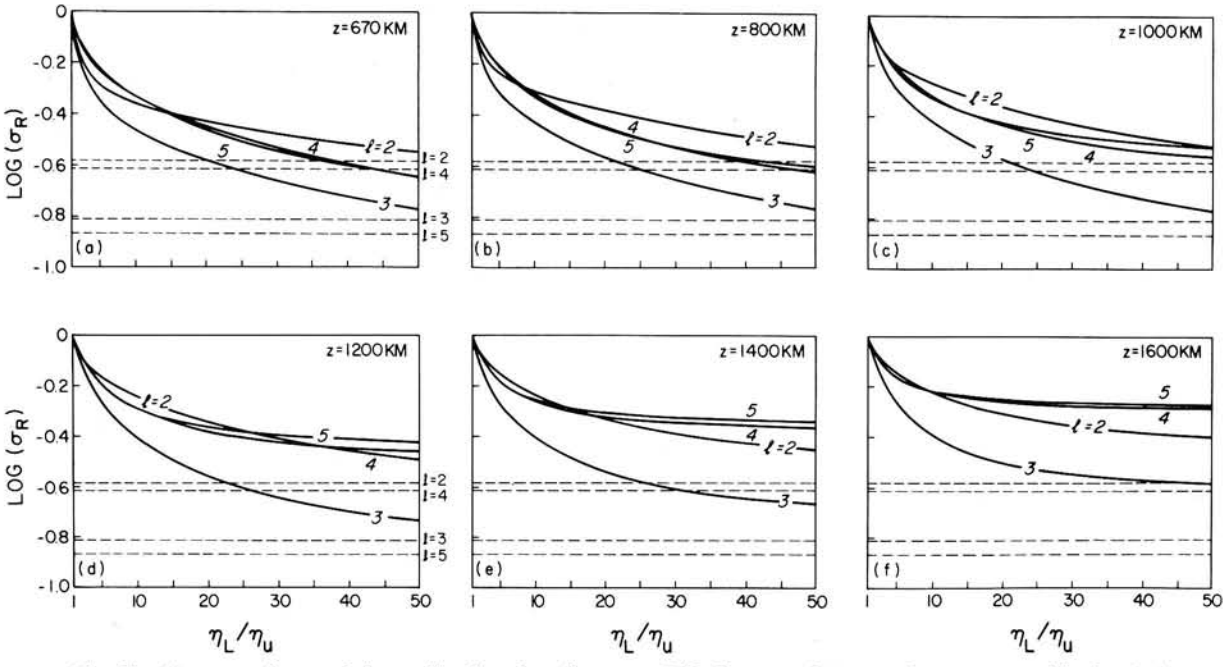

Fig. 21. Degree variances of the predicted surface divergence field, for a two-layer mantle, as measured by log (σ_R) (compare equation (42)) as a function of viscosity contrast and depth of viscosity jump. The dashed horizontal lines are the degree variances of the observed surface divergence field, as measured by log (σ_0)(compare equation (43)).

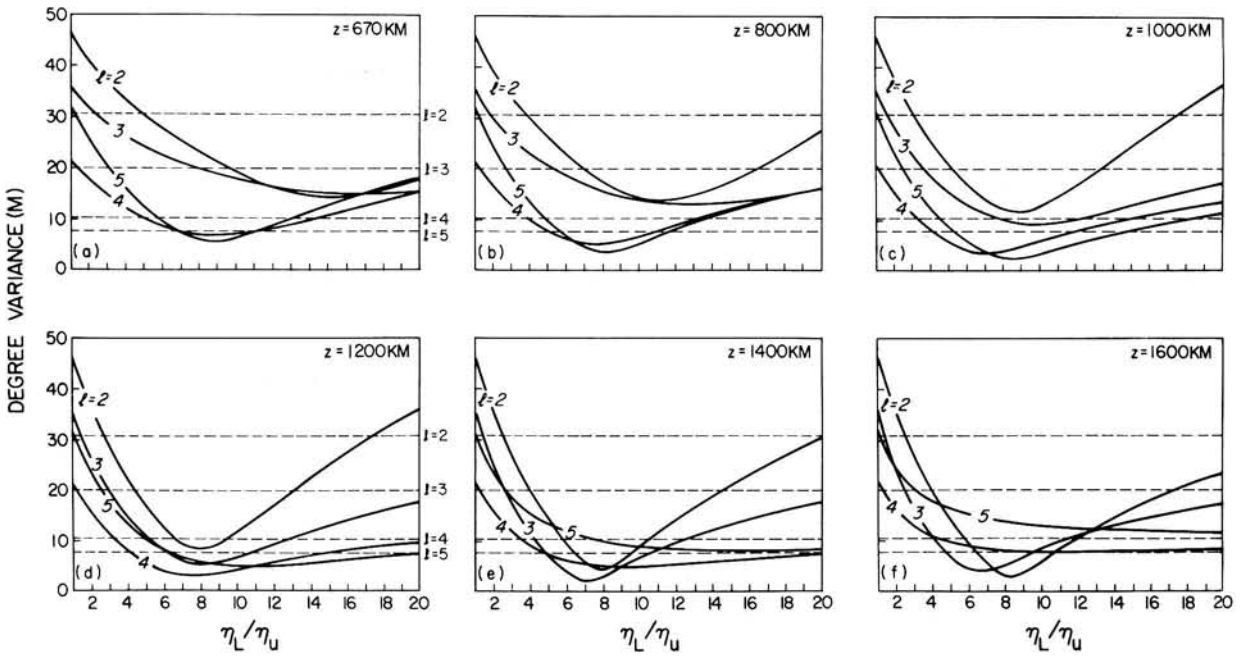

Fig. 22. Degree variances (in meters) of the predicted geoid, for a two-layer mantle, as a function of viscosity contrast and depth of viscosity jump. The dashed horizontal lines are the degree variances of the corrected, nonhydrostatic, GEM 10B geoid.

complicated radial variation in viscosity than is possible in a simple two-layer model.

In the case of a two-layer model a reasonable compromise is achieved by fitting the total predicted geoid synthesized from all available harmonics (i.e., from $l = 2$ to $l = 5$) to the corresponding observed nonhydrostatic geoid. It is possible to introduce an objective measure of "fit" which incorporates the information contained in both the degree variances and degree correlations by defining a root mean square (rms) error δ_{rms} as

$$\delta_{\text{rms}}{}^2 = \frac{1}{4\pi}\int_0^{2\pi}\int_{-1}^{1}[G_p(\theta,\phi) - G_0(\theta,\phi)]^2\, d\cos\theta\, d\phi \qquad (44)$$

where $G_p(\theta, \phi)$ is the predicted geoid field and $G_0(\theta, \phi)$ is the observed nonhydrostatic geoid. If both geoid fields are expanded in terms of spherical harmonics, then one may readily show, from (44), that

$$\delta_{\text{rms}}{}^2 = \sum_l (\sigma_p)_l{}^2 + (\sigma_0)_l{}^2 - 2\rho_l(\sigma_p)_l(\sigma_0)_l \equiv \sum_l \delta_l{}^2 \qquad (45)$$

where $(\sigma_p)_l$ is the degree variance (power) of the predicted geoid, $(\sigma_0)_l$ is the degree variance of the observed geoid, ρ_l is the degree correlation between predicted and observed geoid, and δ_l is the rms error for each degree. In Table 4 we summarize the rms errors obtained when the boundary separating upper and lower layers is at $z = 670$ km and $\eta_L/\eta_u = 18$ (which maximizes the degree correlations). In Table 5 we present the rms errors when $z = 1200$ km and $\eta_L/\eta_u = 8$ (maximum degree correlations). A comparison of Tables 4 and 5 reveals that the best fit to the $l = 2$ and 3 geoid is obtained for the case $z = 670$ km and $\eta_L/\eta_u = 18$, while the best fit to the $\lambda = 4$ and 5 geoid is obtained for the case $z = 1200$ km and $\eta_L/\eta_u = 8$. A slightly better fit to the observed geoid for $2 \le l \le 5$ is achieved for the case $z = 1200$ km and $\eta_L/\eta_u = 8$ and this is entirely due to the much improved fits at $l = 4$ and 5 compared to the case $z = 670$ km. The global fits for the cases $z = 670$ km and $z = 1200$ km are essentially equivalent, and this demonstrates that a trade-off exists between the value of η_L/η_u and the depth of the viscosity jump.

Once the optimum viscosity ratio η_L/η_u has been selected, one may (on the basis of the degree variances of the predicted surface divergence) determine a value of η_u according to the procedure described above, and it is thus possible to estimate the absolute magnitude of the viscosities in the upper and lower layers. Since the best degree correlations between predicted and observed surface divergence are obtained at $l = 2$ and 4, we again try to match the predicted and observed kinetic energies at these degrees to determine the upper mantle viscosity. For the case $z = 670$ km, $\eta_L/\eta_u = 18$, the value of η_u determined from $l = 2$ is 1.47×10^{21} Pa s which agrees well with the value of $\eta_u = 1.55 \times 10^{21}$ Pa s determined from $l = 4$; this agreement shows the self-consistency of our matching method. For the case $z = 1200$ km, $\eta_L/\eta_u = 8$, the

TABLE 4. The rms Errors Between Predicted and Observed Nonhydrostatic Geoid for the Case $z = 670$ km

Degree l	$(\sigma_p)_l$, m	ρ_l	δ_l, m
$l = 2$	15.8	0.82	19.8
$l = 3$	15.2	0.87	10.0
$l = 4$	13.6	0.25	14.8
$l = 5$	16.3	−0.52	21.2

Here $\eta_L/\eta_u = 18$ and $\delta_{\text{rms}} = 34.1$ m.

TABLE 5. The rms Errors Between Predicted and Observed Nonhydrostatic Geoid for the Case $z = 1200$ km

Degree l	$(\sigma_p)_l$, m	ρ_l	δ_l, m
$l = 2$	8.4	0.78	24.6
$l = 3$	5.0	0.65	17.1
$l = 4$	3.0	0.13	10.3
$l = 5$	5.8	0.53	6.6

Here $\eta_L/\eta_u = 8$ and $\delta_{\text{rms}} = 32.3$ m.

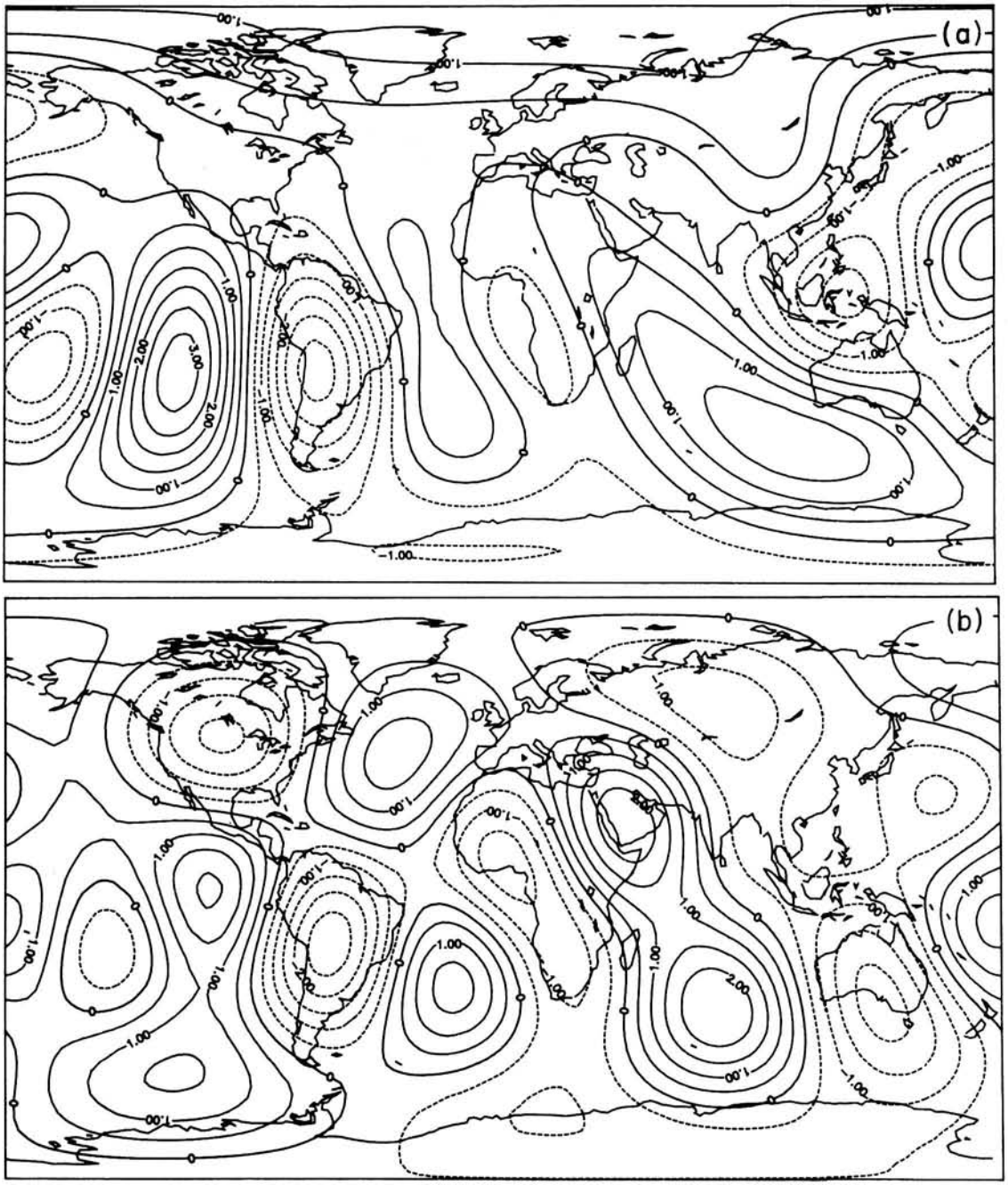

Fig. 23. (*a*) The normalized, observed horizontal divergence of the surface plate velocities synthesized from harmonics in the range $2 \leq l \leq 5$. The total variance of the field shown is exactly unity. The contour interval is 0.5 (dimensionless) units. (*b*) The normalized horizontal divergence predicted using the divergence kernel for a two-layer mantle with a factor of 8 viscosity increase at a depth of 1200 km. The total variance of this field, synthesized from harmonics in the range $2 \leq l \leq 5$, is again exactly unity. The contour interval is as in Figure 23*a*.

value of η_u determined from $l = 2$ is 2.31×10^{21} Pa s which again agrees very well with $\eta_u = 2.26 \times 10^{21}$ Pa s obtained from $l = 4$. A preliminary estimate of the lower mantle viscosity for $z = 670$ km therefore is $\eta_L = 27.2 \times 10^{21}$ Pa s, while for $z = 1200$ km it is $\eta_L = 18.3 \times 10^{21}$ Pa s. On the basis of these results it appears that the value of η_u is not very sensitive to the choice of η_L/η_u, and it seems to have a reasonably well-constrained value of $\eta_u = (2.0 \pm 0.5) \times 10^{21}$ Pa s.

The best correlations between the predicted and observed horizontal divergence fields obtain at $l = 2$ and 4 (compare Figure 19). A more direct illustration of the correspondence between these two fields is given in Figure 23 where we present maps of normalized divergence fields for the degree range $l = 2$–5. Both divergence fields have been normalized according to

$$\nabla_H \cdot \mathbf{u} = \frac{\sum_{l=2}^{5} \sum_{m=-l}^{l} D_l^m Y_l^m Z(\theta, \phi)}{\left[\sum_{l=2}^{5} \sum_{m=-l}^{l} D_l^m D_l^{m*} \right]^{1/2}}$$

where the D_l^m are the harmonic coefficients of the predicted/observed divergence. The fields have been normalized to facilitate a direct comparison between them since the amplitude of the predicted divergence depends on the value of η_u which has been chosen to match the predicted (purely poloi-

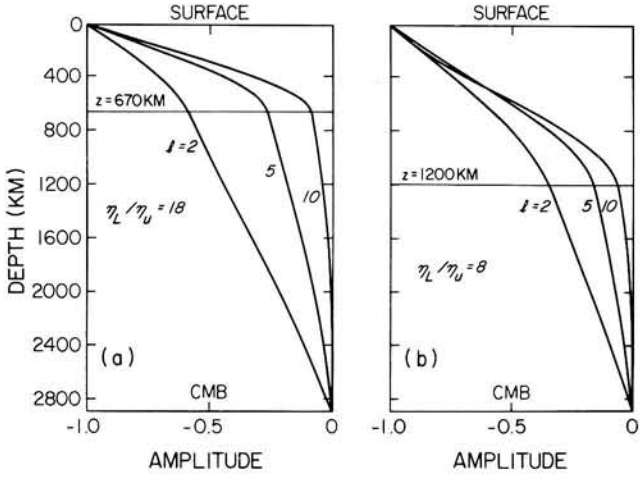

Fig. 24. Topography kernels for a self-gravitating, incompressible, two-layer mantle. Free slip conditions are applied at the surface and CMB.

dal) and observed (poloidal and toroidal) kinetic energies of the surface flow. The agreement between the maps is rather good and the major mismatch between them is due to the continents of North America, Asia, and Australia which are incorrectly shown to be subducting in the predicted divergence map. This is due to an obvious deficiency in our simple viscous flow model which does not include the important effects of lateral variations in chemistry which adds positive buoyancy to these continental blocks.

We complete this discussion of the two-layer mantle by presenting some results for the surface topography field, $\delta a(\theta, \phi)$. In Appendix B we show that the spherical harmonic coefficients of the surface topography produced by internal density anomalies in a self-gravitating mantle are

$$\delta a_l^m = \frac{1}{(\rho_0 - \rho_w)} \int_b^a T_l(r'; \eta_L/\eta_u, d)(\rho_1)_l^m(r')\, dr' \qquad (46)$$

where T_l is the dimensionless topography kernel. From (46) it is clear that the topography, like the geoid, is sensitive only to the ratio of the viscosities of the upper and lower layers. In Figure 24 we present some profiles of the kernel T_l for the cases $\eta_L/\eta_u = 18$ ($z = 670$ km) and $\eta_L/\eta_u = 8$ ($z = 1200$ km). As we point out in section 5, there is a crucial trade-off between the surface topography induced by mantle flow and the viscosity stratification inferred by fitting isostatic geoid anomalies.

5. Discussion and Conclusions

The agreement between the observed surface fields and the fields predicted with our spherically symmetric viscous flow models is encouraging (compare Figure 23). However, in these models the lateral density variations can drive only a poloidal flow, and thus we are unable to reproduce the observed equipartition of kinetic energy between poloidal and toroidal fields at the earth's surface. The generation of toroidal flow may be accomplished by introducing lateral viscosity and/or chemistry variations which then produce a nonlinear coupling of the poloidal and toroidal scalars in the momentum equation. We believe that this coupling will be most important in the near-surface regions of the earth where the lateral variations of rheology and/or chemistry are the most extreme. It follows therefore that in the earth's mantle the internal density heterogeneities will mostly drive a poloidal flow, part of which is then converted to toroidal flow in the near-surface regions and in the process the poloidal flow will itself be modified. In this scenario the near-surface generation of toroidal flow must

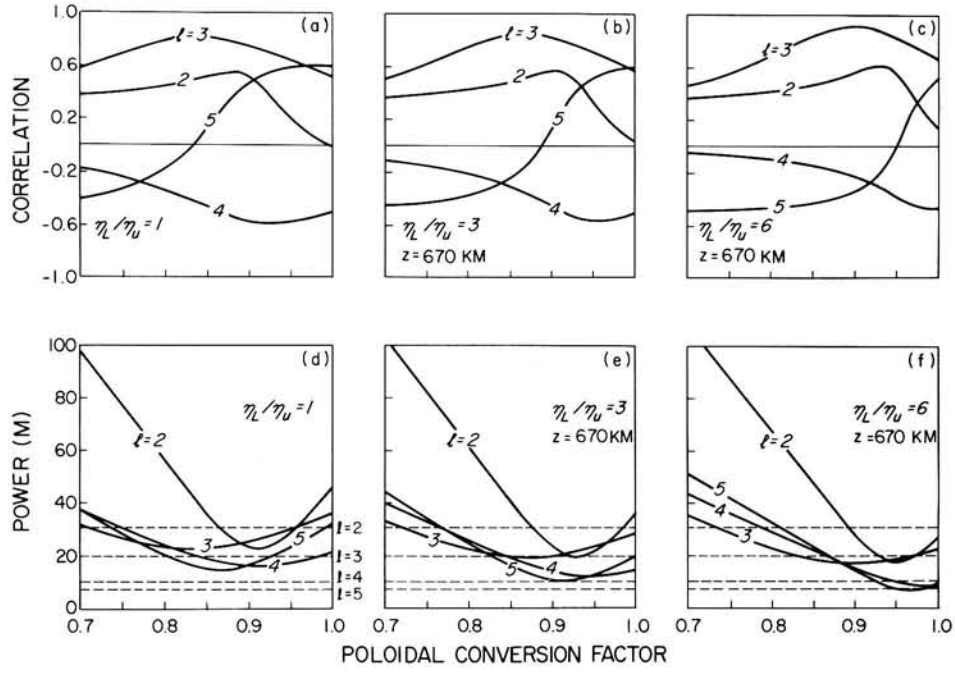

Fig. 25. Behavior of the predicted geoid when poloidal-toroidal coupling at the surface is introduced via a poloidal conversion factor. A conversion factor α simulates a $(1 - \alpha^2) \times 100\%$ flux of energy to the toroidal field. (*a*)–(*c*) Degree correlations of corrected, nonhydrostatic, GEM 10B geoid with predicted geoid as a function of α. (*d*)–(*f*) Degree variances (in meters) of predicted geoid as a function of α. Dashed horizontal lines are degree variances of corrected, nonhydrostatic, GEM 10B geoid.

TABLE 6. Degree Variances of the Predicted Surface Topography

Degree l	Degree Variance, m
$\alpha = 1.0, \eta_L/\eta_u = 1$	
$l = 2$	695
$l = 3$	449
$l = 4$	582
$l = 5$	1012
$\alpha = 1.0, \eta_L/\eta_u = 20, z = 670$ km	
$l = 2$	538
$l = 3$	342
$l = 4$	452
$l = 5$	753
$\alpha = 0.875, \eta_L/\eta_u = 1$	
$l = 2$	542
$l = 3$	371
$l = 4$	486
$l = 5$	856

occur at the expense of the interior poloidal flow, thus resulting in a near-surface poloidal flow of reduced intensity.

The generation of a toroidal flow may seriously compromise the validity of our predicted geoid fields. As noted previously, the predicted geoid will very much depend on the fine balance achieved between opposing contributions from the effective lateral density variations due to the induced surface topography and the internal density heterogeneities. It is of utmost importance therefore that the surface topography be properly modeled if one hopes to predict correctly the geoid field. The greatly improved geoid correlations obtained with the two-layer model are due entirely to the reduction in the amplitude of the surface topography which is produced by increasing the viscosity of the lower layer. We believe that if one also introduces near-surface lateral viscosity/chemistry variations and hence generates toroidal flows by coupling out of the poloidal field, a similar reduction in topography may be achieved since the weaker near-surface poloidal flow will support a reduced topography (we assume that the toroidal flow will itself produce little or no topography). This suggests to us that models incorporating lateral viscosity and/or chemistry variations may allow us to fit the predicted geoid to the observed nonhydrostatic geoid with a smaller viscosity increase at depth than is currently suggested.

We propose the following (admittedly ad hoc) numerical experiment to illustrate this trade-off between the inferred viscosity ratio η_L/η_u and the conversion of poloidal to toroidal flow by introducing the notion of a "poloidal conversion factor" α. With it we can mimic the effect of the flux of energy from poloidal flow to toroidal flow in the near-surface region by simply multiplying the poloidal scalar $p_l^m(r = a)$ by α thus simulating a $(1 - \alpha^2) \times 100\%$ flux of energy to a toroidal flow which we assume contributes little or nothing to the geoid. In Figure 25 we have plotted the variation of both the degree correlations and variances of the predicted geoid as a function of the poloidal conversion factor. It will be observed from Figure 25, for example, that in a constant viscosity mantle (Figures 25*a* and 25*d*) a dramatic improvement in the $l = 2$ geoid is obtained with a conversion factor of only 0.875, and we can trace this improvement directly to the surface topography. In Table 6 we have provided the degree variances of the surface topography field produced by a homogeneous mantle, a homogeneous mantle with a conversion factor $\alpha = 0.875$, and a two-layer mantle with $\eta_L/\eta_u = 20$ and internal boundary at $z = 670$ km. From Table 6 one may see that the very good match between the predicted and observed degree 2 geoids for $\eta_L/\eta_u = 20$ is due to a reduction in surface topography from 695 to 538 m and that an almost identical reduction is achieved in a constant viscosity mantle with only a 23% flux of energy out of the poloidal flow.

An interesting result that has emerged from the analysis of section 4.2 is that the absolute value of the steady state viscosity of the upper mantle, which has been inferred on the basis of the observed energy in the surface plate motions, seems to be practically independent of the value of the lower mantle viscosity which is inferred by also including the geoid data. Thus, although the ultimate viscosity contrast between the upper and lower mantles will remain in doubt until the effects of lateral viscosity/chemistry variations are fully investigated (A. M. Forte and W. R. Peltier, manuscript in preparation, 1986), it appears that a reasonable estimate of the upper mantle viscosity is $\eta_u = (2.0 \pm 0.5) \times 10^{21}$ Pa s. This value of the viscosity is in modest discord with the upper mantle viscosity, $\eta \simeq 1 \times 10^{21}$ Pa s, inferred from glacial isostatic adjustment analyses [e.g., *Peltier*, 1982], and thus one is led to enquire whether the viscosity governing postglacial rebound might represent a transient value [*Peltier*, 1985*b*; *Peltier et al.*, 1986]. *Peltier et al.* [1986] have shown that the transient relaxation provided by the viscoelastic Burger's body rheology will satisfy glacial isostatic adjustment data provided that the elastic defect is large; in this limit the rheology is effectively a Maxwell rheology governed by an effective viscosity η_{eff}, given by

$$\eta_{\text{eff}} = \frac{\eta_1 \eta_2}{\eta_1 + \eta_2} \tag{47}$$

where η_1 is the steady state (e.g., convection time scale) viscosity and η_2 is the transient viscosity. Since the η_{eff} of the upper mantle governing postglacial rebound is known to be near 1×10^{21} Pa s, we may use (47) and our preliminary estimate of $\eta_1 = 2 \times 10^{21}$ Pa s to discover that the transient viscosity in the upper mantle is $\eta_2 = \eta_1 = 2 \times 10^{21}$ Pa s (i.e., $\eta_{\text{eff}} = \frac{1}{2}\eta_1$). We suggest that transient creep experiments on olivine should be performed in an attempt to verify this important prediction.

In summary then, we have shown that the Green function method has enabled us to develop a very simple and straightforward relationship between the convective flow in the earth's mantle (as expressed by the poloidal flow scalar in equations (26) and (38)) and the lateral density variations. In attempting to provide a unified description of both the surface plate motions and the nonhydrostatic geoid we have obtained preliminary estimates of the absolute viscosity values in the mantle. Although the value of the lower mantle viscosity may yet change pending future analyses of the influence of poloidal-toroidal coupling, we find that a reasonable first estimate of the steady state upper mantle viscosity is $\eta_u = (2.0 \pm 0.5) \times 10^{21}$ Pa s.

APPENDIX A: HOMOGENEOUS, INCOMPRESSIBLE MANTLE

A1. *Derivation of the Green Function*

The required Green function must satisfy equation (25), that is,

$$D_l^2 p_l^m(r, r') = \delta(r - r') \tag{A1}$$

When $r \neq r'$, (A1) is the biharmonic equation whose solution is easily found; therefore the solution of (A1) is split in two parts: a solution defined for the region $r' < r \leq a$ and a solution for the region $b \leq r < r'$. These two solutions must then be joined at $r = r'$ by applying the appropriate matching conditions. The biharmonic equation

$$D_l^2 p_l^m(r, r') = 0$$

is a fourth-order differential equation whose solution will consist of the sum of four linearly independent functions:

$$\begin{aligned} p_l^m(r, r') &= A_1 r^l + \frac{B_1}{r^{l+1}} + C_1 r^{l+2} + \frac{D_1}{r^{l-1}} \quad r' < r \leq a \\ p_l^m(r, r') &= A_2 r^l + \frac{B_2}{r^{l+1}} + C_2 r^{l+2} + \frac{D_2}{r^{l-1}} \quad b \leq r < r' \end{aligned} \tag{A2}$$

In (A2) there are eight coefficients which are found by applying the boundary conditions at $r = a$, $r = b$ and the matching conditions at $r = r'$. Two boundary conditions are obtained by requiring that the radial component of the fluid velocity u_r is zero at the deformed bounding surfaces of the fluid layer (which to first-order accuracy may be taken as applying at the underformed, reference positions of the bounding surfaces):

$$\begin{aligned} u_r &= \hat{r} \cdot \mathbf{u} = \hat{r} \cdot (\nabla \times \Lambda p + \Lambda q) \\ &= \frac{1}{r} \Lambda^2 p \end{aligned} \tag{A3}$$

Therefore, from (A3) one sees that if $u_r = 0$ for all θ and ϕ at both $r = a$ and $r = b$, then

$$p_l^m(r, r') = 0 \qquad r = a, b \tag{A4}$$

Two more boundary conditions are obtained by requiring that the shear stresses $\sigma_{r\theta}$ and $\sigma_{r\phi}$ are both zero at $r = a$ and $r = b$, and as shown by *Chandrasekhar* [1961, pp. 224–225], this condition implies that

$$\frac{d^2}{dr^2} p_l^m(r, r') = 0 \qquad r = a, b \tag{A5}$$

Three matching conditions are obtained by requiring that u_r, u_θ (or u_ϕ), and $\sigma_{r\theta}$ (or $\sigma_{r\phi}$) are continuous at $r = r'$; one can therefore show that

$$\begin{aligned} p_l^m(r, r')|_{r=r'^+} &= p_l^m(r, r')|_{r=r'^-} \\ \left.\frac{dp_l^m(r, r')}{dr}\right|_{r=r'^+} &= \left.\frac{dp_l^m(r, r')}{dr}\right|_{r=r'^-} \\ \left.\frac{d^2 p_l^m(r, r')}{dr^2}\right|_{r=r'^+} &= \left.\frac{d^2 p_l^m(r, r')}{dr^2}\right|_{r=r'^-} \end{aligned} \tag{A6}$$

The final matching condition is obtained by integrating equation (A1) from $r = r'^-$ to $r = r'^+$ and using (A6) to obtain

$$\left.\frac{d^3 p_l^m(r, r')}{dr^3}\right|_{r=r'^+} - \left.\frac{d^3 p_l^m(r, r')}{dr^3}\right|_{r=r'^-} = 1 \tag{A7}$$

The eight conditions contained in (A4), (A5), (A6) and (A7) when applied to (A2) then yield the following expressions for the eight coefficients:

$$\begin{aligned} A_1 &= -\frac{D_1}{a^{2l-1}} \qquad B_1 = -C_1 a^{2l+3} \\ C_1 &= \frac{1}{2(2l+3)(2l=1)} \frac{1}{r'^{l-1}} \frac{1-(r'/b)^{2l+3}}{1-(a/b)^{2l+3}} \\ D_1 &= \frac{1}{2(4l^2-1)} \frac{a^{2l-1}}{r'^{l-3}} \frac{1-(r'/b)^{2l-1}}{1-(a/b)^{2l-1}} \end{aligned} \tag{A8}$$

and

$$\begin{aligned} A_2 &= -\frac{D_2}{b^{2l-1}} \qquad B_2 = -C_2 b^{2l+3} \\ C_2 &= -\frac{1}{2(2l+3)(2l+1)} \frac{1}{r'^{l-1}} \frac{1-(r'/a)^{2l+3}}{1-(b/a)^{2l+3}} \\ D_2 &= -\frac{1}{2(4l^2-1)} \frac{b^{2l-1}}{r'^{l-3}} \frac{1-(r'/a)^{2l-1}}{1-(b/a)^{2l-1}} \end{aligned} \tag{A9}$$

In order to obtain expressions for the kernel functions describing surface divergence, geoid height, and surface topography one requires expressions for the derivatives of the poloidal scalar which is given by (26), that is,

$$p_l^m(r) = \frac{g_0}{\eta} \left[\int_r^a \frac{(\rho_1)_l^m(r')}{r'} (p_2)_l^m(r, r')\, dr' + \int_b^r \frac{(\rho_1)_l^m(r')}{r'} (p_1)_l^m(r, r')\, dr' \right] \tag{A10}$$

where $(p_1)_l^m(r, r')$ is the Green function valid for $r' \leq r \leq a$ and $(p_2)_l^m(r, r')$ is the Green function valid for $b \leq r < r'$ (see (A2)). From (A10) one can show, using result (A6), that the Green functions for the first, second, and third derivatives of $p_l^m(r)$ are the first, second, and third derivatives of $p_l^m(r, r')$, respectively.

A2. *Surface Divergence Kernel*

Since $\nabla \cdot \mathbf{u} = 0$, then

$$\nabla_H \cdot \mathbf{u} = -\frac{1}{r^2} \frac{\partial}{\partial r} (r^2 u_r) \tag{A11}$$

Now, to first-order accuracy, $u_r = 0$ at $r = a$, and therefore from (A11) we get

$$\nabla_H \cdot \mathbf{u}(r = a) = -\partial u_r / \partial r|_{r=a} \tag{A12}$$

If one substitutes (A3) into (A12), expands into spherical harmonics, and uses result (A4), then one can show that

$$(\nabla_H \cdot \mathbf{u})_l^m(r = a) = \frac{l(l+1)}{a} \left.\frac{dp_l^m(r)}{dr}\right|_{r=a} \tag{A13}$$

Result (A13) proves equation (6*a*). Now, since

$$\left.\frac{dp_l^m(r)}{dr}\right|_{r=a} = \frac{g_0}{\eta} \int_b^a \frac{(\rho_1)_l^m(r')}{r'} \left.\frac{d(p_1)_l^m(r, r')}{dr}\right|_{r=a} dr' \tag{A14}$$

substitution of (A2) into (A14), and use of (A8), allows one to rewrite (A13) as

$$(\nabla_H \cdot \mathbf{u})_l^m(r = a) = \frac{g_0}{\eta} \int_b^a S_l(r')(\rho_1)_l^m(r')\, dr'$$

where

$$S_l(r') = \frac{a^l l(l+1)}{2(2l+1)}\left[\frac{1}{r'^l}\frac{1-(r'/b)^{2l+3}}{1-(a/b)^{2l+3}} - \frac{1}{a^2 r'^{l-2}}\frac{1-(r'/b)^{2l-1}}{1-(a/b)^{2l-1}}\right]$$

A3. *Geoid Kernel*

If one expands all quantities in (33) in terms of spherical harmonics, then the following result is obtained:

$$\delta a_l{}^m = \frac{1}{g_0(\rho_0-\rho_w)}\left[(P_1)_l{}^m(r=a) - 2\eta\left.\frac{d(u_r)_l{}^m(r)}{dr}\right|_{r=a}\right] \tag{A15}$$

The nonhydrostatic pressure may be obtained from the $\hat{\theta}$ component of the momentum equation (15):

$$\frac{1}{r}\frac{\partial}{\partial\theta}P_1 = \eta\,[\Delta\mathbf{u}]_\theta + \rho_0\frac{1}{r}\frac{\partial\phi_1}{\partial\theta}$$

where one can show from (19), assuming a purely poloidal flow field, that

$$[\Delta\mathbf{u}]_\theta = -\frac{1}{r}\frac{\partial}{\partial\theta}\frac{\partial}{\partial r}r\Delta p$$

and thus if one expands all quantities in terms of spherical harmonics, one can show that

$$(P_1)_l{}^m = -\eta\frac{d}{dr}\left[rD_l p_l{}^m(r)\right] + \rho_0(\phi_1)_l{}^m \tag{A16}$$

where D_l is the transformed Laplacian operator in (24). Now, from (A3) it follows that

$$(u_r)_l{}^m(r) = -\frac{1}{r}\,l(l+1)p_l{}^m(r) \tag{A17}$$

If (A16) and (A17) are substituted into (A15) and use is made of the boundary conditions (A4) and (A5), it follows that

$$\delta a_l{}^m = \frac{1}{(\rho_0-\rho_w)}X_l{}^m(r=a) + \frac{\rho_0}{g_0(\rho_0-\rho_w)}(\phi_1)_l{}^m(r=a) \tag{A18}$$

where

$$X_l{}^m(r) = \frac{\eta}{g_0}\left[-r\frac{d^3}{dr^3} + \frac{3l(l+1)}{r}\frac{d}{dr}\right]p_l{}^m(r) \tag{A19}$$

Similarly, in the case of the core-mantle boundary deflection, $\delta b_l{}^m$, one can show that

$$\delta b_l{}^m = \frac{1}{(\rho_0-\rho_c)}X_l{}^m(r=b) + \frac{\rho_0}{g_0(\pi_0-\rho_c)}(\phi_1)_l{}^m(r=b) \tag{A20}$$

If one now substitutes (A18) into (30) and (A20) into (31) and combines the results in (32), then one may show that

$$(\phi_1)_l{}^m(r) = (U_{\text{int}})_l{}^m(r) = \frac{4\pi aG}{2l+1}\left(\frac{r}{a}\right)^l \cdot\left[X_l{}^m(r=a) + \frac{\rho_0}{g_0}(\phi_1)_l{}^m(r=a)\right] - \frac{4\pi bG}{2l+1}\left(\frac{b}{r}\right)^{l+1}\left[X_l{}^m(r=b) + \frac{\rho_0}{g_0}(\phi_1)_l{}^m(r=b)\right] \tag{A21}$$

In (A21) it is clear that to find $(\phi_1)_l{}^m(r)$, one must know $(\phi_1)_l{}^m(r=a)$ and $(\phi_1)_l{}^m(r=b)$; this is easily accomplished by setting $r=a$ and $r=b$ in (A21), thus producing two simultaneous equations which may be solved to find $(\phi_1)_l{}^m(r=a)$ and $(\phi_1)_l{}^m(r=b)$, and having done this, one may then show that

$$\begin{aligned}(\phi_1)_l{}^m(r) = (U_{\text{int}})_l{}^m(r) = &\left(\frac{r}{a}\right)^l \cdot\left[(1-K_a)(1+K_b) + K_aK_b\left(\frac{b}{a}\right)^{2l+1}\right]^{-1} \\ &\cdot\left\{\left[1+K_b\left(1-\left(\frac{b}{r}\right)^{2l+1}\right)\right]\right. \\ &\cdot\left[K_a(U_{\text{int}})_l{}^m(r=a) + \frac{4\pi aG}{2l+1}X_l{}^m(r=a)\right] \\ &-\left(\frac{b}{a}\right)^{l+1}\left[K_a\left(1-\left(\frac{a}{r}\right)^{2l+1}\right) + \left(\frac{a}{r}\right)^{2l+1}\right] \\ &\left.\cdot\left[K_b(U_{\text{int}})_l{}^m(r=b) + \frac{4\pi bG}{2l+1}X_l{}^m(r=b)\right]\right\}\end{aligned} \tag{A22}$$

where

$$K_a = \frac{4\pi aG}{2l+1}\frac{\rho_0}{g_0} \qquad K_b = \frac{4\pi bG}{2l+1}\frac{\rho_0}{g_0} \tag{A23}$$

When expression (A19) is substituted into (A22), one may then go on to show that

$$(\phi_1)_l{}^m(a) = \frac{4\pi aG}{2l+1}\int_b^a G_l(r')(\rho_1)_l{}^m(r')\,dr' \tag{A24}$$

where

$$\begin{aligned}G_l(r') = &\left[1 - K_a + \frac{K_aK_b}{1+K_b}\left(\frac{b}{a}\right)^{2l+1}\right]^{-1} \\ &\cdot\left(\frac{r'}{a}\right)^{l+2}\left\{1 - \frac{K_a}{1+K_b}\left(\frac{b}{r'}\right)^{2l+1}\left(\frac{b}{a}\right)\right. \\ &+ A_l(r')\left[1 - \frac{K_a}{1+K_b}\left(\frac{b}{a}\right)^{2l+2}\right]\left(\frac{a}{r'}\right)^{l+2} \\ &\left.- B_l(r')\left[1 - \frac{K_a}{1+K_b}\left(\frac{b}{a}\right)\right]\left(\frac{b}{r'}\right)^{l+2}\right\}\end{aligned} \tag{A25}$$

and where

$$\begin{aligned}A_l(r') = &-\frac{l(l+2)}{2l=1}\left(\frac{a}{r'}\right)^{l-2}\frac{1-(r'/b)^{2l-1}}{1-(a/b)^{2l-1}} \\ &+\frac{(l+1)(l-1)}{2l+1}\left(\frac{a}{r'}\right)^l\frac{1-(r'/b)^{2l+3}}{1-(a/b)^{2l+3}}\end{aligned} \tag{A26}$$

$$\begin{aligned}B_l(r') = &-\frac{l(l+2)}{2l=1}\left(\frac{b}{r'}\right)^{l-2}\frac{1-(r'/a)^{2l-1}}{1-(b/a)^{2l-1}} \\ &-\frac{(l+1)(l-1)}{2l+1}\left(\frac{b}{r'}\right)^l\frac{1-(r'/a)^{2l+3}}{1-(b/a)^{2l+3}}\end{aligned} \tag{A27}$$

The nonhydrostatic geoid height field is obtained from $\phi_1(r=a)$ by dividing by g_0, and thus from (A24) one has

$$(Ge)_l{}^m = \frac{3}{2l+1}\frac{1}{\bar{\rho}}\int_b^a G_l(r')(\rho_1)_l{}^m(r')\,dr'$$

where $(Ge)_l^m$ is the harmonic coefficient of the geoid height field, $\bar{\rho}$ is the average density of the earth, and $G_l(r')$ is the geoid kernel given in (A25).

The effects of self-gravitation on the geoid are contained in the constants K_a and K_b which are given in (A23). To obtain the geoid kernels, $G_l(r')$, for a non-self-gravitating mantle one simply sets both K_a and K_b to be zero in (A25).

A4. *Surface Topography Kernel*

The expression for the spherical harmonic coefficients of the surface topography is given in (A18). To determine $X_l^m(r = a)$, one uses (A19) to show that

$$X_l^m(r = a) = \int_b^a C_l(r')(\rho_1)_l^m(r')\, dr' \tag{A28}$$

where

$$C_l(r') = \frac{1}{2l+1}\left[(l+1)(l-1)\left(\frac{a}{r'}\right)^l \frac{1-(r'/b)^{2l+3}}{1-(a/b)^{2l+3}} - l(l+2)\left(\frac{a}{r'}\right)^{l-2}\frac{1-(r'/b)^{2l-1}}{1-(a/b)^{2l-1}}\right] \tag{A29}$$

If one now substitutes (A28) and (A24) into (A18), then the following expression may be obtained:

$$\delta a_l^m = \frac{1}{(\rho_0 - \rho_w)}\int_b^a T_l(r')(\rho_1)_l^m(r')\, dr' \tag{A30}$$

where the dimensionless surface topography kernel is

$$T_l(r') = C_l(r') + \frac{3}{2l+1}\frac{\rho_0}{\bar{\rho}}\, G_l(r') \tag{A31}$$

APPENDIX B: INHOMOGENEOUS (TWO-LAYER), INCOMPRESSIBLE MANTLE

B1. *Derivation of the Green Function*

As in (A2), the Green function $(p_i)_l^m(r, r')$, valid in region i ($i = 1, 2, 3, 4, 5$, and 6; see Figure 16 and equation (39)) is given by the expression

$$(p_i)_l^m(r, r') = A_i r^l + \frac{B_i}{r^{l+1}} + C_i r^{l+2} + \frac{D_i}{r^{l-1}} \tag{B1}$$

For either case 1 or case 2 (Figure 16), equation (B1) shows there are 12 coefficients to be found; they are determined by applying the free slip boundary conditions at $r = a$ and b, by matching conditions at $r = r'$ (see Appendix A), and by applying appropriate matching conditions at $r = d$. Since we assume that a whole mantle flow exists, the conditions that we impose at $r = d$ are continuity of mass flux, normal stress, tangential stress, and tangential velocity:

$$\rho_u u_r|_{r=d^+} = \rho_L u_r|_{r=d^-} \tag{B2a}$$

$$\sigma_{rr}|_{r=d^+} - \sigma_{rr}|_{r=d^-} = (\rho_L - \rho_u) g_0\, \delta d \tag{B2b}$$

$$\sigma_{r\theta}|_{r=d^+} = \sigma_{r\theta}|_{r=d^-} \tag{B2c}$$

$$u_\theta|_{r=d^+} = u_\theta|_{r=d^-} \tag{B2d}$$

where ρ_u and ρ_L are the densities of the upper and lower layers, respectively, and δd is the deflection of the material interface $r = d$ from its reference level. A considerable simplification is made by assuming, as did *Richards and Hager* [1984*a*], that $\rho_u = \rho_L$ (= 4.43 g/cm^3) since then we can ignore the deflection δd in (B2*b*). When the 12 boundary and matching conditions are applied to (B1), we find (after some tedious algebra) that the coefficients of (B1) are given by the following expressions:

$$C_3 = \frac{1}{r'^{l-1}}\, C_3'$$

$$C_3' = \frac{1}{2(2l+1)[G_1G_4(b/d)^4 - G_2G_3]}\left\{\frac{1}{2l+3}\left(\frac{b}{d}\right)^4 \cdot\left[1-\left(\frac{r'}{b}\right)^{2l+3}\right]G_4 - \frac{1}{2l-1}\left(\frac{r'}{d}\right)^2\left(\frac{r'}{b}\right)^{2l-1}\left[1-\left(\frac{b}{r'}\right)^{2l-1}\right]G_2\right\}$$

$$D_3 = r'^{l+2}\, D_3'$$

$$D_3' = \frac{1}{2(2l+1)[G_1G_4(b/d)^4 - G_2G_3]}\left\{-\frac{1}{2l+3}\left(\frac{b}{d}\right)^2\left(\frac{b}{r'}\right)^{2l+1} \cdot\left[1-\left(\frac{r'}{b}\right)^{2l+3}\right]G_3 + \frac{1}{2l-1}\left(\frac{b}{d}\right)^4\left[1-\left(\frac{b}{r'}\right)^{2l-1}\right]G_1\right\}$$

$$B_3 = -a^{l+4}\, B_3' \qquad B_3' = (a/r')^{l-1}\, C_3'$$

$$A_3 = -\frac{1}{a^{l-3}}\, A_3' \qquad A_3' = \left(\frac{r'}{a}\right)^{l+2} D_3'$$

$$C_1 = \frac{1}{r'^{l-1}}\, C_1'$$

$$C_1' = \frac{1}{f + 2l(l+2)}\left[C_3'F_1 + \left(\frac{r'}{d}\right)^{2l+1} D_3'F_2\right]$$

$$D_1 = r'^{l+2}\, D_1'$$

$$D_1' = \frac{1}{h}\left[D_3'F_3 + \left(\frac{d}{r'}\right)^{2l+1} C_3'F_4\right]$$

$$B_1 = r'^{l+4}\, B_1'$$

$$B_1' = \frac{1}{2l+1}\left(\frac{d}{r'}\right)^2\left[D_3'F_6 - C_3'F_5\left(\frac{d}{r'}\right)^{2l+1}\right]$$

$$A_1 = \frac{1}{r'^{l-3}}\, A_1'$$

$$A_1' = \frac{1}{2l+1}\left(\frac{d}{r'}\right)^2\left[C_3'F_7 - D_3'F_8\left(\frac{r'}{d}\right)^{2l+1}\right]$$

$$C_2 = \frac{1}{r'^{l-1}}\, C_2' \qquad C_2' = C_1' - \frac{1}{2(2l+1)(2l+3)}$$

$$D_2 = r'^{l+2}\, D_2' \qquad D_2' = D_1' - \frac{1}{2(2l+1)(2l-1)}$$

$$B_2 = -b^{l+4}\, B_2' \qquad B_2' = \left(\frac{b}{r'}\right)^{l-1} C_2'$$

$$A_2 = -\frac{1}{b^{l-3}}\, A_2' \qquad A_2' = \left(\frac{r'}{b}\right)^{l+2} D_2'$$

where

$$F_1 = \frac{1}{\gamma}\left[f + \gamma 2l(l+2) - (a/b)^{2l+3} l(l+2)(2l+1)(1-\gamma)\right]$$

$$F_2 = l(l+2)(2l-1)\left(\frac{1-\gamma}{\gamma}\right)$$

$$F_3 = \frac{1}{\gamma}\left[2\gamma(l+1)(l-1) + l(2l+1) - (d/a)^{2l-1}(l+1)(l-1)(2l+1)(\gamma^1)\right]$$

$$F_4 = (l+1)(l-1)(2l+3)\left(\frac{\gamma-1}{\gamma}\right)$$

$$F_5 = 2 - \frac{2[f+\gamma 2l(l+2)]}{\gamma[f+2l(l+2)]} + \frac{(2l-1)}{h}(l+1)(l-1)(2l+3) \cdot \left(\frac{\gamma-1}{\gamma}\right) + \left(\frac{a}{d}\right)^{2l+3}(2l+1)\left[1 + \frac{2l(l+2)}{[f+2l(l+2)]}\left(\frac{1-\gamma}{\gamma}\right)\right]$$

$$F_6 = 1 + \frac{2l(l+2)}{[f+2l(l+2)]}\left(\frac{1-\gamma}{\gamma}\right) - \frac{2\gamma(l+1)(l-1) + l(2l+1)}{h\gamma} + \left(\frac{d}{a}\right)^{2l-1}\frac{(l+1)(l-1)(2l+1)}{h}\left(\frac{\gamma-1}{\gamma}\right)$$

$$F_7 = 2l + 3\left[1 - \frac{f+\gamma 2l(l+2)}{\gamma[f+2l(l+2)]} - \frac{2}{h}(l+1)(l-1)\left(\frac{\gamma-1}{\gamma}\right) + \left(\frac{a}{d}\right)^{2l+3}\frac{l(l+2)(2l+1)}{f+2l(l+1)}\left(\frac{1-\gamma}{\gamma}\right)\right]$$

$$F_8 = -2 + \frac{l(l+2)(2l-1)(2l+3)}{f+2l(l+2)}\left(\frac{1-\gamma}{\gamma}\right) + \frac{2}{h}\frac{2\gamma(l+1)(l-1) + l(2l+1)}{\gamma} + \left(\frac{d}{a}\right)^{2l-1}(2l+1)\left[1 + \frac{2}{h}(l+1)(l-1)\left(\frac{1-\gamma}{\gamma}\right)\right]$$

$$G_1 = \frac{F_1}{f+2l(l+2)} - \left(\frac{d}{b}\right)^{2l+3}\frac{F_5}{2l+1}$$

$$G_2 = \frac{F_6}{2l+1} + \left(\frac{b}{d}\right)^{2l+3}\frac{F_2}{f+2l(l+2)}$$

$$G_3 = \frac{F_7}{2l+1} + \left(\frac{d}{b}\right)^{2l-1}\frac{F_4}{h}$$

$$G_4 = \frac{F_3}{h} - \left(\frac{b}{d}\right)^{2l-1}\frac{F_8}{2l+1}$$

and

$$\gamma = \eta_L/\eta_u$$

$$f = 2l^2 + 4l + 3$$

$$h = 4l^2 + l - 2$$

The notation of primed coefficients in the above equations is used to indicate that these quantities are completely dimensionless numbers. For case 2 the coefficients are obtained by straightforward alterations of the coefficients given for case 1. First, we introduce the modifications to F and G defined above and use the notation $\tilde{F}$ and $\tilde{G}$ for the modified versions:

$$\tilde{F}_i = F_i(a \to b,\ \gamma \to 1/\gamma) \qquad i = 1, \cdots, 8$$

where we substitute b for a wherever it occurs and substitute $1/\gamma$ for γ wherever it occurs in F_i; for example,

$$\tilde{F}_1 = \gamma\left[f + \frac{1}{\gamma}2l(l+2) - \left(\frac{b}{d}\right)^{2l+3} l(l+2)(2l+1)\left(1 - \frac{1}{\gamma}\right)\right]$$

Similarly, in the case of G we make the following substitutions:

$$\tilde{G}_i = G_i(F_j \to \tilde{F}_j,\ b \to a) \qquad i = 1, \cdots, 4$$

For example,

$$\tilde{G}_1 = \frac{\tilde{F}_1}{f+2l(l+2)} - \left(\frac{d}{a}\right)^{2l+3}\frac{\tilde{F}_5}{2l+1}$$

Proceeding in this manner, one can verify that the expressions for C_6 and D_6 are analogous to those for C_3 and D_3 in case 1:

$$C_6 = \frac{1}{r'^{l-1}}C_6'$$

$$C_6' = -\frac{1}{2(2l+1)[\tilde{G}_1\tilde{G}_4(a/d)^4 - \tilde{G}_2\tilde{G}_3]}\left\{\frac{1}{2l+3}\left(\frac{a}{d}\right)^4 \cdot \left[1 - \left(\frac{r'}{a}\right)^{2l+3}\right]\tilde{G}_4 - \frac{1}{2l-1}\left(\frac{r'}{d}\right)^2\left(\frac{r'}{a}\right)^{2l-1}\left[1 - \left(\frac{a}{r'}\right)^{2l-1}\right]\tilde{G}_2\right\}$$

$$D_6 = r'^{l+2}D_6'$$

$$D_6' = -\frac{1}{2(2l+1)[\tilde{G}_1\tilde{G}_4(a/d)^4 - \tilde{G}_2\tilde{G}_3]}\left\{-\frac{1}{2l+3}\left(\frac{a}{d}\right)^2\left(\frac{a}{r'}\right)^{2l+1} \cdot \left[1 - \left(\frac{r'}{a}\right)^{2l+3}\right]\tilde{G}_3 + \frac{1}{2l-1}\left(\frac{a}{d}\right)^4\left[1 - \left(\frac{a}{r'}\right)^{2l-1}\right]\tilde{G}_1\right\}$$

The remaining coefficients are

$$B_6 = -b^{l+4}B_6' \qquad B_6' = (b/r')^{l-1}C_6'$$

$$A_6 = -\frac{1}{b^{l-3}}A_6' \qquad A_6' = \left(\frac{r'}{b}\right)^{l+2}D_6'$$

$$C_5 = \frac{1}{r'^{l-1}} \qquad C_5' = \frac{1}{f+2l(l+2)}\left[C_6'\tilde{F}_1 + \left(\frac{r'}{d}\right)^{2l+1}D_6'\tilde{F}_2\right]$$

$$D_5 = r'^{l+2}D_5' \qquad D_5' = \frac{1}{h}\left[D_6'\tilde{F}_3 + \left(\frac{d}{r'}\right)^{2l+1}C_6'\tilde{F}_4\right]$$

$$B_5 = r'^{l+4}B_5' \qquad B_5' = \frac{1}{2l+1}\left(\frac{d}{r'}\right)^2\left[D_6'\tilde{F}_6 - C_5'\tilde{F}_5\left(\frac{d}{r'}\right)^{2l+1}\right]$$

$$A_5 = \frac{1}{r'^{l-3}}A_5'$$

$$A_5' = \frac{1}{2l+1}\left(\frac{d}{r'}\right)^2\left[C_6'\tilde{F}_7 - D_6'\tilde{F}_8\left(\frac{r'}{d}\right)^{2l+1}\right]$$

$$C_4 = \frac{1}{r'^{l-1}}C_4' \qquad C_4' = C_5' + \frac{1}{2(2l+1)(2l+3)}$$

$$D_4 = r'^{l+2}D_4' \qquad D_4' = D_5' + \frac{1}{2(2l+1)(2l-1)}$$

$$B_4 = -a^{l+4}B_4' \qquad B_4' = (a/r')^{l-1}C_4'$$

$$A_4 = -\frac{1}{a^{l-3}}A_4' \qquad A_4' = \left(\frac{r'}{a}\right)^{l+2}D_4'$$

where, again, the primed coefficients are dimensionless numbers.

B2. *Surface Divergence Kernel*

To determine the surface divergence field in a two-layer mantle, we again use (A13) from Appendix A. The radial derivative of the poloidal scalar at $r = a$ is obtained from (39*a*):

$$\left.\frac{dp_l^m}{dr}\right|_{r=a} = \frac{g_0}{\eta_u}\int_d^a \left.\frac{d(p_4)_l^m(r, r')}{dr}\right|_{r=a} \frac{(\rho_1)_l^m(r')}{r'}\,dr' + \frac{g_0}{\eta_L}\int_b^d \left.\frac{d(p_3)_l^m(r, r')}{dr}\right|_{r=a} \frac{(\rho_1)_l^m(r')}{r'}\,dr' \tag{B3}$$

Using (B1) and the coefficients tabulated in section B.1, one can show, using (A13) with (B3), that

$$(\nabla_H \cdot \mathbf{u})_l^m(r = a) = \frac{g_0}{\eta_u}\int_b^a S_l(r'; \gamma, d)(\rho_1)_l^m(r')\,dr' \tag{B4}$$

where

$$S_l(r'; \gamma, d) = p'(4) \qquad d \le r' \le a$$

$$S_l(r'; \gamma, d) = \frac{1}{\gamma}\,p'(3) \qquad b \le r' \le d$$

where

$$p'(i) = l(l+1)\left[-l\left(\frac{a}{r'}\right)A_i' + (l+1)\left(\frac{a}{r'}\right)B_i' + (l+2)\left(\frac{a}{r'}\right)^l C_i' - (l-1)\left(\frac{r'}{a}\right)^{l+1} D_i'\right]$$

B3. *Geoid Kernel*

In our two-layer model we have assumed, for simplicity, that the densities of the upper and lower layers are equal, and therefore any deflection of the interface $r = d$ will not affect the perturbed potential ϕ_1; consequently, (A22) of Appendix A will also be valid for the two-layer earth. The first task is thus to determine the kernels for the quantities $X_l^m(r = a)$ and $X_l^m(r = b)$. From (A19) we have

$$X_l^m(r = a) = \frac{\eta_u}{g_0}\left[-r\frac{d^3}{dr^3} + \frac{3l(l+1)}{r}\frac{d}{dr}\right]p_l^m(r)|_{r=a} \tag{B5a}$$

$$X_l^m(r = b) = \frac{\eta_L}{g_0}\left[-r\frac{d^3}{dr^3} + \frac{3l(l+1)}{r}\frac{d}{dr}\right]p_l^m(r)|_{r=b} \tag{B5b}$$

If one substitutes (39*a*) into (B5*a*), then the following expression is obtained:

$$X_l^m(r = a) = \int_b^a K_l^a(r')(\rho_1)_l^m(r')\,dr' \tag{B6}$$

where

$$K_l^a(r') = p_1''(4) \qquad d \le r' \le a$$

$$K_l^a(r') = \frac{1}{\gamma}\,p_1''(3) \qquad b \le r' \le d$$

where

$$p_1''(i) = 2\left[-l(l^2+3l-1)\left(\frac{a}{r'}\right)A_i' + (l+1)(l^2-l-3)\left(\frac{a}{r'}\right)B_i' + l(l+1)(l+2)\left(\frac{a}{r'}\right)^l C_i' - l(l+1)(l-1)\left(\frac{r'}{a}\right)^{l+1} D_i'\right]$$

Similarly, if one substitutes (39*b*) into (B5*b*), it can be shown that

$$X_l^m(r = b) = \int_b^a K_l^b(r')(\rho_1)_l^m(r')\,dr' \tag{B7}$$

where

$$K_l^b(r') = \gamma p_2''(6) \qquad d \le r' \le a$$

$$K_l^m(r') = p_2''(2) \qquad b \le r' \le d$$

where

$$p_2''(i) = 2\left[-l(l^2+3l-1)\left(\frac{b}{r'}\right)A_i' + (l+1)(l^2-l-3)\left(\frac{b}{r'}\right)B_i' + l(l+1)(l+2)\left(\frac{b}{r'}\right)^l C_i' - l(l+1)(l-1)\left(\frac{r'}{b}\right)^{l+1} D_i'\right]$$

If one sets $r = a$ in (A22) and substitutes (B6) and (B7) into the resulting equation, the following expression for the self-gravitating potential is obtained:

$$(\phi_1)_l^m(a) = \frac{4\pi a G}{2l+1}\int_b^a G_l(r'; \gamma, d)(\rho_1)_l^m(r')\,dr' \tag{B8}$$

where

$$G_l(r'; \gamma, d) = (r'/a)^{l+1}\{1 + [(1 - K_a)(1 + K_b) + K_aK_b(b/a)^{2l+1}]^{-1}[[1 + K_b(1 - (b/a)^{2l+1})] \cdot [K_a + (a/r')^{l+2}K_l^a(r')] - (b/r')^{l+2}[K_b(b/r')^{l-1} + K_l^b(r')]]\} \tag{B9}$$

where the constants K_a and K_b are defined in (A22). The spherical harmonic coefficients of the nonhydrostatic geoid $(G_e)_l^m$ are directly obtained from (B8) by dividing by g_0:

$$(G_e)_l^m = \frac{3}{2l+1}\frac{1}{\bar{\rho}}\int_b^a G_l(r'; \gamma, d)(\rho_1)_l^m(r')\,dr'$$

where $\bar{\rho}$ is the average density of the earth and $G_l(r'; \gamma, d)$ is the dimensionless geoid kernel given in (B9).

B4. *Surface Topography Kernel*

Once the geoid kernel has been obtained, it is a simple task to obtain the kernel for the surface topography as shown in section A4 of Appendix A. From (A30) and (A31) one obtains the harmonic coefficients of the surface topography in a two-layer mantle:

$$\delta a_l^m = \frac{1}{(\rho_0 - \rho_w)}\int_b^a T_l(r'; \gamma, d)(\rho_1)_l^m(r')\,dr' \tag{B10}$$

where the dimensionless topography kernel is

$$T_l(r'; \gamma, d) = K_l^a(r') + \frac{3}{2l+1}\frac{\rho_0}{\bar{\rho}}G_l(r'; \gamma, d) \tag{B11}$$

APPENDIX C: HARMONIC COEFFICIENTS OF THE HORIZONTAL DIVERGENCE AND OF THE RADIAL VORTICITY

In Table C1 the first component of each coefficient is the real part, while the second component is the imaginary part. The complex spherical harmonic basis functions employed to compute these coefficients are normalized according to equation (23). All the coefficients have units of radians per year.

TABLE C1. Spherical Harmonic Coefficients of the Horizontal Divergence and the Radial Vorticity

	Surface Divergence	Radial Vorticity
L= 0 M= 0	(-.1276E-11, .0000E+00)	(-.7595E-12, .0000E+00)
L= 1 M= 0	(-.4297E-08, .0000E+00)	(-.4198E-08, .0000E+00)
L= 1 M= 1	(-.1907E-08,-.2741E-08)	(-.8511E-09, .1991E-08)
L= 2 M= 0	(.1671E-08, .0000E+00)	(-.2831E-08, .0000E+00)
L= 2 M= 1	(-.1989E-08,-.1498E-08)	(-.3527E-08, .1085E-08)
L= 2 M= 2	(-.7776E-09,-.4086E-08)	(.1806E-09, .1459E-08)
L= 3 M= 0	(.1671E-08, .0000E+00)	(.1418E-08, .0000E+00)
L= 3 M= 1	(.2967E-09, .1666E-08)	(-.1850E-08,-.8071E-09)
L= 3 M= 2	(.1434E-08, .1487E-08)	(-.1497E-08, .1092E-08)
L= 3 M= 3	(-.1751E-08,-.1187E-08)	(.8667E-09, .1544E-08)
L= 4 M= 0	(-.6761E-09, .0000E+00)	(.3436E-08, .0000E+00)
L= 4 M= 1	(-.1895E-08, .4615E-09)	(-.2710E-09, .4106E-09)
L= 4 M= 2	(-.1429E-08, .9861E-09)	(.7495E-09,-.7679E-09)
L= 4 M= 3	(.3319E-08, .2207E-09)	(.1430E-09, .1794E-08)
L= 4 M= 4	(.1838E-09, .4437E-08)	(.5018E-09, .5685E-09)
L= 5 M= 0	(.2798E-08, .0000E+00)	(-.1275E-09, .0000E+00)
L= 5 M= 1	(-.1171E-09,-.5437E-09)	(.2436E-08, .5064E-09)
L= 5 M= 2	(-.1529E-08,-.7218E-09)	(-.1638E-08, .8328E-09)
L= 5 M= 3	(-.2472E-08,-.1280E-08)	(.1089E-08,-.3282E-08)
L= 5 M= 4	(.7137E-09,-.3081E-08)	(.5649E-10,-.4665E-10)
L= 5 M= 5	(.2637E-08, .6067E-09)	(-.1219E-08,-.1507E-08)
L= 6 M= 0	(-.6579E-09, .0000E+00)	(-.2069E-08, .0000E+00)
L= 6 M= 1	(.7742E-09, .1281E-08)	(-.8366E-10, .2505E-09)
L= 6 M= 2	(-.7488E-10, .1364E-09)	(-.3946E-09, .4216E-09)
L= 6 M= 3	(.1545E-09,-.6487E-09)	(-.3186E-09, .1678E-08)
L= 6 M= 4	(-.2336E-09, .3703E-09)	(.4986E-09,-.1585E-08)
L= 6 M= 5	(-.6265E-10, .3363E-09)	(-.1311E-09,-.8453E-09)
L= 6 M= 6	(.9108E-09,-.2619E-08)	(-.6161E-10,-.1504E-08)
L= 7 M= 0	(.8730E-11, .0000E+00)	(.2269E-08, .0000E+00)
L= 7 M= 1	(.4306E-09,-.1305E-10)	(-.1209E-08,-.6343E-09)
L= 7 M= 2	(-.6442E-09, .8977E-09)	(-.1237E-09,-.3143E-09)
L= 7 M= 3	(-.8011E-09, .3687E-10)	(-.1559E-08, .7356E-09)
L= 7 M= 4	(.5058E-09,-.3914E-09)	(.1499E-08, .3401E-09)
L= 7 M= 5	(.7913E-09, .9884E-09)	(.6161E-09, .2610E-09)
L= 7 M= 6	(-.8902E-09, .2294E-08)	(-.2172E-09,-.3563E-10)
L= 7 M= 7	(-.2176E-08,-.1108E-08)	(.5833E-09, .7307E-09)
L= 8 M= 0	(.7173E-09, .0000E+00)	(-.9497E-09, .0000E+00)
L= 8 M= 1	(.1052E-08,-.1183E-08)	(.1369E-08,-.1081E-08)
L= 8 M= 2	(.1491E-08, .3129E-09)	(.1860E-09,-.4102E-09)
L= 8 M= 3	(-.1907E-09, .7263E-09)	(-.1177E-08,-.1310E-09)
L= 8 M= 4	(.2410E-09,-.2488E-09)	(-.1639E-08, .5710E-09)
L= 8 M= 5	(.4674E-09,-.8488E-09)	(.5953E-09,-.1568E-10)
L= 8 M= 6	(-.8065E-10, .2182E-09)	(-.6951E-09, .1300E-08)
L= 8 M= 7	(-.8440E-10, .1416E-08)	(-.3749E-09, .6116E-09)
L= 8 M= 8	(-.1412E-08, .1650E-08)	(.3367E-09, .1327E-08)
L= 9 M= 0	(-.2952E-09, .0000E+00)	(-.1512E-08, .0000E+00)
L= 9 M= 1	(-.1823E-10,-.6354E-09)	(.4113E-09, .1234E-08)
L= 9 M= 2	(.5506E-09, .1113E-09)	(.8465E-09,-.3895E-09)
L= 9 M= 3	(.9306E-10, .3984E-09)	(.9054E-09,-.4211E-09)
L= 9 M= 4	(-.2359E-09, .1171E-08)	(-.7269E-11,-.7355E-09)
L= 9 M= 5	(.1100E-08,-.7648E-09)	(-.4328E-09,-.4141E-09)
L= 9 M= 6	(.9819E-09, .4691E-09)	(-.6402E-09, .2938E-09)
L= 9 M= 7	(-.4490E-09,-.5908E-09)	(-.1396E-10, .1069E-08)
L= 9 M= 8	(.6942E-09,-.1044E-08)	(-.3451E-09, .6044E-10)
L= 9 M= 9	(.1393E-08, .4077E-09)	(.2523E-09,-.2865E-09)
L=10 M= 0	(.2539E-09, .0000E+00)	(.4114E-09, .0000E+00)
L=10 M= 1	(.6282E-09, .5451E-09)	(.2849E-09, .3729E-09)
L=10 M= 2	(.2771E-09,-.4306E-09)	(.2691E-09, .1975E-09)
L=10 M= 3	(-.6788E-09, .3871E-09)	(.5213E-09,-.2176E-09)
L=10 M= 4	(-.1788E-08,-.3453E-09)	(.4112E-09,-.8967E-10)
L=10 M= 5	(.1800E-10,-.4938E-09)	(-.2939E-09,-.1454E-08)
L=10 M= 6	(.3185E-09,-.4415E-09)	(.4866E-09,-.1973E-08)
L=10 M= 7	(.1556E-08, .8669E-09)	(-.1114E-08,-.1214E-09)
L=10 M= 8	(-.9438E-09,-.5855E-09)	(.2044E-09,-.1319E-09)
L=10 M= 9	(.1162E-09,-.3864E-09)	(-.5075E-10,-.7745E-09)
L=10 M=10	(.1165E-08, .9419E-11)	(.1843E-09,-.2680E-09)
L=11 M= 0	(-.1803E-08, .0000E+00)	(-.3022E-09, .0000E+00)
L=11 M= 1	(-.2134E-09, .1377E-08)	(-.2119E-09,-.4407E-09)
L=11 M= 2	(.3804E-09, .1384E-09)	(.3374E-09,-.3440E-09)
L=11 M= 3	(.1138E-08, .1980E-09)	(-.1667E-09, .4142E-09)
L=11 M= 4	(.5743E-09, .8229E-09)	(-.3551E-09, .7699E-09)
L=11 M= 5	(-.1277E-08, .3206E-09)	(.4310E-09,-.1470E-09)
L=11 M= 6	(.2238E-09,-.3061E-09)	(-.6235E-09,-.6607E-09)
L=11 M= 7	(-.4639E-09, .7759E-09)	(-.2713E-09,-.1271E-08)
L=11 M= 8	(.5618E-09,-.3357E-09)	(-.1048E-08,-.1765E-09)

TABLE C1. (continued)

	Surface Divergence	Radial Vorticity
L=11 M= 9	(-.1488E-08,-.2954E-09)	(-.6282E-11,-.1045E-08)
L=11 M=10	(.6603E-09,-.1288E-08)	(-.2571E-11,-.5179E-09)
L=11 M=11	(.2882E-09,-.2009E-09)	(-.5268E-09,-.8406E-10)
L=12 M= 0	(-.2333E-09, .0000E+00)	(-.2877E-09, .0000E+00)
L=12 M= 1	(-.1106E-08,-.8295E-09)	(-.3520E-09, .2602E-09)
L=12 M= 2	(.5137E-10,-.2445E-09)	(-.2569E-09, .4192E-10)
L=12 M= 3	(-.9840E-09,-.1470E-09)	(.7061E-10,-.1034E-08)
L=12 M= 4	(.9216E-09, .8713E-10)	(-.1878E-09, .2076E-10)
L=12 M= 5	(.8188E-09, .6581E-09)	(-.2553E-09, .4218E-09)
L=12 M= 6	(.2903E-09, .6145E-10)	(.1070E-08, .3155E-09)
L=12 M= 7	(.9583E-09, .1421E-08)	(-.2757E-09, .5631E-09)
L=12 M= 8	(-.6264E-09, .2221E-08)	(.3952E-09, .9155E-10)
L=12 M= 9	(.5184E-09, .5133E-09)	(-.1223E-09, .7297E-09)
L=12 M=10	(-.5619E-10, .1992E-08)	(-.1046E-10,-.4646E-09)
L=12 M=11	(-.9164E-09,-.5201E-09)	(-.2342E-09, .4705E-09)
L=12 M=12	(-.5543E-09, .3618E-09)	(-.3923E-09,-.1129E-10)
L=13 M= 0	(.8750E-09, .0000E+00)	(-.1510E-08, .0000E+00)
L=13 M= 1	(-.3133E-09,-.5776E-09)	(-.3461E-09, .9216E-10)
L=13 M= 2	(.8017E-09,-.1161E-08)	(-.4243E-09, .5475E-09)
L=13 M= 3	(.9236E-09,-.1026E-08)	(.9647E-10, .1621E-09)
L=13 M= 4	(-.1286E-09, .1786E-09)	(-.7247E-10,-.5263E-09)
L=13 M= 5	(-.4256E-09,-.6394E-09)	(-.7347E-09,-.2667E-10)
L=13 M= 6	(.6654E-10,-.5226E-09)	(-.7899E-09,-.7200E-09)
L=13 M= 7	(.3251E-09,-.1414E-08)	(.8195E-09,-.5430E-09)
L=13 M= 8	(.5088E-10, .3246E-10)	(-.9609E-10, .1154E-08)
L=13 M= 9	(-.5505E-09, .7924E-09)	(.7673E-09,-.1462E-09)
L=13 M=10	(.2126E-09, .3678E-10)	(.1012E-08, .3493E-09)
L=13 M=11	(.1508E-08, .9868E-09)	(-.1254E-09, .5120E-09)
L=13 M=12	(-.1229E-08, .9759E-09)	(.3310E-09, .3462E-09)
L=13 M=13	(.3344E-10, .6000E-09)	(.2366E-09,-.5297E-10)
L=14 M= 0	(-.6608E-09, .0000E+00)	(.1336E-08, .0000E+00)
L=14 M= 1	(-.8171E-10, .3605E-09)	(-.6667E-09, .2539E-09)
L=14 M= 2	(-.8854E-09, .7306E-09)	(.2724E-10,-.3609E-10)
L=14 M= 3	(.7692E-09,-.4594E-09)	(-.1900E-09, .4611E-09)
L=14 M= 4	(.6684E-09, .4169E-09)	(.1367E-08, .4780E-10)
L=14 M= 5	(.1090E-08, .6012E-09)	(.6925E-09, .4662E-09)
L=14 M= 6	(-.6316E-09, .3621E-09)	(-.7441E-09,-.4226E-09)
L=14 M= 7	(.9954E-09,-.9751E-09)	(-.1084E-08,-.4542E-09)
L=14 M= 8	(.6450E-09,-.6045E-09)	(-.5613E-09,-.2353E-09)
L=14 M= 9	(-.1499E-09,-.1560E-09)	(-.5230E-09, .5309E-09)
L=14 M=10	(-.1167E-08,-.1240E-08)	(-.1330E-10,-.2079E-09)
L=14 M=11	(-.5645E-09,-.3674E-09)	(.7682E-10,-.1053E-08)
L=14 M=12	(-.4688E-10,-.1425E-08)	(-.5143E-10, .5347E-09)
L=14 M=13	(.3420E-10, .5297E-09)	(.2177E-09,-.2760E-09)
L=14 M=14	(-.3185E-09,-.3359E-10)	(.3749E-09,-.2465E-09)
L=15 M= 0	(.5635E-09, .0000E+00)	(.1421E-08, .0000E+00)
L=15 M= 1	(-.2714E-09,-.1206E-09)	(.1296E-09,-.4357E-09)
L=15 M= 2	(-.4012E-09, .1138E-09)	(-.1405E-09,-.6132E-09)
L=15 M= 3	(-.9881E-09, .5633E-09)	(.5519E-09, .2516E-09)
L=15 M= 4	(-.5592E-09,-.4964E-09)	(-.7413E-09, .3261E-09)
L=15 M= 5	(.4754E-10, .3016E-09)	(.1078E-08,-.5655E-09)
L=15 M= 6	(.2146E-09, .5630E-09)	(.1144E-08, .4246E-09)
L=15 M= 7	(-.1417E-09, .1079E-08)	(-.1730E-09,-.1227E-08)
L=15 M= 8	(.9951E-09, .6090E-09)	(-.8192E-09,-.4332E-09)
L=15 M= 9	(.4535E-09, .1267E-08)	(-.2312E-09, .8338E-09)
L=15 M=10	(-.4365E-10,-.7223E-10)	(-.6225E-09,-.2364E-10)
L=15 M=11	(-.6480E-09,-.8166E-09)	(-.3433E-09, .1429E-09)
L=15 M=12	(.6976E-09, .2431E-09)	(-.2245E-09,-.5781E-09)
L=15 M=13	(-.8583E-09,-.9150E-09)	(.3443E-09, .4603E-09)
L=15 M=14	(.1332E-08,-.1209E-08)	(-.1814E-09,-.3770E-09)
L=15 M=15	(.3459E-09, .1042E-09)	(.4356E-09,-.1863E-09)
L=16 M= 0	(.1391E-08, .0000E+00)	(-.4412E-09, .0000E+00)
L=16 M= 1	(-.6473E-10, .1076E-08)	(.4560E-09, .1741E-09)
L=16 M= 2	(.8855E-10,-.1498E-09)	(-.7977E-09,-.2176E-09)
L=16 M= 3	(.7079E-11, .7084E-10)	(.2110E-09,-.1658E-09)
L=16 M= 4	(.8462E-09,-.3651E-09)	(-.1742E-09,-.1427E-10)
L=16 M= 5	(-.9232E-09,-.2533E-09)	(-.5381E-09,-.1691E-09)
L=16 M= 6	(.4690E-10,-.6978E-09)	(-.6981E-10, .5192E-09)
L=16 M= 7	(-.3880E-09, .4485E-10)	(.5482E-10,-.3588E-10)
L=16 M= 8	(-.2233E-09,-.3110E-09)	(.8721E-09,-.7883E-09)
L=16 M= 9	(.6073E-09, .1227E-08)	(-.8382E-09,-.5939E-09)
L=16 M=10	(-.3338E-10, .1245E-08)	(.2149E-09, .3592E-09)
L=16 M=11	(-.2858E-09, .2528E-09)	(-.2345E-09,-.3057E-09)
L=16 M=12	(-.4332E-10,-.2852E-10)	(.6558E-10, .1510E-09)
L=16 M=13	(.8687E-09, .2219E-09)	(-.2178E-10, .4174E-09)

TABLE C1. (continued)

	Surface Divergence	Radial Vorticity
L=16 M=14	(-.5939E-09, .1035E-08)	(.6820E-10, .6633E-10)
L=16 M=15	(-.2860E-09,-.1239E-08)	(-.2169E-09, .2113E-09)
L=16 M=16	(.3709E-09, .2609E-09)	(-.3110E-11, .3981E-09)
L=17 M= 0	(.4510E-09, .0000E+00)	(.8926E-10, .0000E+00)
L=17 M= 1	(.4489E-09, .3130E-10)	(.6782E-09, .3761E-10)
L=17 M= 2	(-.4576E-09, .6244E-09)	(-.1440E-09, .7760E-09)
L=17 M= 3	(-.1158E-08, .5412E-10)	(-.6758E-09,-.7097E-09)
L=17 M= 4	(-.4500E-10,-.2086E-09)	(.3962E-09,-.3262E-09)
L=17 M= 5	(.8295E-09,-.7639E-09)	(-.1695E-09, .3509E-09)
L=17 M= 6	(.8717E-09, .6208E-09)	(-.3446E-09,-.4705E-09)
L=17 M= 7	(-.1990E-09,-.1071E-08)	(.2019E-09, .6929E-09)
L=17 M= 8	(.3285E-09,-.2157E-09)	(-.8881E-09,-.3697E-09)
L=17 M= 9	(-.5019E-09,-.1074E-08)	(.1077E-08, .1224E-09)
L=17 M=10	(.4944E-09, .3876E-09)	(-.4336E-09,-.3870E-09)
L=17 M=11	(-.8288E-10,-.1796E-09)	(.7065E-09,-.3305E-09)
L=17 M=12	(.7736E-09, .2889E-09)	(-.1639E-09,-.9936E-10)
L=17 M=13	(-.4240E-09,-.4381E-09)	(.2178E-11, .1562E-11)
L=17 M=14	(.1262E-09,-.2407E-09)	(-.1476E-09, .9583E-10)
L=17 M=15	(.4471E-09, .1027E-08)	(-.3225E-09,-.8410E-10)
L=17 M=16	(-.6066E-09,-.1528E-09)	(-.1655E-09, .3656E-09)
L=17 M=17	(-.2989E-10, .1571E-09)	(-.2039E-09, .1800E-09)
L=18 M= 0	(-.2578E-09, .0000E+00)	(-.8902E-09, .0000E+00)
L=18 M= 1	(.4174E-09,-.6274E-09)	(-.1131E-09, .1660E-10)
L=18 M= 2	(-.1738E-09,-.6695E-10)	(-.1706E-09, .1522E-09)
L=18 M= 3	(.5384E-10,-.5262E-09)	(-.6050E-09, .8543E-09)
L=18 M= 4	(-.8448E-09,-.1300E-09)	(-.2180E-09, .4012E-10)
L=18 M= 5	(-.8720E-09,-.4950E-09)	(-.5701E-09, .1396E-09)
L=18 M= 6	(-.2385E-09,-.8338E-10)	(.3773E-09,-.2195E-09)
L=18 M= 7	(.9532E-09, .1738E-09)	(.3377E-10,-.1954E-09)
L=18 M= 8	(-.3429E-09,-.9720E-09)	(-.4110E-09,-.7495E-10)
L=18 M= 9	(.1142E-08,-.3784E-09)	(-.7895E-09,-.4393E-10)
L=18 M=10	(-.5670E-09, .4077E-09)	(.9388E-09, .6419E-09)
L=18 M=11	(-.2604E-09, .1787E-10)	(-.2418E-09,-.2110E-09)
L=18 M=12	(-.3407E-09,-.4166E-09)	(.6395E-09,-.8685E-09)
L=18 M=13	(.7086E-09, .2746E-09)	(-.2148E-09, .3623E-09)
L=18 M=14	(-.6167E-09, .4142E-10)	(-.1912E-10,-.4753E-10)
L=18 M=15	(-.1344E-10,-.4311E-10)	(.2865E-09,-.3244E-09)
L=18 M=16	(.2740E-09, .1718E-09)	(-.4911E-09,-.1490E-09)
L=18 M=17	(-.3354E-09,-.5951E-10)	(-.8025E-10,-.1225E-09)
L=18 M=18	(-.2493E-09,-.1037E-10)	(-.1226E-09,-.2117E-09)
L=19 M= 0	(-.5796E-09, .0000E+00)	(.1136E-08, .0000E+00)
L=19 M= 1	(.5141E-09,-.7836E-10)	(.1711E-09, .5630E-09)
L=19 M= 2	(-.3006E-10, .7218E-09)	(.2951E-09,-.2840E-09)
L=19 M= 3	(-.1127E-09, .4154E-09)	(-.3877E-09, .2529E-09)
L=19 M= 4	(.1461E-09,-.1736E-10)	(.2822E-09, .5270E-09)
L=19 M= 5	(.3962E-09, .4502E-09)	(.4250E-09, .4342E-09)
L=19 M= 6	(-.7836E-09,-.2610E-10)	(.1250E-09, .8466E-09)
L=19 M= 7	(.1604E-09, .2480E-09)	(.5166E-09,-.1288E-09)
L=19 M= 8	(-.8469E-11, .2733E-09)	(-.1120E-09,-.9567E-10)
L=19 M= 9	(-.2538E-10,-.1625E-09)	(-.4320E-09,-.9384E-09)
L=19 M=10	(.1086E-08,-.5357E-09)	(-.6619E-09, .6623E-09)
L=19 M=11	(-.6866E-09, .1200E-08)	(.3500E-09, .9258E-09)
L=19 M=12	(-.1270E-08,-.2409E-09)	(-.5097E-09,-.1451E-09)
L=19 M=13	(-.8472E-09,-.4152E-09)	(.1086E-09,-.3233E-09)
L=19 M=14	(.3902E-09,-.2022E-09)	(-.2990E-10, .2592E-09)
L=19 M=15	(-.9779E-10, .1454E-09)	(.1903E-09,-.2920E-09)
L=19 M=16	(.3718E-09,-.5166E-10)	(.4740E-09,-.1205E-09)
L=19 M=17	(.2895E-09, .3777E-09)	(-.5112E-10,-.3100E-10)
L=19 M=18	(.2101E-09, .3650E-09)	(.1904E-09,-.1926E-09)
L=19 M=19	(.8290E-10, .3305E-09)	(.6503E-10,-.5289E-11)
L=20 M= 0	(.4051E-09, .0000E+00)	(-.2626E-09, .0000E+00)
L=20 M= 1	(.8923E-10,-.3011E-09)	(.7789E-09,-.8121E-09)
L=20 M= 2	(.1058E-08,-.4791E-09)	(.9573E-09,-.1627E-09)
L=20 M= 3	(-.1319E-09, .1004E-08)	(.1240E-08,-.6879E-09)
L=20 M= 4	(-.4708E-09,-.5682E-10)	(-.8766E-09,-.3382E-09)
L=20 M= 5	(-.3615E-09, .3098E-09)	(.6971E-09,-.4403E-09)
L=20 M= 6	(.3570E-09,-.1046E-09)	(.4208E-09, .5501E-09)
L=20 M= 7	(-.1853E-09, .3867E-09)	(.7396E-09,-.4278E-10)
L=20 M= 8	(-.2922E-10, .8086E-10)	(.7670E-09, .9035E-10)
L=20 M= 9	(-.3486E-09, .9264E-09)	(-.2416E-09, .2462E-09)
L=20 M=10	(.8200E-09, .2728E-09)	(-.2900E-09,-.6844E-09)
L=20 M=11	(.6811E-09, .7696E-09)	(-.2743E-11, .1925E-09)
L=20 M=12	(.2798E-09, .2675E-10)	(-.2205E-09, .9048E-09)
L=20 M=13	(-.3120E-09, .2305E-09)	(-.1814E-09,-.3591E-09)

TABLE C1. (continued)

	Surface Divergence	Radial Vorticity
L=20 M=14	(-.1917E-09, .1515E-09)	(.5360E-10, .3454E-09)
L=20 M=15	(-.1932E-09,-.1438E-09)	(.1715E-10, .1791E-09)
L=20 M=16	(-.3305E-09,-.3142E-09)	(-.1197E-09,-.2010E-09)
L=20 M=17	(-.9765E-10,-.4863E-09)	(.7920E-10,-.2731E-10)
L=20 M=18	(.1023E-09, .6250E-10)	(.3777E-09,-.5019E-10)
L=20 M=19	(.2884E-09,-.3345E-09)	(.6242E-10,-.7418E-10)
L=20 M=20	(.1777E-10,-.7572E-10)	(.1835E-10, .3197E-10)
L=21 M= 0	(.1034E-10, .0000E+00)	(-.1724E-08, .0000E+00)
L=21 M= 1	(.2020E-09, .5850E-09)	(-.3763E-09, .1280E-09)
L=21 M= 2	(.6954E-09,-.4090E-09)	(-.3041E-09,-.9667E-10)
L=21 M= 3	(.9614E-09,-.4432E-10)	(.2745E-09,-.1363E-09)
L=21 M= 4	(.6025E-09, .3297E-09)	(.1290E-09,-.8837E-09)
L=21 M= 5	(-.5547E-09,-.5119E-09)	(-.8196E-09,-.2687E-09)
L=21 M= 6	(.2694E-10,-.7996E-10)	(-.6016E-09,-.3023E-09)
L=21 M= 7	(-.1534E-09,-.9156E-09)	(-.2969E-09, .2642E-09)
L=21 M= 8	(.3457E-09,-.4693E-09)	(.5387E-09,-.1493E-09)
L=21 M= 9	(-.3059E-09,-.4042E-09)	(.3629E-09,-.1522E-09)
L=21 M=10	(-.3924E-09, .3623E-09)	(-.3083E-10,-.3767E-09)
L=21 M=11	(.2652E-09, .2549E-09)	(.2076E-09,-.1997E-09)
L=21 M=12	(.9311E-10, .1068E-08)	(-.2229E-10,-.6661E-09)
L=21 M=13	(-.1919E-10,-.9121E-09)	(-.2379E-09, .2434E-10)
L=21 M=14	(.8635E-09, .9442E-11)	(.2161E-09,-.1640E-09)
L=21 M=15	(.7415E-09, .1453E-09)	(.1028E-09, .4648E-09)
L=21 M=16	(.9176E-10, .8856E-09)	(.1302E-09, .1306E-09)
L=21 M=17	(.2356E-10,-.4729E-10)	(-.3150E-09, .5018E-09)
L=21 M=18	(-.3420E-09, .5214E-10)	(-.3598E-10,-.4462E-10)
L=21 M=19	(-.3003E-09, .1513E-10)	(.1258E-09, .7750E-10)
L=21 M=20	(.2381E-10,-.4540E-09)	(-.1258E-09, .8914E-10)
L=21 M=21	(-.7324E-10,-.7609E-10)	(.2928E-10,-.9607E-10)
L=22 M= 0	(-.9256E-09, .0000E+00)	(.6713E-09, .0000E+00)
L=22 M= 1	(-.2154E-09,-.5481E-09)	(-.3161E-09, .2684E-09)
L=22 M= 2	(-.2018E-09, .6084E-09)	(-.3927E-09, .1851E-09)
L=22 M= 3	(-.4362E-09, .6266E-10)	(-.3464E-09, .2573E-09)
L=22 M= 4	(-.7640E-10, .8639E-09)	(.7642E-10, .5392E-09)
L=22 M= 5	(-.5399E-10,-.5777E-12)	(-.4535E-09, .2175E-09)
L=22 M= 6	(.2534E-09, .7255E-09)	(-.8523E-10,-.4982E-09)
L=22 M= 7	(-.1846E-09,-.1310E-09)	(-.6934E-09, .5005E-09)
L=22 M= 8	(-.2506E-09, .1072E-09)	(-.5557E-09,-.1269E-09)
L=22 M= 9	(.6225E-09,-.9797E-09)	(-.1732E-09, .2176E-09)
L=22 M=10	(-.3921E-09,-.9921E-09)	(.2204E-09,-.7783E-10)
L=22 M=11	(.2687E-09,-.7580E-09)	(.3942E-10,-.5356E-09)
L=22 M=12	(-.1089E-09, .3523E-09)	(.5056E-09,-.1528E-09)
L=22 M=13	(-.5687E-10, .3998E-09)	(-.2504E-09,-.8475E-09)
L=22 M=14	(-.5268E-09,-.3750E-09)	(-.2160E-09,-.2092E-09)
L=22 M=15	(.1397E-10,-.5186E-09)	(-.3886E-10,-.1368E-09)
L=22 M=16	(.1015E-09,-.5809E-09)	(-.4837E-10,-.1669E-09)
L=22 M=17	(.3985E-09, .5687E-09)	(.5410E-10,-.2129E-09)
L=22 M=18	(-.8589E-10,-.2248E-09)	(-.2777E-09, .5531E-09)
L=22 M=19	(.1459E-09, .1713E-09)	(.9001E-10,-.1979E-10)
L=22 M=20	(-.3777E-09, .3289E-09)	(-.3415E-10, .1818E-09)
L=22 M=21	(-.1730E-09,-.2430E-09)	(-.1334E-09, .1014E-09)
L=22 M=22	(.3487E-10,-.7233E-11)	(.4230E-10,-.1019E-09)
L=23 M= 0	(-.1041E-09, .0000E+00)	(-.3667E-09, .0000E+00)
L=23 M= 1	(-.5585E-09,-.4595E-09)	(-.4111E-10,-.8985E-10)
L=23 M= 2	(-.1867E-09,-.9640E-09)	(-.8626E-10,-.3854E-09)
L=23 M= 3	(.2077E-10,-.3353E-09)	(.3159E-09, .3965E-09)
L=23 M= 4	(-.2552E-09,-.5811E-09)	(-.2149E-09, .6434E-09)
L=23 M= 5	(-.9798E-09, .4405E-09)	(.8895E-10, .1865E-09)
L=23 M= 6	(-.1155E-08,-.1846E-09)	(.4444E-09, .6875E-09)
L=23 M= 7	(.4752E-10, .5354E-09)	(.2127E-09, .1702E-09)
L=23 M= 8	(-.5533E-09, .4961E-09)	(.3989E-09, .4886E-09)
L=23 M= 9	(.2860E-09, .2272E-09)	(.1418E-09,-.7631E-10)
L=23 M=10	(-.1411E-09, .1706E-09)	(-.4917E-09,-.2335E-10)
L=23 M=11	(.3098E-09,-.5756E-09)	(-.2593E-09, .2891E-09)
L=23 M=12	(.1314E-09, .2007E-10)	(.4214E-09,-.1953E-09)
L=23 M=13	(-.4611E-09,-.3379E-11)	(.3556E-09, .2223E-09)
L=23 M=14	(.3039E-09,-.1017E-09)	(-.3020E-09,-.6962E-09)
L=23 M=15	(.9509E-10, .1073E-09)	(.5979E-10, .2963E-09)
L=23 M=16	(-.1996E-09, .4956E-10)	(-.4980E-09,-.1594E-10)
L=23 M=17	(-.2670E-09,-.6056E-09)	(.1101E-09,-.3941E-09)
L=23 M=18	(.5442E-09,-.4023E-10)	(-.2966E-09,-.1316E-09)
L=23 M=19	(-.4306E-09,-.2073E-09)	(-.2498E-10,-.1646E-09)
L=23 M=20	(.4852E-09,-.3720E-09)	(-.9604E-11, .4148E-10)
L=23 M=21	(.5548E-10, .6016E-09)	(-.4981E-10, .4891E-10)
L=23 M=22	(-.1776E-09, .2234E-10)	(-.1237E-10, .1526E-10)
L=23 M=23	(.7839E-10, .1453E-09)	(.4364E-10, .3964E-10)

TABLE C1. (continued)

	Surface Divergence	Radial Vorticity
L=24 M= 0	(.1550E-09, .0000E+00)	(.8407E-09, .0000E+00)
L=24 M= 1	(-.8023E-10, .9926E-09)	(-.7470E-09, .8882E-09)
L=24 M= 2	(-.3363E-09,-.2298E-10)	(.4981E-09,-.8589E-10)
L=24 M= 3	(.5730E-09,-.2718E-10)	(-.1996E-09,-.9706E-10)
L=24 M= 4	(.7622E-09,-.2742E-09)	(.4200E-09,-.4951E-09)
L=24 M= 5	(.1067E-08,-.4160E-09)	(.8237E-10,-.2838E-09)
L=24 M= 6	(.2465E-09,-.5746E-09)	(-.3890E-09, .3407E-09)
L=24 M= 7	(-.6863E-09,-.2379E-09)	(.3807E-09,-.1261E-09)
L=24 M= 8	(-.1070E-09,-.2824E-09)	(.1181E-09, .4476E-09)
L=24 M= 9	(-.4738E-09, .1349E-09)	(.1069E-08,-.3520E-09)
L=24 M=10	(.3909E-09,-.3978E-09)	(-.4144E-11, .1384E-09)
L=24 M=11	(-.4602E-09, .8986E-09)	(-.2603E-09,-.1066E-09)
L=24 M=12	(.7855E-09,-.1133E-09)	(.1029E-09, .8313E-09)
L=24 M=13	(-.2369E-10, .1287E-08)	(.1308E-09, .2106E-09)
L=24 M=14	(-.1121E-08,-.3215E-10)	(-.6743E-10, .1248E-09)
L=24 M=15	(.7592E-10, .4557E-10)	(-.1205E-09,-.3815E-09)
L=24 M=16	(.3476E-09, .3791E-09)	(.4649E-09, .4436E-09)
L=24 M=17	(.1169E-09, .4451E-09)	(-.3191E-09, .1145E-10)
L=24 M=18	(-.2204E-09, .1087E-10)	(.2950E-09,-.2291E-09)
L=24 M=19	(.1914E-09, .7486E-11)	(-.9827E-10, .1778E-09)
L=24 M=20	(-.1712E-09, .6714E-10)	(-.4456E-10,-.3807E-09)
L=24 M=21	(.1225E-09,-.5673E-09)	(-.1795E-10,-.4216E-10)
L=24 M=22	(.2738E-09, .9277E-10)	(-.3138E-10,-.7948E-10)
L=24 M=23	(.1117E-09,-.3029E-10)	(.6301E-10,-.5694E-10)
L=24 M=24	(.1665E-09,-.1902E-10)	(.4228E-10, .5277E-10)
L=25 M= 0	(.6643E-09, .0000E+00)	(.7459E-09, .0000E+00)
L=25 M= 1	(-.2171E-09,-.6395E-10)	(.2616E-09,-.9757E-09)
L=25 M= 2	(-.3490E-10, .3933E-09)	(-.2757E-09, .4277E-09)
L=25 M= 3	(-.1994E-09, .1081E-09)	(.7847E-09,-.4929E-09)
L=25 M= 4	(.5092E-09, .5519E-09)	(.3451E-09,-.1518E-09)
L=25 M= 5	(.2737E-09, .7896E-09)	(.3376E-09,-.8348E-09)
L=25 M= 6	(.9028E-09, .1678E-09)	(-.7144E-09,-.8837E-09)
L=25 M= 7	(.3388E-09, .2133E-09)	(-.2886E-09,-.2984E-09)
L=25 M= 8	(.1911E-09,-.1177E-10)	(-.3468E-09, .3618E-09)
L=25 M= 9	(-.3572E-09,-.2431E-09)	(-.1840E-09, .5052E-09)
L=25 M=10	(.1733E-09,-.2385E-09)	(.6637E-09,-.4187E-09)
L=25 M=11	(-.1168E-09,-.1924E-09)	(.5009E-09, .2315E-09)
L=25 M=12	(.5042E-09, .1908E-09)	(-.1595E-09,-.8233E-09)
L=25 M=13	(.3675E-09,-.2086E-09)	(.7052E-09, .4339E-09)
L=25 M=14	(-.4359E-10, .7051E-09)	(-.1786E-09, .2306E-09)
L=25 M=15	(-.9349E-09,-.5102E-09)	(-.1671E-09, .1267E-09)
L=25 M=16	(.1500E-09, .4438E-10)	(.2648E-09,-.5005E-10)
L=25 M=17	(-.1420E-09, .1921E-09)	(.2506E-09, .2107E-09)
L=25 M=18	(-.6833E-10, .8394E-10)	(-.1072E-09,-.1398E-10)
L=25 M=19	(-.3764E-10, .3713E-09)	(.1247E-09,-.4342E-10)
L=25 M=20	(-.2266E-09, .3855E-09)	(.2869E-09, .2054E-09)
L=25 M=21	(.1249E-09, .2425E-09)	(-.1839E-09,-.1268E-09)
L=25 M=22	(-.1110E-09,-.5422E-10)	(.1241E-09,-.4982E-10)
L=25 M=23	(-.8042E-10,-.7009E-11)	(-.2376E-10, .2863E-11)
L=25 M=24	(.5906E-10, .2723E-10)	(-.6244E-10,-.7651E-11)
L=25 M=25	(-.5957E-10, .1488E-10)	(.7644E-11, .4399E-10)
L=26 M= 0	(.3886E-09, .0000E+00)	(-.1830E-08, .0000E+00)
L=26 M= 1	(-.1372E-09,-.1535E-09)	(.5913E-09, .1267E-09)
L=26 M= 2	(.1272E-11,-.2080E-09)	(-.1313E-08,-.5119E-13)
L=26 M= 3	(-.4192E-09,-.7552E-09)	(-.2430E-09, .4968E-10)
L=26 M= 4	(.5666E-10,-.5657E-09)	(.2425E-09,-.1376E-09)
L=26 M= 5	(-.5020E-10,-.1433E-09)	(.1187E-08, .4555E-09)
L=26 M= 6	(-.3190E-09, .5440E-09)	(.3830E-10,-.6623E-09)
L=26 M= 7	(-.3664E-09, .2764E-09)	(-.5924E-09,-.1901E-09)
L=26 M= 8	(.1825E-09, .3482E-09)	(-.8457E-10, .3708E-10)
L=26 M= 9	(.2228E-09, .2860E-09)	(-.6224E-09, .3067E-09)
L=26 M=10	(-.7586E-09,-.1117E-09)	(.3450E-09, .2165E-09)
L=26 M=11	(.1359E-11,-.3054E-09)	(-.3975E-09, .3084E-09)
L=26 M=12	(-.5747E-09, .1396E-09)	(.5824E-09, .4444E-10)
L=26 M=13	(.3458E-09,-.2577E-09)	(-.1113E-09,-.1039E-08)
L=26 M=14	(.2058E-09, .1010E-09)	(.3465E-09,-.1875E-09)
L=26 M=15	(.1677E-09,-.2031E-09)	(-.1878E-09,-.1093E-09)
L=26 M=16	(-.5734E-10,-.5689E-09)	(.2424E-09,-.1191E-09)
L=26 M=17	(.3495E-09,-.1191E-09)	(.3359E-09, .2827E-10)
L=26 M=18	(-.3157E-09, .7438E-10)	(-.6823E-10, .4041E-10)
L=26 M=19	(-.9329E-10,-.1581E-09)	(-.1176E-10, .2900E-11)
L=26 M=20	(.1378E-10,-.1374E-09)	(.9662E-10, .5180E-10)
L=26 M=21	(-.2153E-09, .1848E-09)	(.1766E-09,-.5536E-10)
L=26 M=22	(.5065E-10,-.3297E-11)	(-.1354E-09, .4748E-11)
L=26 M=23	(-.8488E-12, .7386E-10)	(.1243E-09, .8562E-11)

TABLE C1. (continued)

	Surface Divergence	Radial Vorticity
L=26 M=24	(-.1312E-09, .4082E-10)	(-.1818E-10, .4335E-10)
L=26 M=25	(.1336E-10,-.9169E-10)	(-.4899E-10,-.3612E-10)
L=26 M=26	(-.7299E-10, .8401E-10)	(-.2705E-10, .8362E-11)
L=27 M= 0	(-.6355E-10, .0000E+00)	(.9851E-09, .0000E+00)
L=27 M= 1	(.2473E-09,-.5393E-10)	(-.5149E-09, .7912E-09)
L=27 M= 2	(-.4513E-09, .5639E-09)	(.6752E-09, .6399E-10)
L=27 M= 3	(-.3509E-09,-.6987E-10)	(-.9197E-09, .7494E-09)
L=27 M= 4	(-.4470E-09,-.2883E-11)	(-.5908E-09, .2617E-10)
L=27 M= 5	(.3425E-09,-.7098E-09)	(-.6271E-09, .7442E-09)
L=27 M= 6	(.2747E-09,-.2740E-09)	(.1031E-08,-.1104E-09)
L=27 M= 7	(-.7721E-10,-.1640E-09)	(-.5892E-10, .1677E-09)
L=27 M= 8	(-.5353E-09, .7660E-09)	(-.4292E-09,-.5149E-09)
L=27 M= 9	(.6512E-10,-.2488E-10)	(.5028E-10, .2978E-10)
L=27 M=10	(.1845E-09,-.6185E-10)	(-.6560E-09, .5302E-09)
L=27 M=11	(-.5689E-10,-.1241E-09)	(.1891E-09,-.5286E-09)
L=27 M=12	(-.3281E-09,-.3645E-09)	(-.4594E-09, .8630E-09)
L=27 M=13	(-.3501E-09, .9631E-10)	(.1536E-09,-.4311E-10)
L=27 M=14	(-.3526E-09, .1366E-09)	(.1755E-09,-.4411E-09)
L=27 M=15	(-.2276E-09, .2907E-09)	(-.1324E-09,-.3795E-09)
L=27 M=16	(-.1547E-09,-.4639E-09)	(-.3796E-09,-.7314E-10)
L=27 M=17	(.3461E-09,-.2885E-09)	(.1427E-09,-.1482E-09)
L=27 M=18	(.9928E-10, .5718E-10)	(.1659E-09,-.1339E-09)
L=27 M=19	(.1245E-09,-.6625E-11)	(-.8321E-10, .5978E-11)
L=27 M=20	(.3428E-10, .2935E-11)	(.8662E-11,-.8441E-10)
L=27 M=21	(.2647E-11,-.2794E-09)	(.8262E-10, .9570E-10)
L=27 M=22	(.4932E-10, .1598E-09)	(.1192E-10,-.6612E-10)
L=27 M=23	(-.8113E-10, .1737E-10)	(.8100E-11, .8213E-10)
L=27 M=24	(.1194E-10,-.5946E-11)	(.1135E-10, .2466E-11)
L=27 M=25	(-.7567E-10, .2910E-11)	(-.1033E-10,-.1547E-10)
L=27 M=26	(-.3085E-10,-.8517E-10)	(.3349E-10,-.4288E-10)
L=27 M=27	(-.1826E-10, .1847E-10)	(-.2320E-10,-.1231E-10)
L=28 M= 0	(.5120E-09, .0000E+00)	(.5989E-09, .0000E+00)
L=28 M= 1	(.4320E-09, .1136E-09)	(.1493E-09,-.8795E-09)
L=28 M= 2	(.3788E-09,-.2375E-09)	(.3881E-09, .4842E-10)
L=28 M= 3	(-.9421E-10, .3881E-09)	(.1384E-09,-.2981E-09)
L=28 M= 4	(-.4089E-09,-.2692E-09)	(-.1282E-09, .6729E-09)
L=28 M= 5	(-.6964E-10, .6503E-09)	(-.4103E-09,-.1394E-09)
L=28 M= 6	(-.3326E-10,-.1637E-09)	(-.2343E-09, .1181E-08)
L=28 M= 7	(.2805E-09,-.2611E-09)	(.2763E-09,-.8888E-10)
L=28 M= 8	(.2115E-10, .5281E-11)	(.2735E-09, .1887E-09)
L=28 M= 9	(-.1898E-09, .5440E-09)	(.1964E-09,-.4285E-09)
L=28 M=10	(-.5578E-09, .2872E-09)	(-.4219E-09,-.1679E-09)
L=28 M=11	(.2586E-09, .1174E-09)	(-.1350E-09, .5345E-10)
L=28 M=12	(.2784E-09,-.3709E-09)	(.4744E-10,-.6779E-10)
L=28 M=13	(.1666E-09,-.1343E-09)	(-.7400E-10, .6450E-09)
L=28 M=14	(.1766E-09,-.8976E-10)	(.2643E-09, .2534E-09)
L=28 M=15	(-.1005E-09, .6153E-09)	(.1935E-09, .2146E-09)
L=28 M=16	(-.5765E-09, .3451E-09)	(-.1567E-09, .1239E-09)
L=28 M=17	(-.1853E-09,-.1688E-10)	(-.1802E-09, .2393E-09)
L=28 M=18	(.5447E-10, .7515E-11)	(.6008E-11, .7201E-10)
L=28 M=19	(-.1606E-09, .8675E-10)	(-.7905E-11,-.1248E-09)
L=28 M=20	(-.3718E-10,-.1823E-09)	(-.8186E-10, .2640E-10)
L=28 M=21	(-.6669E-10, .1397E-10)	(-.9801E-10,-.9086E-10)
L=28 M=22	(-.7415E-10,-.3152E-09)	(.2743E-10, .1404E-10)
L=28 M=23	(.1606E-09,-.6135E-10)	(-.1372E-10, .3523E-10)
L=28 M=24	(-.3089E-10, .4928E-12)	(.7772E-10, .1440E-10)
L=28 M=25	(.1037E-09,-.6554E-10)	(-.2824E-10, .3220E-10)
L=28 M=26	(-.9892E-11, .4093E-10)	(.3867E-10,-.2253E-10)
L=28 M=27	(.1791E-10,-.3240E-11)	(.3297E-10, .1560E-10)
L=28 M=28	(.1966E-10,-.1878E-10)	(.4317E-11,-.1041E-10)
L=29 M= 0	(-.3137E-09, .0000E+00)	(-.4485E-09, .0000E+00)
L=29 M= 1	(.3440E-09, .4568E-09)	(.1009E-08, .4573E-09)
L=29 M= 2	(.4791E-10, .3970E-09)	(-.2856E-09,-.1928E-09)
L=29 M= 3	(.3671E-10, .2963E-09)	(.1988E-09,-.5972E-09)
L=29 M= 4	(-.2159E-09,-.1090E-09)	(-.1574E-09,-.5458E-09)
L=29 M= 5	(.4178E-10,-.5149E-09)	(.1125E-08, .3624E-10)
L=29 M= 6	(.1154E-08,-.2926E-09)	(.2536E-10,-.2081E-09)
L=29 M= 7	(-.5296E-11,-.1641E-10)	(.3882E-09,-.3056E-09)
L=29 M= 8	(.1407E-09,-.5540E-09)	(-.5481E-10, .1894E-09)
L=29 M= 9	(.1786E-10,-.3046E-09)	(.1919E-09, .2464E-09)
L=29 M=10	(-.1184E-09, .1023E-09)	(.4480E-09,-.9394E-10)
L=29 M=11	(-.6494E-09,-.1144E-09)	(.2303E-09, .3223E-09)
L=29 M=12	(.1937E-09,-.2389E-10)	(-.1380E-09,-.4938E-09)
L=29 M=13	(.2901E-09,-.1561E-10)	(.1210E-09, .1859E-09)
L=29 M=14	(.5623E-09, .1115E-09)	(.2595E-09,-.7498E-10)

TABLE C1. (continued)

	Surface Divergence	Radial Vorticity
L=29 M=15	(.6485E-10,-.2657E-09)	(.1895E-09, .4685E-09)
L=29 M=16	(-.3297E-10, .2179E-09)	(.2364E-09, .1184E-09)
L=29 M=17	(-.1189E-09,-.4118E-10)	(.1290E-09, .2428E-09)
L=29 M=18	(.1460E-09, .1827E-09)	(.2285E-09, .2518E-09)
L=29 M=19	(-.1245E-10, .2439E-10)	(-.8890E-10, .1486E-09)
L=29 M=20	(.8773E-11, .1261E-09)	(-.3044E-10, .3390E-10)
L=29 M=21	(-.7396E-10, .9710E-10)	(.4596E-10, .1473E-09)
L=29 M=22	(-.2910E-10, .9936E-10)	(-.1363E-09,-.4625E-10)
L=29 M=23	(-.1058E-09,-.1910E-09)	(-.7623E-10, .1490E-10)
L=29 M=24	(-.5465E-10,-.9075E-10)	(-.3439E-10, .3885E-10)
L=29 M=25	(-.9399E-10,-.1047E-10)	(.4707E-11,-.2216E-10)
L=29 M=26	(.8016E-10,-.7929E-10)	(-.2185E-10, .3776E-10)
L=29 M=27	(.4126E-11, .6040E-10)	(.2486E-10, .4347E-11)
L=29 M=28	(-.5563E-11, .7987E-11)	(-.4640E-11, .2362E-10)
L=29 M=29	(-.1064E-10,-.1228E-10)	(.9036E-12,-.4668E-12)
L=30 M= 0	(.9744E-11, .0000E+00)	(-.7227E-09, .0000E+00)
L=30 M= 1	(.4217E-10,-.8027E-09)	(.2981E-09, .5995E-09)
L=30 M= 2	(.5427E-10, .2998E-10)	(.5043E-09, .3473E-10)
L=30 M= 3	(-.6575E-09,-.1540E-10)	(.2558E-10, .3206E-09)
L=30 M= 4	(-.4758E-09, .2033E-09)	(-.4401E-09,-.2257E-09)
L=30 M= 5	(-.9289E-09, .7525E-10)	(-.6510E-09,-.1158E-09)
L=30 M= 6	(-.8941E-10,-.8098E-12)	(.8540E-09,-.7559E-09)
L=30 M= 7	(.4812E-09,-.3712E-09)	(-.5081E-10,-.6506E-09)
L=30 M= 8	(.6995E-09, .3933E-09)	(-.3484E-09,-.9967E-09)
L=30 M= 9	(.1652E-09,-.2485E-09)	(-.5689E-09,-.5211E-10)
L=30 M=10	(.4472E-09,-.8019E-10)	(.8030E-10, .1721E-09)
L=30 M=11	(.1552E-09,-.1220E-09)	(.2115E-09,-.8102E-10)
L=30 M=12	(-.8714E-10,-.2194E-09)	(.4040E-09,-.7808E-10)
L=30 M=13	(-.2750E-09,-.1583E-09)	(-.2371E-09,-.3141E-09)
L=30 M=14	(.2336E-09, .1230E-09)	(.1134E-09,-.9486E-11)
L=30 M=15	(.2868E-09,-.9315E-11)	(-.1860E-10,-.4114E-09)
L=30 M=16	(-.2806E-09,-.7328E-10)	(-.3170E-09, .2392E-09)
L=30 M=17	(-.3604E-09,-.5249E-09)	(.1223E-09,-.1094E-09)
L=30 M=18	(.3265E-09,-.3298E-09)	(.3190E-09, .6772E-10)
L=30 M=19	(.7770E-10, .3170E-09)	(.1553E-09, .1046E-10)
L=30 M=20	(-.2200E-09,-.9915E-10)	(-.1345E-10, .8138E-10)
L=30 M=21	(.1035E-09, .8217E-11)	(.1154E-09, .2460E-10)
L=30 M=22	(.8402E-10, .1073E-09)	(.1516E-09, .9063E-10)
L=30 M=23	(.1193E-09, .1193E-09)	(-.2762E-11, .5590E-11)
L=30 M=24	(.9933E-10,-.1401E-11)	(-.2324E-10, .6307E-10)
L=30 M=25	(-.2343E-10, .3864E-10)	(.2227E-10, .3523E-10)
L=30 M=26	(-.5373E-10, .4166E-10)	(-.5200E-10,-.2343E-10)
L=30 M=27	(.7943E-11,-.6027E-10)	(-.4255E-11, .5996E-11)
L=30 M=28	(.2411E-10, .2030E-10)	(-.9260E-11, .1187E-10)
L=30 M=29	(.1684E-10, .3928E-11)	(-.4785E-11, .3973E-11)
L=30 M=30	(-.1472E-11, .1503E-11)	(.1527E-11,-.1821E-12)
L=31 M= 0	(.2419E-09, .0000E+00)	(-.5245E-09, .0000E+00)
L=31 M= 1	(.3491E-09, .1302E-09)	(-.5704E-09,-.1701E-09)
L=31 M= 2	(.7663E-09,-.3476E-09)	(-.2659E-09, .3389E-09)
L=31 M= 3	(.5635E-09,-.1741E-09)	(.2176E-09,-.1379E-09)
L=31 M= 4	(-.1314E-09,-.3847E-09)	(.5869E-10, .7057E-09)
L=31 M= 5	(-.4477E-09,-.3018E-09)	(-.7964E-09, .2764E-09)
L=31 M= 6	(-.6725E-09,-.1762E-11)	(-.3027E-09, .6748E-09)
L=31 M= 7	(-.8715E-09,-.2868E-10)	(.3803E-09, .7237E-09)
L=31 M= 8	(-.4347E-09, .2753E-09)	(-.2730E-09,-.4493E-09)
L=31 M= 9	(-.1666E-09, .4836E-09)	(.2844E-09,-.5679E-09)
L=31 M=10	(-.1141E-10, .7121E-09)	(-.7256E-09, .7725E-10)
L=31 M=11	(-.2570E-09, .1038E-09)	(-.1514E-09,-.1437E-09)
L=31 M=12	(.7243E-10, .1121E-09)	(-.3362E-10, .3847E-09)
L=31 M=13	(-.3288E-09, .2497E-09)	(.5730E-09, .2788E-10)
L=31 M=14	(-.8701E-10, .1880E-09)	(-.3281E-09,-.4451E-10)
L=31 M=15	(-.1731E-09, .2226E-09)	(.3955E-09,-.5385E-09)
L=31 M=16	(.5253E-10, .1420E-09)	(-.1956E-09,-.3475E-10)
L=31 M=17	(-.1647E-09, .2058E-10)	(-.4484E-09, .7960E-10)
L=31 M=18	(-.3334E-09,-.6284E-09)	(-.1656E-10,-.2265E-09)
L=31 M=19	(.2783E-09,-.5104E-09)	(.2483E-09, .1708E-10)
L=31 M=20	(.5769E-10, .1272E-09)	(-.1745E-09,-.1460E-09)
L=31 M=21	(-.1699E-09,-.1918E-09)	(.7745E-11,-.1417E-10)
L=31 M=22	(-.3581E-11,-.1156E-09)	(.5645E-10,-.2669E-10)
L=31 M=23	(-.1122E-09,-.5218E-10)	(.5943E-10,-.5347E-10)
L=31 M=24	(.7090E-10, .3423E-10)	(-.2655E-11, .1115E-10)
L=31 M=25	(.7926E-10, .3990E-10)	(.3878E-10,-.1031E-10)
L=31 M=26	(.3047E-10, .1970E-10)	(.3059E-10, .1762E-10)
L=31 M=27	(.2193E-10, .6117E-10)	(-.2107E-10,-.2481E-10)
L=31 M=28	(-.3519E-10,-.7774E-11)	(.3844E-11,-.8960E-12)

TABLE C1. (continued)

	Surface Divergence	Radial Vorticity
L=31 M=29	(-.1019E-11,-.7595E-11)	(-.1393E-10,-.4237E-11)
L=31 M=30	(.3384E-11,-.4904E-11)	(-.1016E-11,-.2693E-11)
L=31 M=31	(.9359E-12,-.3236E-12)	(.5748E-12, .1434E-13)
L=32 M= 0	(-.2473E-09, .0000E+00)	(.6161E-09, .0000E+00)
L=32 M= 1	(-.7069E-10, .1815E-09)	(-.7216E-10, .1657E-09)
L=32 M= 2	(-.1499E-09, .2250E-09)	(-.1936E-09,-.1975E-09)
L=32 M= 3	(.5436E-09, .1597E-09)	(.2032E-09, .1086E-09)
L=32 M= 4	(.4962E-09, .2822E-09)	(.1603E-09,-.2099E-09)
L=32 M= 5	(.4233E-09,-.4975E-10)	(.4440E-09, .1517E-09)
L=32 M= 6	(.7024E-10,-.3631E-09)	(-.3367E-09, .2406E-09)
L=32 M= 7	(.2479E-09,-.1373E-09)	(.2849E-09, .5508E-09)
L=32 M= 8	(-.3020E-09,-.1406E-10)	(-.3952E-10, .2054E-09)
L=32 M= 9	(-.2361E-09,-.3083E-09)	(.2342E-09,-.5104E-10)
L=32 M=10	(.9529E-10, .1139E-09)	(.1751E-09,-.8296E-10)
L=32 M=11	(-.7408E-10, .3706E-09)	(-.1693E-09,-.1356E-09)
L=32 M=12	(-.6044E-09,-.2825E-09)	(-.6607E-10,-.1739E-09)
L=32 M=13	(.6229E-10, .7000E-10)	(-.3049E-09, .2705E-09)
L=32 M=14	(-.5154E-09,-.2416E-09)	(.2972E-09, .4015E-10)
L=32 M=15	(-.1488E-09,-.4769E-10)	(-.8687E-10, .1532E-10)
L=32 M=16	(-.5305E-10, .2334E-09)	(.1286E-09,-.3012E-09)
L=32 M=17	(.3431E-10, .3972E-09)	(.9856E-10, .2431E-09)
L=32 M=18	(-.1128E-09, .5292E-10)	(-.1548E-09, .2556E-09)
L=32 M=19	(-.2907E-10, .9345E-10)	(-.1450E-09,-.1280E-09)
L=32 M=20	(-.7735E-10,-.1716E-09)	(.1962E-09,-.5934E-10)
L=32 M=21	(.9300E-10,-.5624E-10)	(-.6405E-10,-.3747E-11)
L=32 M=22	(.3739E-10,-.1918E-09)	(.2071E-10, .3110E-10)
L=32 M=23	(.2746E-10,-.6977E-10)	(-.3063E-10, .5456E-11)
L=32 M=24	(-.1070E-09,-.9035E-10)	(-.1411E-10,-.6839E-10)
L=32 M=25	(-.1003E-10,-.4237E-10)	(-.1030E-10,-.2716E-10)
L=32 M=26	(.2669E-10,-.2101E-10)	(-.5058E-12,-.2461E-10)
L=32 M=27	(.1896E-10,-.3676E-10)	(.1670E-10,-.1576E-10)
L=32 M=28	(.4466E-10, .9497E-11)	(.1232E-11, .1115E-11)
L=32 M=29	(-.5290E-11, .1824E-10)	(-.2444E-11,-.3576E-11)
L=32 M=30	(-.4862E-11,-.4589E-11)	(-.7376E-13,-.4037E-11)
L=32 M=31	(-.8863E-12, .9764E-12)	(-.2899E-12,-.1630E-12)
L=32 M=32	(.2784E-29, .5204E-23)	(-.1895E-29, .7880E-23)

Read $-.1277E-08$ as $-.1277 \times 10^{-8}$.

REFERENCES

Anderson, D. L., and A. M. Dziewonski, Seismic tomography, *Sci. Am.*, *251*, 60–68, 1984.

Anderson, O. L., E. Schreiber, R. C. Lieberman, and N. Soga, Some elastic constant data on minerals relevant to geophysics, *Rev. Geophys.*, *6*, 491–524, 1968.

Backus, G., A class of self-sustaining dissipative spherical dynamos, *Ann. Phys.*, *4*, 372–447, 1958.

Baumgardner, J. R., 3-D numerical investigation of mantle convection (abstract), *Eos Trans. AGU*, *65*, 236, 1984.

Chandrasekhar, S. *Hydrodynamic and Hydromagnetic Stability*, Oxford University Press, New York, 1961.

Dziewonski, A. M., Mapping the lower mantle: Determination of lateral heterogeneity in *P* velocity up to degree and order 6, *J. Geophys. Res.*, *89*, 5929–5952, 1984.

Forte, A. M., and W. R. Peltier, Surface plate kinematics and mantle convection, in *The Composition, Structure, and Dynamics of the Lithosphere-Asthenosphere System, Geodyn. Ser.*, edited by K. Fuchs and C. Froidevaux, pp. 125–136, AGU, Washington, D. C., in press, 1987.

Hager, B. H., Subducted slabs and the geoid: Constraints on mantle rheology and flow, *J. Geophys. Res.*, *89*, 6003–6015, 1984.

Hager, B. H., and R. J. O'Connell, Subduction zone dips and flow driven by the plates, *Tectonophysics*, *50*, 111–134, 1978.

Hager, B. H., and R. J. O'Connell, A simple global model of plate dynamics and mantle convection, *J. Geophys. Res.*, *86*, 4843–4867, 1981.

Jackson, J. D., *Classical Electrodynamics*, John Wiley, New York, 1975.

Jarvis, G. T., and W. R. Peltier, Mantle convection as a boundary layer phenomenon, *Geophys. J. R. Astron. Soc.*, *68*, 389–427, 1982.

Jarvis, G. T., and W. R. Peltier, Lateral heterogeneity in the convecting mantle, *J. Geophys. Res.*, *91*, 435–451, 1986.

Lerch, F. S., S. M. Klosko, R. E. Laubscher, and C. A. Wagner, Gravity model improvement using GEOS 3 (GEM 9 and GEM 10), *J. Geophys. Res.*, *84*, 3897–3916, 1979.

Masters, G., T. H. Jordan, P. G. Silver, and F. Gilbert, Aspherical earth structure from fundamental spheroidal-mode data, *Nature*, *298*, 609–613, 1982.

Minster, J. B., and T. H. Jordan, Present-day plate motions, *J. Geophys. Res.*, *83*, 5331–5354, 1978.

Nakiboglu, S. M., Hydrostatic theory of the earth and its mechanical implications, *Phys. Earth Planet. Inter.*, *28*, 302–311, 1982.

O'Connell, R. J., Pleistocene glaciation and the viscosity of the lower mantle, *Geophys. J. R. Astron. Soc.*, *23*, 299–327, 1971.

Parsons, B., and S. Daly, The relationship between surface topography, gravity anomalies, and the temperature structure of convection, *J. Geophys. Res.*, *88*, 1129–1144, 1983.

Pekeris, C. L., Thermal convection in the interior of the earth, *Mon. Not. R. Astron. Soc., Geophys. Suppl.*, *3*, 343–367, 1935.

Peltier, W. R., Dynamics of the ice age earth, *Adv. Geophys.*, *24*, 1–146, 1982.

Peltier, W. R., Mantle convection and viscoelasticity, *Annu. Rev. Fluid Mech.*, *17*, 561–608, 1985*a*.

Peltier, W. R., New constraints on transient lower mantle rheology and internal mantle buoyancy from glacial rebound data, *Nature*, *318*, 611–614, 1985*b*.

Peltier, W. R., R. A. Drummond, and A. M. Tushingham, Post-glacial rebound and transient lower mantle rheology, *Geophys. J. R. Astron. Soc.*, *87*, 79–116, 1986.

Ranalli, G., and B. Fischer, Diffusion creep, dislocation creep, and mantle rheology, *Phys. Earth Planet. Inter.*, *34*, 77–84, 1984.

Ricard, Y., L. Fleitout, and C. Froidevaux, Geoid heights and lithospheric stresses for a dynamic earth, *Ann. Geophys.*, *2*, 267–286, 1984.

Richards, M. A., and B. H. Hager, Geoid anomalies in a dynamic earth, *J. Geophys. Res.*, *89*, 5987–6002, 1984*a*.

Richards, M. A., and B. H. Hager, Long-wavelength geoid anomalies and mantle-convection (abstract), *Eos Trans. AGU*, *65*, 184, 1984*b*.

Roberts, G. O., Fast viscous convection, *Geophys. Astrophys. Fluid Dyn.*, *8*, 197–233, 1977.

Runcorn, S. K., Satellite gravity measurements and a laminar viscous flos model of the earth's mantle, *J. Geophys. Res.*, *69*, 4389–4394, 1964.

Runcorn, S. K., Flow in the mantle inferred from the low degree harmonics of the geopotential, *Geophys. J. R. Astron. Soc.*, *14*, 375–384, 1967.

Sammis, C. G., J. C. Smith, G. Schubert, and D. A. Yuen, Viscosity-depth profile of the earth's mantle: Effects of polymorphic phase transitions, *J. Geophys. Res.*, *82*, 3747–3761, 1977.

Stacey, F. D., and D. E. Loper, The thermal boundary-layer interpretation of D'' and its role as a plume source, *Phys. Earth Planet. Inter.*, *33*, 45–55, 1983.

Turcotte, D. L., and E. R. Oxburgh, Finite amplitude convection cells and continental drift, *J. Fluid Mech.*, *28*, 29–42, 1967.

Woodhouse, J. H., and A. M. Dziewonski, Mapping the upper mantle: Three-dimensional model of earth structure by inversion of seismic waveforms, *J. Geophys. Res.*, *89*, 5953–5986, 1984.

A. M. Forte and W. R. Peltier, Department of Physics, University of Toronto, Toronto, Ontario, Canada M5S 1A7.

(Received June 3, 1986;
revised December 17, 1986;
accepted December 18, 1986.)